Analysis of Macroscopic Cloaking Devices

Tanaka, Tatsuo

(Degree)
博士（工学）

(Date of Degree)
2017-09-25

(Date of Publication)
2018-09-01

(Resource Type)
doctoral thesis

(Report Number)
甲第7009号

(URL)
https://hdl.handle.net/20.500.14094/D1007009

Doctoral Dissertation

Analysis of Macroscopic Cloaking Devices
（大規模クローキング素子の解析）

July 2017

Graduate School of System Informatics
Kobe University

Tatsuo Tanaka
（田中　健夫）

Abstract

Invisibility cloaking, which used to be a science fiction until the pioneering theoretical works based on transformation optics, has recently attracted considerable attention because it is expected to apply to industrial uses, such as transparent pillars of automobile bodies, the transparent hands of surgery support robots, and highly efficient solar cells. Cloaking devices have been designed by using transformation optics. In general, the constitutive parameters obtained from transformation optics become anisotropic and inhomogeneous. Therefore, the Hamiltonian-based ray tracing, which can deal with anisotropy and inhomogeneity in the constitutive parameters, is the only one method that can evaluate cloaking effects for large-scale objects.

However, the Hamiltonian-based ray tracing has been applied to only the regular shapes, such as spheres and cylinders. This thesis solves two technical issues for treatment of arbitrary shapes. The first issue is how to represent the surfaces of arbitrary shapes. The other issue is how to represent the constitutive parameters inside of cloaking devices with arbitrary shapes.

The first issue is the Hamiltonian-based ray tracing technique with surface-mesh representation, where the surfaces of cloaking devices are represented by triangular mesh structure. The results of the cloaking simulations with the surface-mesh representation are compared with those with rigorous function representation, where the surfaces of cloaking devices are represented by rigorous functions. The numerical results have shown a cloaking performance with the surface-mesh representation using fine mesh resolution is comparable to one with the rigorous function representation, suggesting the verification of the surface-mesh representation.

The second issue is the Hamiltonian-based ray tracing technique with full-mesh representation, where both the surface and the inner area of a cloaking device are represented by mesh structure and the constitutive parameters of the cloaking device are calculated by the finite element method using the mesh structure. The full-mesh representation has been verified by comparison between the results of the cloaking simulations with the full-mesh representation and those with the rigorous function representation. By using the Hamiltonian-based ray tracing with the full-mesh representation, cloaking characteristics of a double cylindrical cloaking device and a huge cloaking device with the completely arbitrary shape are evaluated. The numerical results have shown high performance, suggesting that the proposed Hamiltonian ray tracing can be applied to the evaluation of the performances of cloaking devices with arbitrary shapes.

Furthermore, by utilizing the proposed Hamiltonian-based ray tracing, the improvement in cloaking performance by the design of the distributions of the constitutive parameters is investigated. The cloaking performances of cylindrical cloaking with various distributions of the constitutive parameters are evaluated. The distributions are varied by employing the Navier's equation with various distributions of Young's moduli as the partial differential equation solved by the finite element method. The numerical results suggest that the proposed design method for the distributions of the constitutive parameters can improve cloaking performance in coarser mesh resolution. Therefore, this design method will contribute to the realization of large-scale cloaking devices because it can enhance the cloaking performances of cloaking devices fabricated by using technologies with coarse resolution.

Table of Contents

List of Figures

List of Tables

List of Symbols

Term	Unit	Description
$\mathbf{A}$	–	Jacobian transformation matrix
$\mathbf{A}'$	–	Jacobian transformation matrix of the inverse transformation
$\boldsymbol{B}$	T	Magnetic flux density of the original space
c	m/s	Speed of light in vacuum
C	–	Cross-correlation
d	m	Distance between the position and the center of the cylinder
$\boldsymbol{D}$	C/m^2	Electric flux density of the original space
$\boldsymbol{E}$	V/m	Electric field of the original space
$\boldsymbol{E}_0$	V/m	Amplitude of electric field
$\boldsymbol{E}'$	V/m	Electric field of the transformed space
$f(x,y)$	–	Gray levels of the reference image without any hidden object and any cloak device
$\langle f \rangle$	–	Spatial average values of $f(x,y)$
$g(x,y)$	–	Gray levels of the image with a hidden object and a cloak device
$\langle g \rangle$	–	Spatial average values of $g(x,y)$
$\mathbf{G}$	–	Deformation gradient tensor
$\mathbf{G}'$	–	Deformation gradient tensor for the inverse transformation
$h(\boldsymbol{r})$	–	Arbitrary function of $\boldsymbol{r}$
$\boldsymbol{H}$	A/m	Magnetic field of the original space
$\boldsymbol{H}_0$	V/m	Amplitude of magnetic field whose unit is same as $\boldsymbol{E}_0$
$\boldsymbol{H}'$	A/m	Magnetic field of the transformed space

$H(\boldsymbol{r},\boldsymbol{k})$	–	Hamiltonian of the cloaking medium
$H_0(\boldsymbol{r},\boldsymbol{k})$	–	Hamiltonian of the surrounding medium
i	–	$\sqrt{-1}$
$\mathbf{I}$	–	Identity matrix
$\boldsymbol{k}$	–	Normalized wave vector
k_0	rad/m	Magnitude of wave vector ω/c
$\boldsymbol{k}_1$	–	Wave vector of the incident ray from the air to the cloaking medium
$\boldsymbol{k}_2$	–	Wave vector of the refracted ray inside the cloaking medium
$\boldsymbol{k}'_1$	–	Wave vector of the incident ray from the cloaking medium to the air
$\boldsymbol{k}'_2$	–	Wave vector of the refracted ray outside the cloaking medium
$\mathbf{K}$	–	Operator defined as $K_{\alpha\gamma} \equiv \varepsilon_{\alpha\beta\gamma} k_\beta$
$\mathbf{n}$	–	Symmetric tensor
$\boldsymbol{n}$	–	Normal vector from the air to the cloaking medium
$\boldsymbol{n}'$	–	Normal vector pointing from the cloaking medium to the air
N_{ray}	–	Number of the total rays used for the evaluation of cloaking performance
$\boldsymbol{r}$	m	Spatial coordinates in the original space
r	m	Magnitude of r
$\boldsymbol{r}'$	m	Spatial coordinates in the transformed space
$\boldsymbol{r}_a$	m	Spatial coordinates of the point $\boldsymbol{a}$
$\boldsymbol{r}_b$	m	Spatial coordinates of the outer boundary in the original space, $\boldsymbol{b}$
$\boldsymbol{r}'_a$	m	Spatial coordinates of the inner boundary in the transformed space, $\boldsymbol{a}'$
$\boldsymbol{r}'_b$	m	Spatial coordinates of the outer boundary in the transformed space, $\boldsymbol{b}'$
R_a	m	Inner radius of the cylindrical shell or the spherical shell
R_b	m	Outer radius of the cylindrical shell or the spherical shell

t	s	Time
$\boldsymbol{U}$	m	Displacement field
$\boldsymbol{U}'$	m	Displacement field for the inverse transformation
$\mathbf{T}$	–	Matrix defined in Eq. (2-55)
Y	Pa	Young's modulus,
$\mathbf{Z}$	–	Matrix defined in Eq. (2-56)
$\boldsymbol{\varepsilon}$	F/m	Relative electrical permittivity tensor of the original space
$\boldsymbol{\varepsilon}'$	F/m	Relative electrical permittivity tensor of the transformed space
ε_0	F/m	Electrical permittivity of free space
ε_r	–	Principal permittivity whose principal axis is the radial axis
ε_ϕ	–	Principal permittivity whose principal axis is the azimuthal axis
ε_z	–	Principal permittivity whose principal axis is the Z axis
$\varepsilon_{\alpha\beta\gamma}$	–	Levi-Civita permutation tensor
η_0	Ω	Impedance of free space
κ	–	Poisson ratio
λ	m	Wavelength
$\boldsymbol{\mu}$	H/m	Relative magnetic permeability tensor of the original space
$\boldsymbol{\mu}'$	H/m	Relative magnetic permeability tensor of the transformed space
μ_0	H/m	Magnetic permeability of free space
θ_α	rad	Angle for the evaluation of cloaking performance
$\theta^{ref}{}_\alpha$	rad	Reference angle for the evaluation of cloaking performance
$\Delta\theta$	rad	Mean square root of the differences between θ_α and $\theta^{ref}{}_\alpha$
$\boldsymbol{\rho}$	m	Transverse coordinates
ρ	m	Magnitude of $\boldsymbol{\rho}$

$\sigma(f)$	–	Standard deviation of $f(x,y)$
$\sigma(g)$	–	Standard deviation of $g(x,y)$
τ	–	Parameter of a ray trajectory
$\boldsymbol{\tau}$	Pa	Stress tensor
ω	rad/s	Angular frequency
ψ	–	Derivative of $\boldsymbol{r}'$ with respect of $\boldsymbol{r}$
$\boldsymbol{\zeta}$	–	Strain tensor

CHAPTER 1

Introduction

1.1. Invisibility cloaking

Invisibility cloaking is a technology which makes an object transparent by making light guided around the hidden object as shown in Fig. 1-1. In order to realize invisibility cloaking, a special device is placed to cover the object to be hidden as shown in Fig. 1-2. Here, this device is called a cloaking device.

Although invisibility cloaking used to be a science fiction, such as Harry Potter, it has recently attracted considerable attention because of its possible realization thanks to theoretical works [1,2] and developments in metamaterial science [3-13]. So far various methods to realize invisibility cloaking have been proposed such as the transformation optics approach [1,2,14-18], the scattering cancelling approach [19-29], etc.

It is expected that invisibility cloaking opens many industrial applications. For example, a transparent pillar of an automobile body, as depicted in Fig. 1-3, is expected to reduce a dead zone of the view field of a driver leading to the decline of the number of car accidents [30-32]. In the medical field, if the hands of surgery support robots can be rendered as a transparent medium as shown in Figs. 1-4, the usability of these robots will be improved for their operators [33]. In addition, it has been reported that the efficiency of a solar cell can be enhanced by cloaking contact fingers which prevent light from

reaching the active area of the solar cell as shown Fig. 1-5. [34].

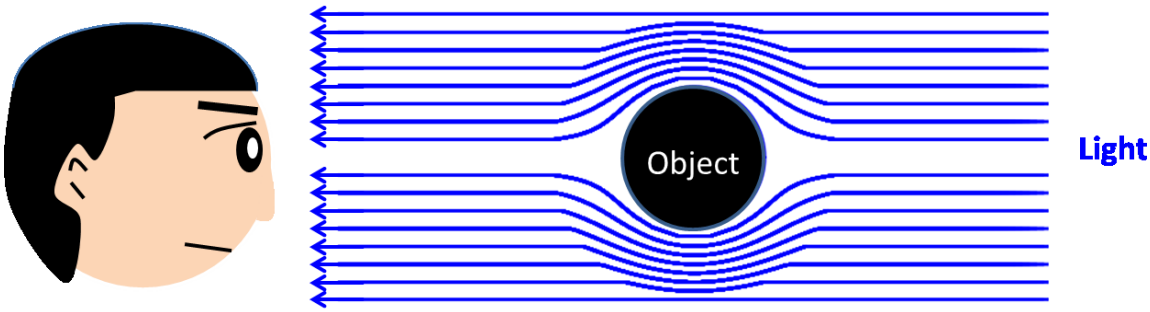

Fig. 1-1. The mechanism of invisibility cloaking.

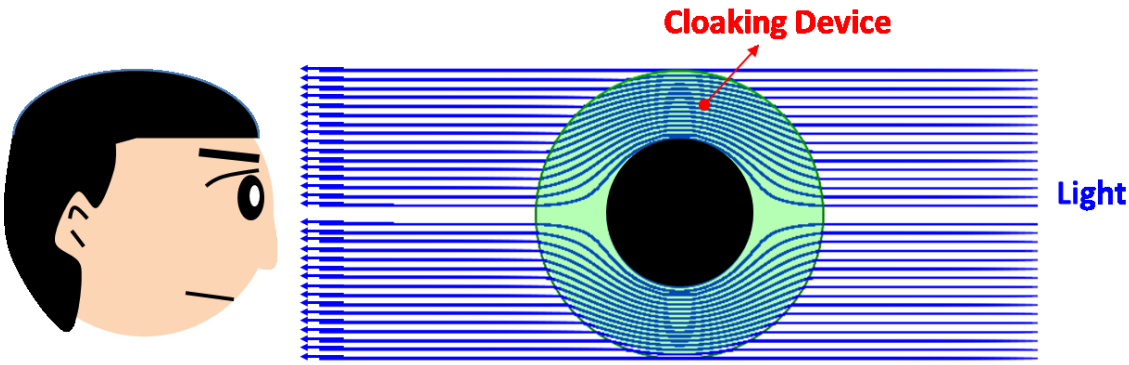

Fig. 1-2. A cloaking device.

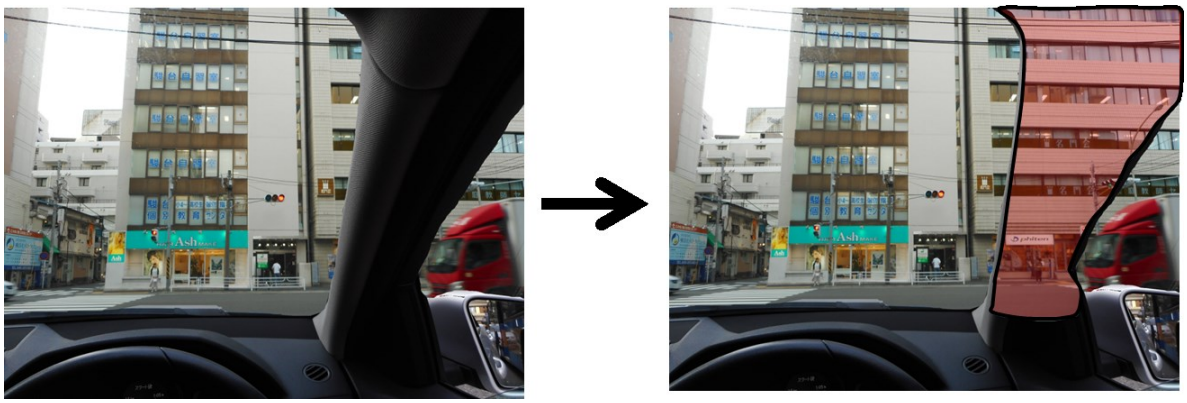

Fig. 1-3. A transparent pillar of an automobile body.

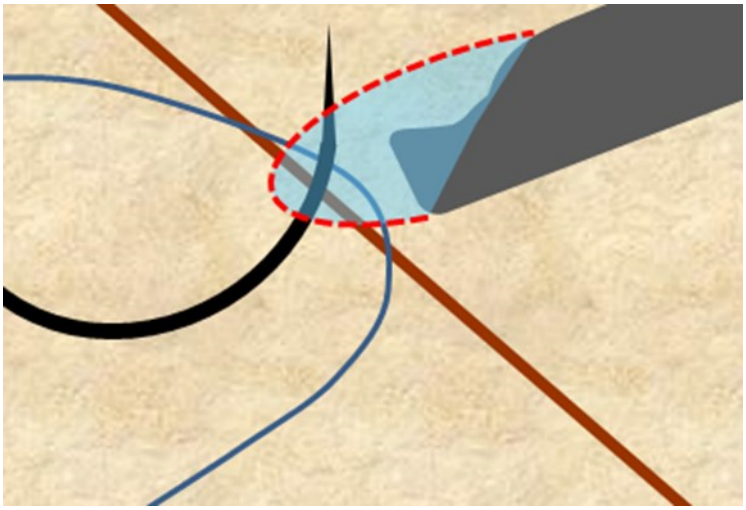

Fig. 1-4. A transparent hand of a surgery support robot.

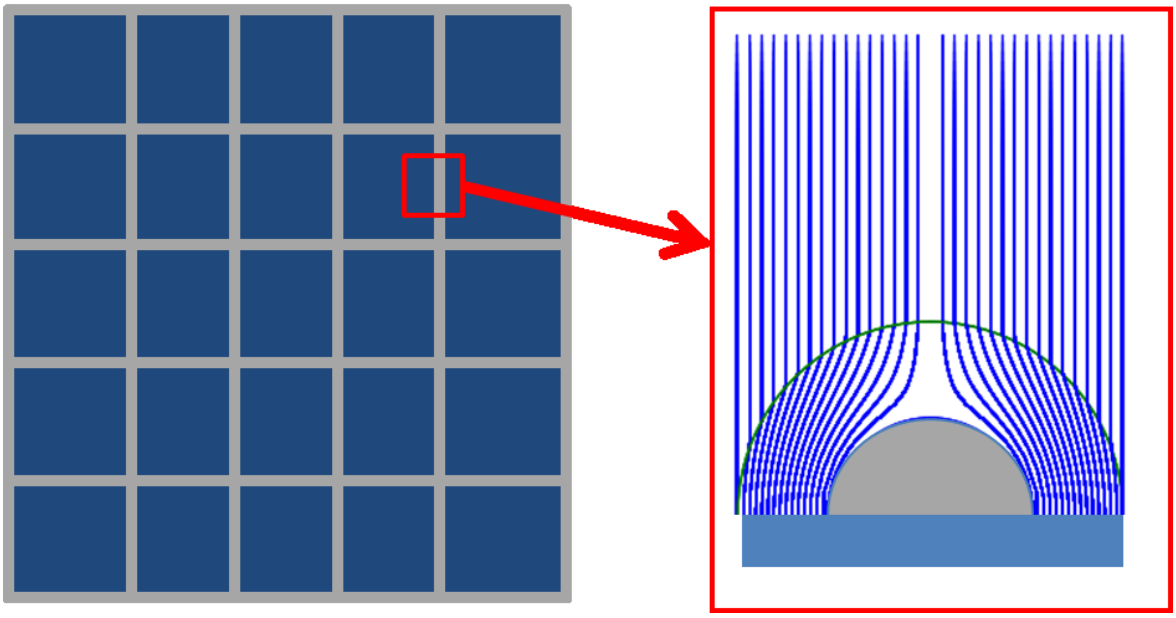

Fig. 1-5. The improvement of the efficiency of a solar cell by invisibility cloaking.

1.2. Transformation optics

Among the methods to realize invisibility cloaking, the transformation optics approach is expected to be applied to cloaking devices for large-scale objects such as pillars of automobile bodies and surgery support robots at optical frequencies because the other approaches are not well suited for large-scale objects.

Transformation optics is based on the fact that a coordinate transformation does not change the form of Maxwell's equation but changes the values of the electrical and magnetic field and the constitutive parameters. Let us consider the coordinate transformation as shown in Fig. 1-6. A ray of light can be bended at will by stretching and compressing the Cartesian space as shown in Fig. 1-6. Based on transformation optics, it is possible to re-interpret the light propagation in the transformed coordinate system as the propagation in the original coordinate system with specific distributions of the relative permittivity tensor, ε' and permeability tensor, μ'. The derivation of ε' and μ' will be described in SECTION 2.2.

Next, the coordinate transformation which makes a hole at the center, as shown in Fig. 1-7, is considered. By the coordinate transformation, a straight ray is transformed in to the curved ray which can avoid the hole. Assuming a cloaking device covers the light green area in Fig. 1-7, this ray path corresponds to that in the cloaking device. Therefore, invisibility cloaking can be realized by assigning ε' and μ' to the cloaking device. However, since some of the values of ε' and μ' obtained from transformation optics cannot be realized by any material in nature, metamaterial should be required for the realization of cloaking devices.

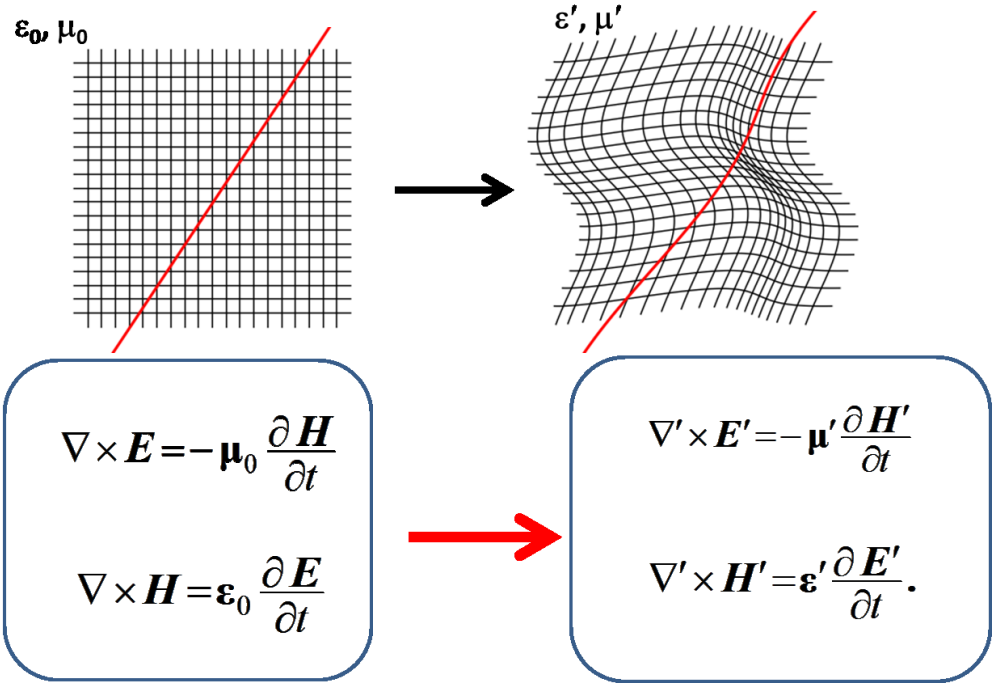

Fig. 1-6. A coordinate transformation for bending a ray of light.

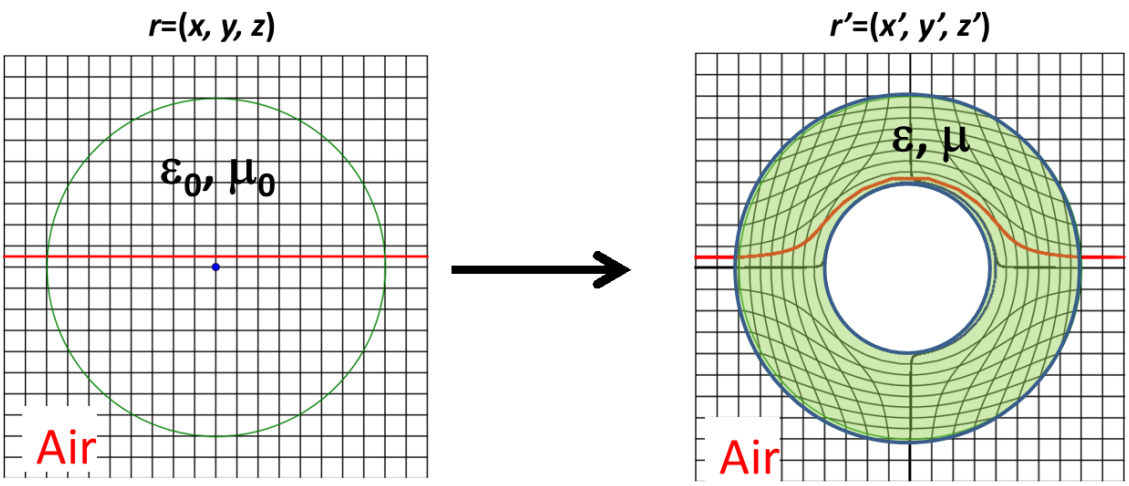

Fig. 1-7. A coordinate transformation which makes a hole at the center.

Invisibility cloaking based on transformation optics was proposed simultaneously and independently by Pendery [1] and by Leonhardt [2] in 2006. Since these propositions, research and development on invisibility cloaking have been progressed.

The first experimental verification of invisibility cloaking was shown for a microwave (8.5GHz) [14]. The cloaking device used in the experiment was fabricated by using a metamaterial which consists of split-ring resonators. Although invisibility cloaking at optical frequencies were also designed based on transformation optics [15], it has not been verified experimentally yet since nanotechnology still cannot support well to fabricate the sufficient metamaterial in visible wavelength range.

In addition to the design of invisible cloaking, transformation optics has been used for design of other optical devices. For example, based on force-loaded transformation optics, force-induced transformational devices, such as an optical escalator, have been proposed [35].

1.3. Design of cloaking device

A scheme of the design of a cloaking device is shown in Fig. 1-8. At the first step, the size and shape of the cloaking device is determined. At the second step, ideal and continuous distributions of ε and μ in the cloaking device are obtained based on transformation optics. The continuous distributions of ε and μ can give perfect cloaking. However, the continuous distributions of ε and μ cannot be realized by the current fabrication technology. Therefore, at the third step, the continuous distributions of ε and μ are discretized by mesh structure with certain resolution depending on the technology used for the fabrication of the cloaking device. Here, each element of the mesh structure is called a cell. At the fourth step, the geometry of a metamaterial with the values of ε

and μ at each cell is designed. Since the values of ε and μ of the metamaterial can be obtained by the retrieval method [36], the geometry of the metamaterial can be optimized so that the values of ε and μ calculated from the retrieval method get close to the values of ε and μ obtained at the third step. Finally, the metamaterial designed at each cell is located in the cloaking device, and then the design of the cloaking device is complete.

In the third step, the resolution of the discretization should be so fine that the cloaking device can show a sufficiently high performance for industrial uses. Hence, in order to determine the resolution of the discretization, the evaluation of the cloaking performance by optical simulation is required.

A classification table of optical simulation methods is shown in Table 1.1. As described in 1.2, ε and μ obtained by transformation optics become anisotropic and inhomogeous. Therefore, full-wave simulations, such as the Finite Difference Time Domain (FDTD) method, have been used for the evaluations because they can deal with anisotropy and inhomogeneity in ε and μ [37-43]. However, it is difficult to apply the full-wave simulations for large-scale objects such as pillars of automobile bodies and surgery support robots at optical frequencies because these simulations require large computational resources.

On the other hand, although the ray-tracing method [44] is a practical method for large-scale objects with anisotropy [45-47] or without anisotropy in their constitutive parameters, it cannot deal with inhomogeneity. In order to deal with inhomogeneity, the special ray tracing method called the Hamiltonian-based ray tracing is available [48-57]. Currently, the Hamiltonian-based ray tracing is the only one method that can evaluate the cloaking effects for large-scale objects.

Besides cloaking devices, an Eaton lens [58] and a graded negative-index metamaterial magnifier [59] have been investigated by the Hamiltonian-based ray tracing. Recently,

the Hamiltonian-based ray tracing has been extended to incorporate relativistic effects, such as relativistic Dopper effects and Fresnel-Fizeau drag [60, 61]. Furthermore, the method called "force tracing" to trace optical force has been proposed based on the Hamiltonian-based ray tracing [62].

However, the Hamiltonian-based ray tracing has been applied to only the regular shapes, such as spheres and cylinders. There are two technical issues to be solved for the treatment of arbitrary shapes. The first issue is how to represent the surfaces of arbitrary shapes. The other issue is how to represent the constitutive parameters inside cloaking devices with arbitrary shapes. On the other hand, in order to design and evaluate various practical cloaking devices for industrial uses, arbitrary shapes are needed to deal with by the Hamiltonian-based ray tracing.

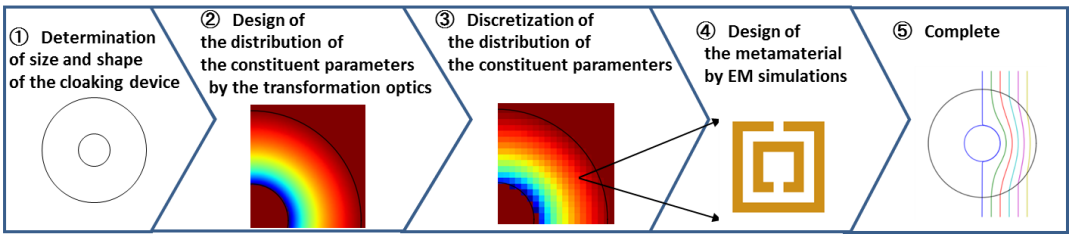

Fig. 1-8. A scheme of the design of a cloaking device.

Table 1.1: Classification table of the optical simulation methods.

Functionality	Full-wave [1-3]	Ray tracing	Hamiltonian-based ray tracing [4-14]	Hamiltonian-based ray tracing with mesh representation (Proposed Method)
Anisotropy	OK	OK	OK	OK
Inhomogeneity	OK	×	OK	OK
Macroscopic objects	×	OK	OK	OK
Arbitrary shapes	OK	OK	×	This Study

OK: possible, ×: difficult

1.4. Objective of thesis

The objective of this thesis is to establish a new Hamiltonian-based ray tracing method which can deal with arbitrary shapes and to apply this method to evaluation of cloaking devices. A strategy for the establishment of the new Hamiltonian-based ray tracing is shown in Fig. 1-9. In order to model the surfaces of arbitrary shapes, surface-mesh representation, where the surfaces are represented by mesh structure, is adapted. Furthermore, in order to represent the constitutive parameters inside cloaking devices with arbitrary shapes, full-mesh representation, where both the surface and the inner area of a cloaking device are represented by mesh structure and the constitutive parameters of the cloaking device are calculated by the finite element method using the mesh structure, is proposed. In addition, the improvement of cloaking performance by design of the distributions of the constitutive parameters in a cloaking device is investigated by using the Hamiltonian-based ray tracing with the full-mesh representation.

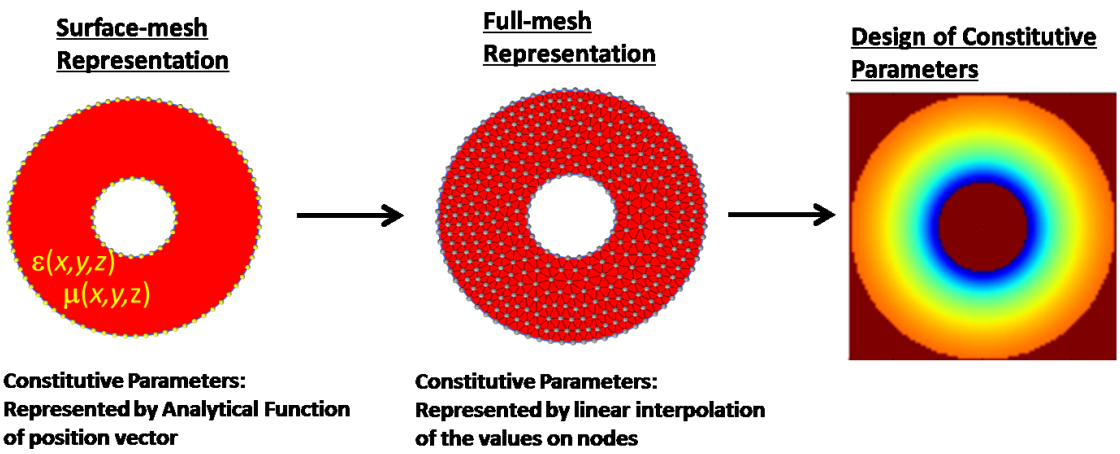

Fig. 1-9. A strategy for establishment of the new Hamiltonian-based ray tracing which can deal with arbitrary shapes.

1.5. Thesis organization

This dissertation is organized into six chapters as depicted in Fig. 1-10. Besides the current chapter which intends to give a brief introduction of invisibility cloaking, transformation optics, the design of cloaking devices and the motivations of this dissertation. Other five chapters are organized as following:

CHAPTER 2 describes calculation methods for evaluation of cloaking performance. The Hamiltonian-based ray tracing, the derivation of the formalism for the constitutive parameters based on transformation optics, and a numerical method for calculation of the constitutive parameters are presented.

In CHAPTER 3, the Hamiltonian-based ray-tracing technique with the surface-mesh representation is presented. In order to deal with cloaking devices with arbitrary shapes, the surfaces of the cloaking devices are represented by triangular mesh structure. Comparison between the results of cloaking simulations with the surface-mesh representation and those with rigorous function representation, where the surfaces of cloaking devices are represented by rigorous functions, is presented. The numerical results have shown that the cloaking performance with the surface-mesh representation using fine mesh resolution is comparable to one with the rigorous function representation. The results suggest the effectiveness of the surface-mesh representation.

In CHAPTER 4, the Hamiltonian-based ray tracing technique with the full-mesh representation, where both the surface and the inner area of a cloaking device are represented by mesh structure and the constitutive parameters of the cloaking device are calculated by the finite element method using the mesh structure, is proposed. The full-mesh representation has been verified by comparison between the results of cloaking simulations with the full-mesh representation and those with the rigorous

function representation. By using the Hamiltonian-based ray tracing with the full-mesh representation, cloaking characteristics of a double cylindrical cloaking device and a huge cloaking device with completely arbitrary shape are evaluated. The numerical results have shown high performance, suggesting that the Hamiltonian ray tracing can be applied to the evaluation of the performances of large cloaking devices with arbitrary shapes.

CHAPTER 5 describes the improvement of cloaking performance by the design of distributions of constitutive parameters. The cloaking performances of cylindrical cloaking with various distributions of the constitutive parameters are evaluated. The distributions are varied by employing the Navier's equation with various distributions of Young's moduli as the partial differential equation solved by the finite element method. The numerical results have suggested that the proposed design method for the distributions of the constitutive parameters can improve cloaking performance in coarser mesh resolution. Therefore, this design method will contribute to the realization of large-scale cloaking devices because it can enhance the cloaking performances of cloaking devices fabricated by using technologies even with coarse resolution.

CHAPTER 6 describes the conclusions of this thesis and the future work.

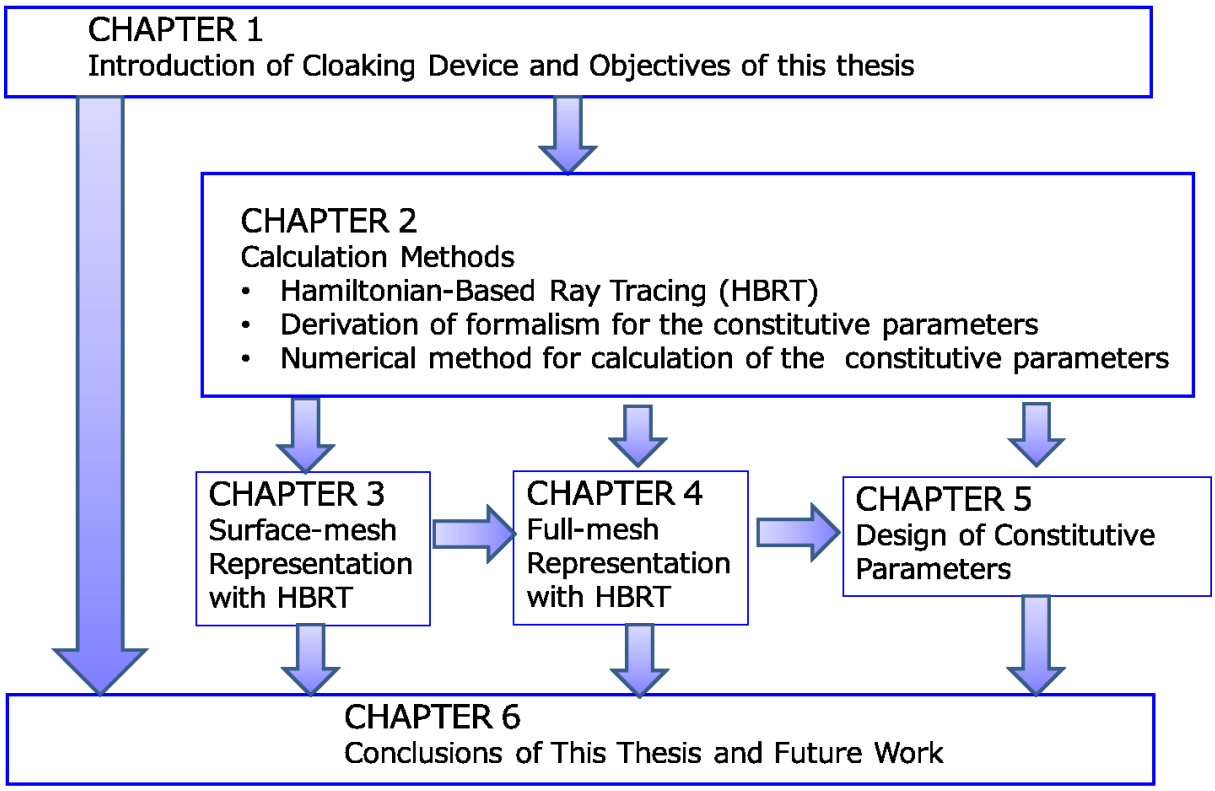

Fig. 1-10. Structure of thesis

References

1. J. B. Pendry, D. Schurig, and D. R. Smith, "Controlling electromagnetic fields," Science **312**, 1780–1782 (2006).
2. U. Leonhardt, "Optical conformal mapping," Science **312**, 1777–1780 (2006).
3. C. Caloz and T. Itoh, "Electromagnetic Metamaterials: Transmission Line Theory and Microwave Applications," John Wiley & Sons, 2005.
4. G. V. Eleftheriades and K. G. Balmain, "Negative-Refraction Metamaterials: Fundamental Principles and Applications," John Wiley & Sons, 2005.
5. N. Engheta and R. W. Ziolkowski, "Metamaterials: Physics and Engineering Explorations," John Wiley & Sons, 2006.
6. A. K. Sarychev and V. M. Shalaev, "Electrodynamics of Metamaterials," World Scientific, 2007.
7. W. Cai and V. M. Shalaev, "Optical Metamaterials: Fundamentals and Applications," Springer, 2009.
8. T. J. Cui, D. R. Smith, and R. Liu, "Metamaterials: Theory, Design, and Applications," Springer, 2009.
9. F. Capolino, "Theory and Phenomena of Metamaterials," CRC Press, 2009.
10. F. Capolino, "Applications of Metamaterials," CRC Press, 2009.
11. R. Marqués, F. Martín, and M. Sorolla, "Metamaterials with Negative Parameters: Theory, Design and Microwave Applications," John Wiley & Sons, 2011.
12. G. Shvets and I. Tsukerman, "Plasmonics and Plasmonic Metamaterials: Analysis and Applications," World Scientific, 2012.
13. R. V. Craster and S. Guenneau, "Acoustic Metamaterials: Negative Refraction, Imaging, Lensing and Cloaking," Springer, 2012.
14. D. Schurig, J. J. Mock, B. J. Justice, S. A. Cummer, J. B. Pendry, A. F. Starr, and D.

R. Smith, “Metamaterial electromagnetic cloak at microwave frequencies,” Science **314**, 977–980 (2006).

15. W. Cai, U. K. Chettiar, A. V. Kildishev, and V. M. Shalaev, “Optical cloaking with non-magnetic metamaterials,” Nat. Photonics **1**, 224–227 (2007).
16. D. Schurig, J. B. Pendry, and D. R. Smith, “Calculation of material properties and ray tracing in transformation media,” Opt. Express **14**, 9794–9804 (2006).
17. U. Leonhardt and T. Tyc, “Broadband Invisibility by Non-Euclidean Cloaking,” Science **323**, 110–112 (2009).
18. M. M. Crosskey, A. T. Nixon, L. M. Schick, and G. Kovačič, “Invisibility cloaking via non-smooth transformation optics and ray tracing,” Phys. Lett. A **375**, 1903-1911 (2011).
19. A. Alù and N. Engheta, “Achieving transparency with plasmonic and metamaterial coatings,” Phys. Rev. E **72**, 016623 (2005).
20. A. Alù and N. Engheta, “Plasmonic and metamaterial cloaking: physical mechanisms and potentials,” J. Opt. A: Pure Appl. Opt. **10**, 093002 (2008).
21. A. Alù and N. Engheta, “Plasmonic materials in transparency and cloaking problems: mechanism, robustness, and physical insights,” Opt. Express **15**, 3318–3332 (2007).
22. A. Alù and N. Engheta, “Cloaking and transparency for collections of particles with metamaterial and plasmonic covers,” Opt. Express **15**, 7578–7590 (2007).
23. A. Alù and N. Engheta, “Multifrequency Optical Invisibility Cloak with Layered Plasmonic Shells,” Phys. Rev. Lett.**100**, 113901 (2008).
24. A. Alù and N. Engheta, “Theory and potentials of multi-layered plasmonic covers for multi-frequency cloaking,” New J. Phys. **10**, 115036 (2008).
25. S. Tricarico, F. Bilotti, A. Alù, and L. Vegni, “Plasmonic cloaking for irregular

objects with anisotropic scattering properties," Phys. Rev. E **81**, 026602 (2010).

26. E. Kallos, C. Argyropoulos, Y. Hao, and A. Alù,"Comparison of frequency responses of cloaking devices under nonmonochromatic illumination," Phys. Rev. B **84**, 045102 (2011).
27. M. G. Silveirinha, A. Alù, and N. Engheta, "Infrared and optical invisibility cloak with plasmonic implants based on scattering cancellation," Phys. Rev. B **78**, 075107 (2008).
28. B. Edwards, A. Alù, M. G. Silveirinha, and N.Engheta, "Experimental Verification of Plasmonic Cloaking at Microwave Frequencies with Metamaterials," Phys. Rev. Lett. **103**, 153901 (2009).
29. D. Rainwater, A. Kerkhoff, K. Melin, J. C. Soric, G. Moreno, and A. Alù, "Experimental verification of three-dimensional plasmonic cloaking in freespace," New J. Phys. **14**, 013054 (2012).
30. R. Beach, "Killer pillars the blinding truth," http://www.safespeed.org.uk/bike005.pdf.
31. N. Joseph, "Jaguar and Rover develops 'transparent' A-pillar and ghost car," http://www.autoblog.com/2014/12/15/jaguar-land-rover-360-virtual-urban-windscreen-transparent-pillar-follow-me-ghost-carnavigation-systems-video-official/.
32. T. Yoshida, K. Jo, K. Minamizawa, H. Nii, N. Kawakami, and S. Tachi, Transparent Cockpit: Visual Assistance System for Vehicle Using Retro-Reflective Projection Technology (IEEE, 2008), pp. 185–188.
33. M. Inami, N. Kawakami, and S. Tachi, Optical Camouflage Using Retro-Reflective Projection Technology (IEEE, 2003), pp. 348–349.
34. M. F. Schumann, S. Wiesendanger, J. C. Goldschmidt, B. Bläsi, K. Bittkau, U. W. Paetzold and M. Wegener, "Cloaked contact grids on solar cells by coordinate

transformations: designs and prototypes," Optica, **2**, 850-853 (2015).

35. D. Gao, C. Qiu, L. Gao, T. Cui, and S. Zhang, "Macroscopic broadband optical escalator with force-loaded transformation optics," Opt. Express 21, 796–803 (2013).
36. D. R. Smith, S. Schultz, P. Markoš and C. M. Soukoulis, "Determination of effective permittivity and permeability of metamaterials from reflection and transmission coefficients," Phys. Rev. B, **65**, 195104 (2002).
37. S. A. Cummer, B.-I. Popa, D. Schurig, D. R. Smith, and J. Pendry, "Full-wave simulations of electromagnetic cloaking structures," Phys. Rev. E **74**, 036621 (2006).
38. F. Zolla, S. Guenneau, A. Nicolet, and J. B. Pendry,"Electromagnetic analysis of cylindrical invisibility cloaks and the mirage effect," Opt. Lett., **32**, 1069–1071 (2007).
39. L. M. Zhong, T. M. Niu, J. Bai, and T. J. Cui, "Design of transparent cloaks with arbitrarily inner and outer boundaries," J. Appl. Phys. **107**, 124908 (2010).
40. J. Hu, X. Zhou, and G. Hu, "Nonsingular two dimensional cloak of arbitrary shape," Appl. Phys. Lett. **95**, 011107 (2009).
41. X. Wang, S. Qu, S. Xia, B. Wang, Z. Xu, H. Ma, J. Wang, C. Gu, X. Wu, L. Lu, and H. Zhou, "Numberical Methods for Three-dimensional Electromagnetic Invisible Cloaks with Irregular Boundary Shapes," in Proceedings of Progress In Electromagnetics Research Symposium, pp. 1649-1652.
42. X. Wang , S. Qu, S. Xia, B. Wang , Z. Xu, H. Ma, J. Wang, C. Gu, X. Wu, L. Lu, and H. Zhou, "Numerical method of designing three-dimensional open cloaks with arbitrary boundary shapes," Photonics and Nanostructures - Fundamentals and Applications **8**, 205–208 (2010).

43. X. Wang, S. Qu, Z. Xu, H. Ma, J. Wang, C. Gu, and X. Wu, ”Three-dimensional invisible cloaks with arbitrary shapes based on partial differential equation,” Appl. Math. Comput. **216**, 426-430 (2010).
44. S. Andrew, Glassner, “An Introduction to Ray Tracing,” Morgan Kaufmann, 1989.
45. O. N. Stavroudis, “Ray-tracing formulas for uniaxial crystals,” J. Opt. Soc. Am. **52**, 187–191 (1962).
46. L. Quan-Ting, “Simple ray tracing formulas for uniaxial optical crystals,” Appl. Opt. **29**, 1008–1010 (1990).
47. S. C. McClain, L. W. Hillman, and R. A. Chipman, “Polarization ray tracing in anisotropic optically active media. I. Algorithms,” J. Opt. Soc. Am. A **10**, 2371–2382 (1993).
48. J. A. Arnaud, “Beam and Fiber Optics,” Academic, New York, 1976.
49. Y. Kravtsov and Y. I. Orlov, “Geometrical optics of inhomogeneous media,” Springer-Verlag, Berlin, 1990.
50. J.C. Halimeh, and M. Wegener, “Photorealistic rendering of unidirectional free-space invisibility cloaks”, Opt. Express **21**, 9457–9472 (2013).
51. J. C. Halimeh and M. Wegener, “Time-of-flight imaging of invisibility cloaks,” Opt. Express **20**, 63–74 (2012).
52. J. C. Halimeh, R. Schmied, and M. Wegener, “Newtonian photorealistic ray tracing of grating cloaks and correlation-function-based cloaking-quality assessment,” Opt. Express **19**, 6078–6092 (2011).
53. J. C. Halimeh, and M. Wegener, “Photorealistic ray tracing of free-space invisibility cloaks made of uniaxial dielectrics,” Opt. Express **20**, 28330–28340 (2012).
54. A. J. Danner, “Visualizing invisibility: Metamaterials-based optical devices in natural environments,” Opt. Express **18**, 3332–3337 (2010).

55. G. Dolling, M. Wegener, S. Linden, and C. Hormann, “Photorealistic images of objects in effective negative-index materials,” Opt. Express **14**, 1842–1849 (2006).
56. 56. Y. Jiao, S. Fan, and D. A. B. Miller, “Designing for beam propagation in periodic and nonperiodic photonic nanostructures: Extended Hamiltonian method,” Phys. Rev. E **70**, 036612 (2004).
57. 57. A. Alireza, and A. J. Danner, “Generalization of ray tracing in a linear inhomogeneous anisotropic medium: a coordinate-free approach,” J. Opt. Soc. Am. A **27**, 2558–2562 (2010).
58. A. Akbarzadeh and A. J. Danner, “Generalization of ray tracing in a linear inhomogeneous anisotropic medium: a coordinate-free approach,” J. Opt. Soc. Am. A **27**, 2558-2562 (2010).
59. C. Qiu, A. Akbarzadeh, T. Han, and A. J. Danner, “Photorealistic rendering of a graded negative-index metamaterial magnifier,” New J. Phys. **14**, 033024 (2012).
60. J. C. Halimeh, R. T. Thompson, and M. Wegener, “Invisibility cloaks in relativistic motion.” Phys. Rev. A **93**, 013850 (2016).
61. J. C. Halimeh, and R. T. Thompson, “Fresnel-Fizeau drag: Invisibility conditions for all inertial observers,” arXiv:1601.04218.
62. A. Akbarzadeh, J. A. Crosse, M. Danesh, C. Qiu, A. J. Danner, and C. M. Soukoulis, “Interplay of Optical Force and Ray-Optic Behavior between Luneburg Lenses,” ACS Photonics **2**, 1384−1390 (2015).

CHAPTER 2

Calculation Methods

2.1. Hamiltonian-based ray tracing

In order to design a cloaking device for a large-scale object, such as pillars of automobile bodies and surgery support robots, for which full-wave simulations cannot be applied due to too many computational resources required, the Hamiltonian-based ray tracing [1-17] has been employed in this thesis. This ray tracing is based on Hamiltonian equations can deal with the media with inhomogeneity and anisotropy in their electric permittivity and magnetic permeability, which cannot be dealt with by the general ray tracing. The Hamiltonian-based ray tracing described in Ref. [1] is explained briefly.

In order to derive its governing equations, let us consider Maxwell's equations in a medium with no sources or currents as follows,

$$\nabla \times \boldsymbol{E} = -\frac{\partial \boldsymbol{B}}{\partial t}, \qquad \nabla \times \boldsymbol{H} = \frac{\partial \boldsymbol{D}}{\partial t}, \tag{2-1}$$

where $\boldsymbol{E}$ represents the electric field, $\boldsymbol{B}$ the magnetic flux density, $\boldsymbol{H}$ the magnetic field, $\boldsymbol{D}$ the electric flux density. With the wavelength (λ) to be very short compared with the scales of the changes of the components of the electric permittivity $\varepsilon_{\alpha\beta}$ and magnetic permeability $\mu_{\alpha\beta}$ in the cloaking medium, the following relation is obtained:

$$\lambda \cdot \frac{\partial \ln \varepsilon_{\alpha\beta}}{\partial x} << 1 . \tag{2-2}$$

With this relation, plane wave solutions can be assumed for Eq. (2-1), which are appropriate for the geometric limit,

$$\boldsymbol{E} = \boldsymbol{E}_0 \, e^{i(k_0 \boldsymbol{k}\cdot\boldsymbol{r} - \omega t)}, \;\; \boldsymbol{H} = \frac{1}{\eta_0} \boldsymbol{H}_0 \, e^{i(k_0 \boldsymbol{k}\cdot\boldsymbol{r} - \omega t)}, \tag{2-3}$$

where $\eta_0 = \sqrt{\mu_0/\varepsilon_0}$ is the impedance of free space, giving $\boldsymbol{E_0}$ and $\boldsymbol{H_0}$ the same units, and $\boldsymbol{k_0} = \omega/c$ making $\boldsymbol{k}$ dimensionless. The constitutive relations for a linear medium are given by the equations with dimensionless tensors $\boldsymbol{\varepsilon}$ and $\boldsymbol{\mu}$,

$$\boldsymbol{D} = \varepsilon_0 \boldsymbol{\varepsilon} \boldsymbol{E}, \qquad \boldsymbol{B} = \mu_0 \boldsymbol{\mu} \boldsymbol{H}. \tag{2-4}$$

Plugging Eq. (2-3) and Eq. (2-4) into the curl equations described in Eq. (2-1), the following equations are obtain,

$$\boldsymbol{k} \times \boldsymbol{E_0} - \boldsymbol{\mu} \boldsymbol{H_0} = 0, \qquad \boldsymbol{k} \times \boldsymbol{H_0} + \boldsymbol{\varepsilon} \boldsymbol{E_0} = 0. \tag{2-5}$$

By eliminating the magnetic field, the following equation is obtained,

$$\boldsymbol{k} \times \left(\boldsymbol{\mu}^{-1} \left(\boldsymbol{k} \times \boldsymbol{E_0} \right) \right) + \boldsymbol{\varepsilon} \boldsymbol{E_0} = 0. \tag{2-6}$$

Equation (2-6) can be expressed as a single operator on $\boldsymbol{E_0}$,

$$\left(\mathbf{K} \boldsymbol{\mu}^{-1} \mathbf{K} + \boldsymbol{\varepsilon} \right) \boldsymbol{E_0} = 0, \tag{2-7}$$

where the operator K is defined as

$$K_{\alpha\gamma} \equiv \varepsilon_{\alpha\beta\gamma} k_\beta, \tag{2-8}$$

where ε_{ijk} is the Levi-Civita permutation tensor defined as

$$\varepsilon_{\alpha\beta\gamma} \equiv \begin{cases} 1 & ((\alpha,\beta,\gamma) = (1,2,3),(2,3,1),(3,1,2)) \\ -1 & ((\alpha,\beta,\gamma) = (1,3,2),(3,2,1),(2,1,3)). \\ 0 & (\text{otherwise}) \end{cases} \tag{2-9}$$

Since Eq. (2-7) must be singular for non-zero field solutions, the dispersion relation can be derived from the condition that this operator must have zero determinate,

$$\det\left(\mathbf{K}\boldsymbol{\mu}^{-1}\mathbf{K} + \boldsymbol{\varepsilon}\right) = 0. \tag{2-10}$$

Now $\boldsymbol{\varepsilon}$ and $\boldsymbol{\mu}$ are the same symmetric tensor, which is called as $\mathbf{n}$, since material properties are derived from transforming free space. In this case, an alternate expression of the dispersion relation can be obtained,

$$\det\left(\mathbf{K}\boldsymbol{\mu}^{-1}\mathbf{K} + \boldsymbol{\varepsilon}\right) = \frac{1}{\det(\mathbf{n})}\left(\boldsymbol{k}\,\mathbf{n}\,\boldsymbol{k} - \det(\mathbf{n})\right)^2 = 0. \tag{2-11}$$

Although the latter expression clearly has fourth order in k, it has only two unique solutions. This suggests that media with $\boldsymbol{\varepsilon} = \boldsymbol{\mu}$ are singly refracting.

Equation (2-11) finally gives the Hamilton-Jacobi equation,

$$\boldsymbol{k}\,\mathbf{n}\,\boldsymbol{k} - \det(\mathbf{n}) = 0. \tag{2-12}$$

Note that this equation can be multiplied by an arbitrary scalar function, $h(\boldsymbol{r})$, of the position vector $\boldsymbol{r}$.

Equation (2-12) can be solved using characteristics of light rays [16, 17]. Let us

parametrize the characteristics by the parameter τ. Then the following equation is obtained,

$$\frac{dk_\alpha}{d\tau} = \sum_{\beta=1}^{3} \frac{\partial k_\alpha}{\partial r_\beta} \frac{dr_\beta}{d\tau}. \tag{2-13}$$

Let us rewrite Eq. (2-12) as

$$H(\boldsymbol{r},\boldsymbol{k}) = h(\boldsymbol{r})(\boldsymbol{k}\,\mathbf{n}\,\boldsymbol{k} - \det(\mathbf{n})) = 0, \tag{2-14}$$

where $h(\boldsymbol{r})$ is an arbitrary function of $\boldsymbol{r}$. Equation (2-14) is the definition of the Hamiltonian. By differentiating the equation $H(\boldsymbol{r}, \boldsymbol{k}) = 0$ with respect to r_α, the following equation can be obtained,

$$\sum_{\beta=1}^{3} \frac{\partial H}{\partial k_\beta} \frac{\partial k_\beta}{\partial r_\alpha} + \frac{\partial H}{\partial r_\alpha} = 0. \tag{2-15}$$

If the following equation is chosen,

$$\frac{dr_\alpha}{d\tau} = \frac{\partial H}{\partial k_\alpha}, \tag{2-16}$$

Eq. (2-13) and Eq. (2-15) reveal

$$\frac{dk_\alpha}{d\tau} = -\frac{\partial H}{\partial r_\alpha}, \tag{2-17}$$

as well as

$$\frac{dH}{d\tau} = 0. \tag{2-18}$$

In other words, the ray trajectories corresponding to Eq. (2-12) can be described by the Hamiltonian system,

$$\frac{\partial \boldsymbol{r}}{\partial \tau} = \frac{\partial H}{\partial \boldsymbol{k}}, \tag{2-19a}$$

$$\frac{\partial \boldsymbol{k}}{\partial \tau} = -\frac{\partial H}{\partial \boldsymbol{r}}, \tag{2-19b}$$

with H($\boldsymbol{r}$, $\boldsymbol{k}$) = 0. Therefore, the ray trajectories can be obtained by solving the pair of coupled, first order ordinary differential ray equations.

Although the ray trajectories throughout the cloaking device can be obtained by solving Eqs. (2-19a) and (2-19b), special care is needed at the interface between the cloaking medium and the surrounding medium because the direction of an incident ray changes discontinuously, i.e., the refraction of ray occurs. The direction of the refracted ray can be determined by solving the following equations resulting from the boundary conditions at the interface,

$$(\boldsymbol{k}_1 - \boldsymbol{k}_2) \times \boldsymbol{n} = 0, \tag{2-20}$$

$$H(\boldsymbol{k}_2) = 0, \tag{2-21}$$

where $\boldsymbol{k_1}$ is the wave vector of the incident ray, $\boldsymbol{k_2}$ is the wave vector of the refracted ray inside the cloaking medium, $\boldsymbol{n}$ is the normal vector pointing into the cloaking medium as shown in Fig.2-1 (a) and H is the Hamiltonian of the cloaking medium.

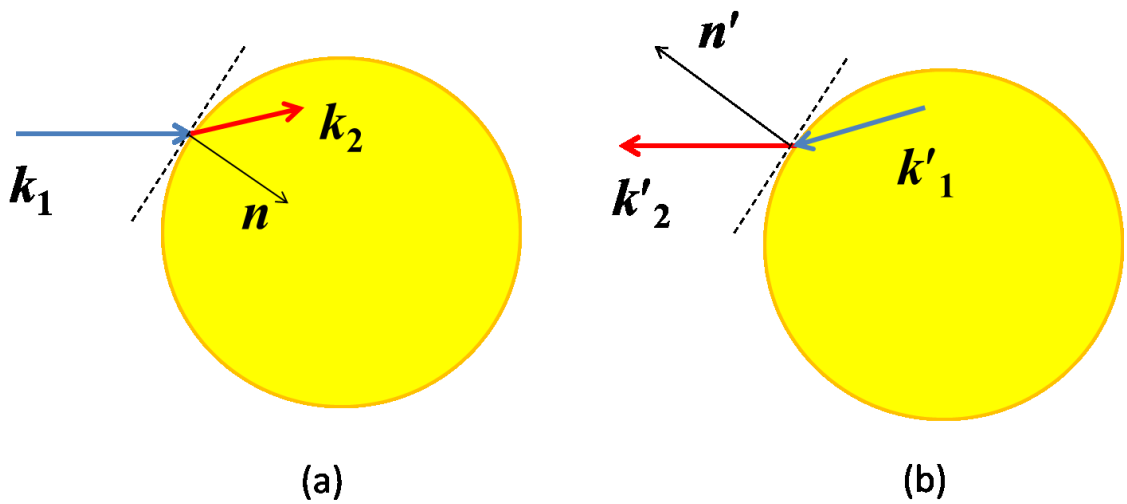

Fig. 2-1. (a) Refraction at the surface of the cloaking device from the air into medium, and $\boldsymbol{n}$ is the normal vector from the air into the cloaking medium. In the cloaking medium , $\boldsymbol{k}_1$ is the wave vector of the incident ray, $\boldsymbol{k}_2$ is the wave vector of the refracted ray inside the cloaking medium, and $\boldsymbol{n}'$ is the normal vector from the cloaking medium into the air. (b) Refraction at the surface of the cloaking device from the cloaking medium into the air: $\boldsymbol{k}'_1$ is the wave vector of of the incident ray, and $\boldsymbol{k}'_2$ is the wave vector of the refracted ray outside the cloaking medium.

Equation (2-21) has two solutions where the light carries energy into the cloaking medium and the light carries energy out from the cloaking medium. Hence the desired solution corresponds to the former. On the other hand, the direction of the energy flow is determined by the path of the ray, i.e., Eq. (2-19a). Therefore, the desired solution can be chosen by the following condition:

$$\frac{\partial H}{\partial \boldsymbol{k}} \cdot \boldsymbol{n} > 0, \tag{2-22}$$

where $\boldsymbol{n}$ is the normal vector from the surrounding medium into the cloaking medium.

In the case of refraction out of the cloaking medium as shown in Fig. 2-1(b), the direction of the refracted ray can be determined by solving the following equations

instead of Eqs. (2-20), (2-21) and (2-22),

$$(\boldsymbol{k}_1' - \boldsymbol{k}_2') \times \boldsymbol{n}' = 0, \tag{2-23}$$

$$H_0(\boldsymbol{k}_2') = 0, \tag{2-24}$$

$$\frac{\partial H_0}{\partial \boldsymbol{k}} \cdot \boldsymbol{n}' > 0, \tag{2-25}$$

where $\boldsymbol{k}'_1$ is the wave vector of the incident ray, $\boldsymbol{k}'_2$ is the wave vector of the refracted ray outside the cloaking medium, $\boldsymbol{n}'$ is the normal vector from the medium into the surrounding medium (air) and H_0 is the Hamiltonian of the surrounding medium,

$$H_0 = \boldsymbol{k}^{\mathrm{T}} \cdot \boldsymbol{k} - 1. \tag{2-26}$$

2.2. Derivation of the formalism of the constitutive parameters based on transformation optics

In order to derive the formalism of the constitutive parameters based on transformation optics, the invariance of Maxwell's equations under a spatial coordinate transformation is exploited following Refs. [18-21]. Let us consider Maxwell's equations in a medium with no sources or currents in the Cartesian coordinate $\boldsymbol{r}$,

$$\nabla \times \boldsymbol{E} = -\frac{\partial \boldsymbol{B}}{\partial t}, \tag{2-27}$$

$$\nabla \times \boldsymbol{H} = \frac{\partial \boldsymbol{D}}{\partial t}, \tag{2-28}$$

$$\nabla \cdot \boldsymbol{D} = 0, \tag{2-29}$$

$$\nabla \cdot \boldsymbol{B} = 0, \tag{2-30}$$

where $\boldsymbol{E}$ represents the electric field, $\boldsymbol{B}$ the magnetic induction, $\boldsymbol{H}$ the magnetic field, $\boldsymbol{D}$ the electric displacement field. The constitutive relations for a linear medium are given by the following equations with dimensionless tensors $\boldsymbol{\varepsilon}$ and $\boldsymbol{\mu}$,

$$\boldsymbol{D} = \varepsilon_0 \boldsymbol{\varepsilon} \boldsymbol{E}, \tag{2-31}$$

$$\boldsymbol{B} = \mu_0 \boldsymbol{\mu} \boldsymbol{H}. \tag{2-32}$$

In index notation, the Einstein convention is employed whereby repeated indices are summed over. Eq. (2-27) is now expressed as

$$\partial_\alpha E_\beta \varepsilon_{\alpha\beta\gamma} = -\mu_{\gamma\chi} \frac{\partial H_\chi}{\partial t}. \tag{2-33}$$

where $\varepsilon_{\alpha\beta\gamma}$ is the Levi-Civita permutation tensor and $\partial = \partial/\partial r_\alpha$.

Now suppose that the coordinate is changed from $\boldsymbol{r} = (x, y, z)$ to $\boldsymbol{r'} = (x', y', z')$. Let $\mathbf{A}$ denote the Jacobian transformation matrix,

$$\mathbf{A} = \begin{pmatrix} \partial x'/\partial x & \partial x'/\partial y & \partial x'/\partial z \\ \partial y'/\partial x & \partial y'/\partial y & \partial y'/\partial z \\ \partial z'/\partial x & \partial z'/\partial y & \partial z'/\partial z \end{pmatrix}, \tag{2-34}$$

or

$$A_{\alpha\beta} = \frac{\partial r'_\alpha}{\partial r_\beta}. \tag{2-35}$$

Under the coordinate change, the following equations are obtained,

$$\partial_\alpha = A_{\beta\alpha}\partial'_\beta, \tag{2-36}$$

$$E_\alpha = A_{\beta\alpha}E'_\beta, \tag{2-37}$$

$$H_\alpha = A_{\beta\alpha}H'_\beta. \tag{2-38}$$

Hence, Eq. (2-27) can be expressed as follows,

$$A_{o\alpha}\partial'_o A_{p\beta}E'_q\varepsilon_{\alpha\beta\gamma} = -\mu_{\gamma\chi}A_{s\chi}\frac{\partial H'_s}{\partial t}. \tag{2-39}$$

Here, the $A_{o\alpha}\partial'_\alpha = \partial_\alpha$ derivative falls on both the $A_{p\beta}$ and E'_p terms, but the former can be eliminated due to the $\varepsilon_{\alpha\beta\gamma}$: $\partial_\alpha A_{p\beta}\varepsilon_{\alpha\beta\gamma} = 0$ because of $\partial_\alpha A_{p\beta} = \partial_\beta A_{p\alpha}$. Then, multiplying both sides by the Jacobian $A_{q\gamma}$, the following equation can be obtain

$$A_{q\gamma}A_{o\alpha}A_{p\beta}\partial'_o E'_p\varepsilon_{\alpha\beta\gamma} = -A_{q\gamma}\mu_{\gamma\chi}A_{s\chi}\frac{\partial H'_s}{\partial t}. \tag{2-40}$$

Noting that $A_{o\alpha}A_{p\beta}A_{q\gamma}\varepsilon_{\alpha\beta\gamma} = \varepsilon_{opq}\det\mathbf{A}$ by definition of the determinant, the following equation is finally derived,

$$\partial'_o E'_p\varepsilon_{opq} = -\frac{1}{\det\mathbf{A}}A_{q\gamma}\mu_{\gamma\chi}A_{s\chi}\frac{\partial H'_s}{\partial t}, \tag{2-41}$$

or, in vector notation,

$$\nabla' \times \boldsymbol{E}' = -\frac{\mathbf{A}\boldsymbol{\mu}\mathbf{A}^{\mathrm{T}}}{\det\mathbf{A}}\frac{\partial \boldsymbol{H}'}{\partial t}. \tag{2-42}$$

By the same argument, the following equation can be obtained,

$$\nabla' \times \boldsymbol{H}' = \frac{\mathbf{A}\boldsymbol{\varepsilon}\mathbf{A}^{\mathrm{T}}}{\det\mathbf{A}}\frac{\partial \boldsymbol{E}'}{\partial t}. \tag{2-43}$$

Equation (2-28) becomes

$$\begin{aligned}
\partial_\alpha \varepsilon_{\alpha\beta} E_\beta &= A_{o\alpha}\partial'_o \varepsilon_{\alpha\beta} A_{p\beta} E'_p = A_{o\alpha}\partial'_o (\det\mathbf{A}) A^{-1}_{\alpha q}\frac{A_{q\alpha}\varepsilon_{\alpha\beta}A_{p\beta}}{\det\mathbf{A}}E'_p \\
&= (\det\mathbf{A}) A_{o\alpha}A^{-1}_{\alpha q}\partial'_o \frac{A_{q\alpha}\varepsilon_{\alpha\beta}A_{p\beta}}{\det\mathbf{A}}E'_p + A_{o\alpha}\partial'_o\left[A^{-1}_{\alpha q}(\det\mathbf{A})\right]\frac{A_{q\alpha}\varepsilon_{\alpha\beta}A_{p\beta}}{\det\mathbf{A}}E'_p \\
&= (\det\mathbf{A})\delta_{oq}\partial'_o \frac{A_{q\alpha}\varepsilon_{\alpha\beta}A_{p\beta}}{\det\mathbf{A}}E'_p + A_{o\alpha}\partial'_o\left[A^{-1}_{\alpha q}(\det\mathbf{A})\right]\frac{A_{q\alpha}\varepsilon_{\alpha\beta}A_{p\beta}}{\det\mathbf{A}}E'_p \\
&= (\det\mathbf{A})\partial'_o \frac{A_{o\alpha}\varepsilon_{\alpha\beta}A_{p\beta}}{\det\mathbf{A}}E'_p + \partial_\alpha\left[A^{-1}_{\alpha q}(\det\mathbf{A})\right]\frac{A_{q\alpha}\varepsilon_{\alpha\beta}A_{p\beta}}{\det\mathbf{A}}E'_p \\
&= (\det\mathbf{A})\partial'_o \frac{A_{o\alpha}\varepsilon_{\alpha\beta}A_{p\beta}}{\det\mathbf{A}}E'_p = 0.
\end{aligned} \tag{2-44}$$

Here, from the cofactor formula for the matrix inverse, and $\partial_\alpha A_{p\beta}\varepsilon_{\alpha\beta\gamma} = 0$,

$$\partial_\alpha\left[A^{-1}_{\alpha q}(\det\mathbf{A})\right] = \partial_\alpha\left[\bar{A}_{\alpha q}\right] = \partial_\alpha\left[\frac{1}{2}\varepsilon_{qop}\varepsilon_{\alpha uv}A_{ou}A_{pv}\right] = 0, \tag{2-45}$$

where $\bar{A}_{\alpha q}$ is the cofactor of $\mathbf{A}$ at the αth row and the qth column. Therefore, the following equation can be obtained,

$$\partial'_o \frac{A_{o\alpha}\varepsilon_{\alpha\beta}A_{p\beta}}{\det\mathbf{A}}E'_p = 0. \tag{2-46}$$

or, in vector notation,

$$\nabla \cdot \frac{\mathbf{A}\,\boldsymbol{\varepsilon}\,\mathbf{A}^{\mathbf{T}}}{\det\mathbf{A}} \boldsymbol{E}' = 0. \tag{2-47}$$

Similarly, Equation (2-30) becomes

$$\nabla \cdot \frac{\mathbf{A}\,\boldsymbol{\mu}\,\mathbf{A}^{\mathbf{T}}}{\det\mathbf{A}} \boldsymbol{H}' = 0. \tag{2-48}$$

From Eqs. (2-42), (2-43), (2-47), and (2-48), it can be shown that Maxwell's equations take on the same form in the transformed coordinate system if the following transformations are made,

$$\boldsymbol{\varepsilon}' = \frac{\mathbf{A}\,\boldsymbol{\varepsilon}\,\mathbf{A}^{\mathbf{T}}}{\det\mathbf{A}}, \tag{2-49}$$

$$\boldsymbol{\mu}' = \frac{\mathbf{A}\,\boldsymbol{\mu}\,\mathbf{A}^{\mathbf{T}}}{\det\mathbf{A}}, \tag{2-50}$$

Using the above transformation rules, the curved rays in the transformed space can be reinterpreted as the physical rays propagating through the medium with the transformed relative electric permeability and magnetic permittivity tensors ε' and μ', given by Eqs. (2-49) and (2-50).

2.3. Numerical method for calculation of the constitutive parameters

A space transformation from the original space, $\boldsymbol{r}=(x,y,z)$, to the transformed space, $\boldsymbol{r}'=(x', y', z')$, as shown in Fig. 2-2, is considered. The relative permittivity tensor and the permeability tensor in the transformed space, $\boldsymbol{\varepsilon}'$ and $\boldsymbol{\mu}'$, are obtained from transformation optics as

$$\boldsymbol{\varepsilon}' = \frac{\mathbf{A} \cdot \boldsymbol{\varepsilon} \cdot \mathbf{A}^{\mathrm{T}}}{\det(\mathbf{A})}, \tag{2-51}$$

$$\boldsymbol{\mu}' = \frac{\mathbf{A} \cdot \boldsymbol{\mu} \cdot \mathbf{A}^{\mathrm{T}}}{\det(\mathbf{A})}, \tag{2-52}$$

where $\boldsymbol{\varepsilon}$ and $\boldsymbol{\mu}$ are the relative permittivity tensor and the permeability tensor in the original space. $\mathbf{A}$ is the Jacobian transformation matrix defined as

$$\mathbf{A} = \begin{pmatrix} \partial x'/\partial x & \partial x'/\partial y & \partial x'/\partial z \\ \partial y'/\partial x & \partial y'/\partial y & \partial y'/\partial z \\ \partial z'/\partial x & \partial z'/\partial y & \partial z'/\partial z \end{pmatrix}, \tag{2-53}$$

Therefore, $\boldsymbol{\varepsilon}'$ and $\boldsymbol{\mu}'$ can be calculated if the components of $\mathbf{A}$ are obtained.

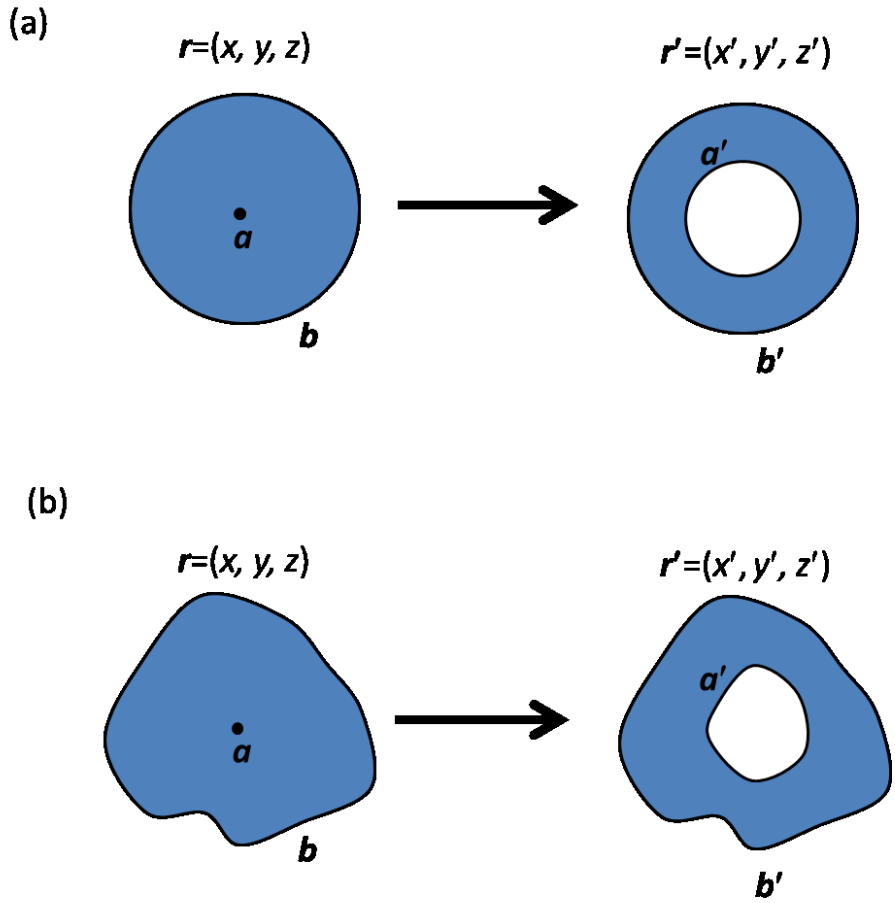

Fig. 2-2. The space transformation from the original space, $\boldsymbol{r}=(x,y,z)$, to the transformed space, $\boldsymbol{r}'=(x', y', z')$ for cylindrical cloaking (a) and for arbitrary shaped cloaking (b).

Subsequently, the calculation of the components of **A** is considered. If the transformed coordinate, $\boldsymbol{r}'=(x', y', z')$, can be expressed by analytical functions of the components of $\boldsymbol{r}$, that is, x', y' *or* z', the components of **A** can also be described analytically, resulting in analytical solutions for $\boldsymbol{\varepsilon}'$ and $\boldsymbol{\mu}'$.

For instance, $\boldsymbol{\varepsilon}'$ and $\boldsymbol{\mu}'$ for a cylinder cloaking device with its rotational symmetry axis aligned along the z-axis as shown in Fig. 2-2 (a) [1] is given by,

$$\boldsymbol{\varepsilon}'=\boldsymbol{\mu}'=\mathbf{n}'=\frac{\rho}{\rho-R_a}\mathbf{T}-\frac{2R_a\rho-R_a^{\,2}}{\rho^3(\rho-R_a)}\boldsymbol{\rho}\otimes\boldsymbol{\rho}+\left(\frac{R_b}{R_b-R_a}\right)^2\frac{\rho-R_a}{\rho}\mathbf{Z}, \tag{2-54}$$

where $\boldsymbol{\rho}=(x', y', 0)$ is the transverse coordinate with its coordinate origin to be the rotational symmetry axis of the cylindrical cloaking device, ρ is the magnitude of $\boldsymbol{\rho}$, R_a and R_b are the inner radius and the outer radius of the cylindrical shell, respectively, **T** and **Z** are the following matrixes,

$$\mathbf{T}=\begin{pmatrix}1 & 0 & 0\\ 0 & 1 & 0\\ 0 & 0 & 0\end{pmatrix}, \tag{2-55}$$

$$\mathbf{Z}=\begin{pmatrix}0 & 0 & 0\\ 0 & 0 & 0\\ 0 & 0 & 1\end{pmatrix}, \tag{2-56}$$

On the other hand, in the case of cloaking devices with arbitrary shapes as shown in Fig. 2-2 (b), it is difficult to express $\boldsymbol{r}'$ as analytical functions of the components of $\boldsymbol{r}$. Hence, expressing $\boldsymbol{\varepsilon}'$ and $\boldsymbol{\mu}'$ as analytical functions is also difficult. In order to solve the issue, a numerical technique for calculation of $\boldsymbol{\varepsilon}'$ and $\boldsymbol{\mu}'$ has been proposed in Ref. [21]. The technique described in Ref. [21] is explained briefly as follows.

A scheme of the numerical method is shown in Fig. 2-3. The space transformation depicted in Fig. 2-2 can be supposed to be a forced deformation problem in the continuum mechanics. Hence, the transformed coordinates are expressed as follows,

$$\begin{pmatrix}x'\\ y'\\ z'\end{pmatrix}=\begin{pmatrix}x\\ y\\ z\end{pmatrix}+\begin{pmatrix}U_x\\ U_y\\ U_z\end{pmatrix}, \tag{2-57}$$

where U_α ($\alpha=x,y,z$) are called the displacement field in the continuum mechanics. Therefore, the components of **A** can be expressed as

$$
\begin{aligned}
\mathbf{A} &= \begin{pmatrix} 1+\partial U_x/\partial x & \partial U_x/\partial y & \partial U_x/\partial z \\ \partial U_y/\partial x & 1+\partial U_y/\partial y & \partial U_y/\partial z \\ \partial U_z/\partial x & \partial U_z/\partial y & 1+\partial U_z/\partial z \end{pmatrix} \\
&= \begin{pmatrix} 1 & 0 & 0 \\ 0 & 1 & 0 \\ 0 & 0 & 1 \end{pmatrix} + \begin{pmatrix} \partial U_x/\partial x & \partial U_x/\partial y & \partial U_x/\partial z \\ \partial U_y/\partial x & \partial U_y/\partial y & \partial U_y/\partial z \\ \partial U_z/\partial x & \partial U_z/\partial y & \partial U_z/\partial z \end{pmatrix} \\
&= \mathbf{I} + \mathbf{G},
\end{aligned}
\tag{2-58}
$$

where the tensor **G** is called the deformation gradient tensor in the continuum mechanics and **I** is the identity matrix.

Let us consider the boundary conditions for the forced deformation problem shown in Fig. 2-2. The outer boundary of the transformed region, $\boldsymbol{b'}$, is the same as that of the original region, $\boldsymbol{b}$. On the other hand, the inner boundary of the transformed region, $\boldsymbol{a'}$, is extended from the point of the original region, $\boldsymbol{a}$. Consequently, the boundary conditions for the forced deformation problem are given by

$$
\begin{pmatrix} U_x(\boldsymbol{r_b}) \\ U_y(\boldsymbol{r_b}) \\ U_z(\boldsymbol{r_b}) \end{pmatrix} = \begin{pmatrix} 0 \\ 0 \\ 0 \end{pmatrix},
\tag{2-59}
$$

$$
\begin{pmatrix} U_x(\boldsymbol{r_a}) \\ U_y(\boldsymbol{r_a}) \\ U_z(\boldsymbol{r_a}) \end{pmatrix} = \boldsymbol{r'_a} - \boldsymbol{r_a} = \begin{pmatrix} x'_a - x_a \\ x'_a - x_a \\ x'_a - x_a \end{pmatrix} = \begin{pmatrix} x'_a \\ x'_a \\ x'_a \end{pmatrix},
\tag{2-60}
$$

where $\boldsymbol{r_a} = (x_a, y_a, z_a) = (0, 0, 0)$ and $\boldsymbol{r_b} = (x_b, y_b, z_b)$ are position vectors at the point, $\boldsymbol{a}$ and the outer boundary of the original region, $\boldsymbol{b}$, and $\boldsymbol{r'_a} = (x'_a, y'_a, z'_a)$ is the position vector at the inner boundary of the transformed region, $\boldsymbol{a'}$.

U_α and **G** can be obtained by solving the Laplace's equation as

$$\left(\frac{\partial^2}{\partial x^2}+\frac{\partial^2}{\partial y^2}+\frac{\partial^2}{\partial z^2}\right)U_\alpha = 0,\ (\alpha = x, y, z), \tag{2-61}$$

with the Dirichlet boundary conditions shown in Eqs. (2-58) and (2-59).

Nevertheless, the solution of the Laplace's equation, Eq. (2-61), becomes singular at the point, ***a.*** In order to prevent the singular solution, the inverse transformation, $\boldsymbol{r'} \rightarrow \boldsymbol{r}$, is considered. In the inverse transformation, the original coordinates are described as

$$\begin{pmatrix} x \\ y \\ z \end{pmatrix} = \begin{pmatrix} x' \\ y' \\ z' \end{pmatrix} + \begin{pmatrix} U'_x \\ U'_y \\ U'_z \end{pmatrix}, \tag{2-62}$$

where U'_α (α=x,y,z) are the displacement fields. Then, the inverse form of the Laplace's equation is obtained as,

$$\left(\frac{\partial^2}{\partial x'^2}+\frac{\partial^2}{\partial y'^2}+\frac{\partial^2}{\partial z'^2}\right)U'_\alpha = 0,\ (\alpha = x, y, z), \tag{2-63}$$

The Dirichlet boundary conditions correspondingly become

$$\begin{pmatrix} U'_x(\boldsymbol{r'_b}) \\ U'_y(\boldsymbol{r'_b}) \\ U'_z(\boldsymbol{r'_b}) \end{pmatrix} = \begin{pmatrix} 0 \\ 0 \\ 0 \end{pmatrix}, \tag{2-64}$$

$$\begin{pmatrix} U'_x(\boldsymbol{r'_a}) \\ U'_y(\boldsymbol{r'_a}) \\ U'_z(\boldsymbol{r'_a}) \end{pmatrix} = \boldsymbol{r_a} - \boldsymbol{r'_a} = \begin{pmatrix} x_a - x'_a \\ y_a - y'_a \\ z_a - z'_a \end{pmatrix} = \begin{pmatrix} -x'_a \\ -y'_a \\ -z'_a \end{pmatrix}, \tag{2-65}$$

where $\boldsymbol{r'_b}$ = (x'_b, y'_b, z'_b) is the position vector at the outer boundary of the transformed region, $\boldsymbol{b'}$.

By solving Eqs. (2-62), (2-63), and (2-64), the deformation gradient tensor **G'** can be obtained as follows,

$$\mathbf{G}' = \begin{pmatrix} \partial U'_x/\partial x' & \partial U'_x/\partial y' & \partial U'_x/\partial z' \\ \partial U'_y/\partial x' & \partial U'_y/\partial y' & \partial U'_y/\partial z' \\ \partial U'_z/\partial x' & \partial U'_z/\partial y' & \partial U'_z/\partial z' \end{pmatrix}, \tag{2-66}$$

From the components of $\mathbf{G}'$, the components of Jacobian transformation matrix of the inverse transformation can be calculated as follows,

$$\begin{aligned} \mathbf{A}' &= \begin{pmatrix} \partial x/\partial x' & \partial x/\partial y' & \partial x/\partial z' \\ \partial y/\partial x' & \partial y/\partial y' & \partial y/\partial z' \\ \partial z/\partial x' & \partial z/\partial y' & \partial z/\partial z' \end{pmatrix} \\ &= \begin{pmatrix} 1+\partial U'_x/\partial x' & \partial U'_x/\partial y' & \partial U'_x/\partial z' \\ \partial U'_y/\partial x' & 1+\partial U'_y/\partial y' & \partial U'_y/\partial z' \\ \partial U'_z/\partial x' & \partial U'_z/\partial y' & 1+\partial U'_z/\partial z' \end{pmatrix} \\ &= \mathbf{I} + \mathbf{G}', \end{aligned} \tag{2-67}$$

By the inversion of $\mathbf{A}'$, the components of **A** can be calculated. Finally, by applying A into Eqs. (2-50) and (2-51), respectively, $\boldsymbol{\varepsilon}'$ and $\boldsymbol{\mu}'$ can be obtained.

The solution of Laplace's equation is attained by means of the Finite Element Method (FEM). As a program for the FEM, Elmer from CSC, which is an open source program, is employed [22].

Since space transformations, as shown in Fig. 2-2, can be specified for cloaking devices with arbitrary shapes, $\boldsymbol{\varepsilon}'$ and $\boldsymbol{\mu}'$ of each of cloaking devices can be obtained through transformation optics [23]. The space transformations can be expressed numerically as described in Eq. (2-57). Consequently, the FEM-based numerical technique for the calculation of $\boldsymbol{\varepsilon}'$ and $\boldsymbol{\mu}'$ described above can be utilized for cloaking

devices with arbitrary shapes including irregular shapes [24-27]. It is noted that the sufficient accuracy of the solution of the FEM is required when the FEM-based numerical technique is used. The accuracy of the solution affects the performances of cloaking devices through the accuracy of ε′ and μ′.

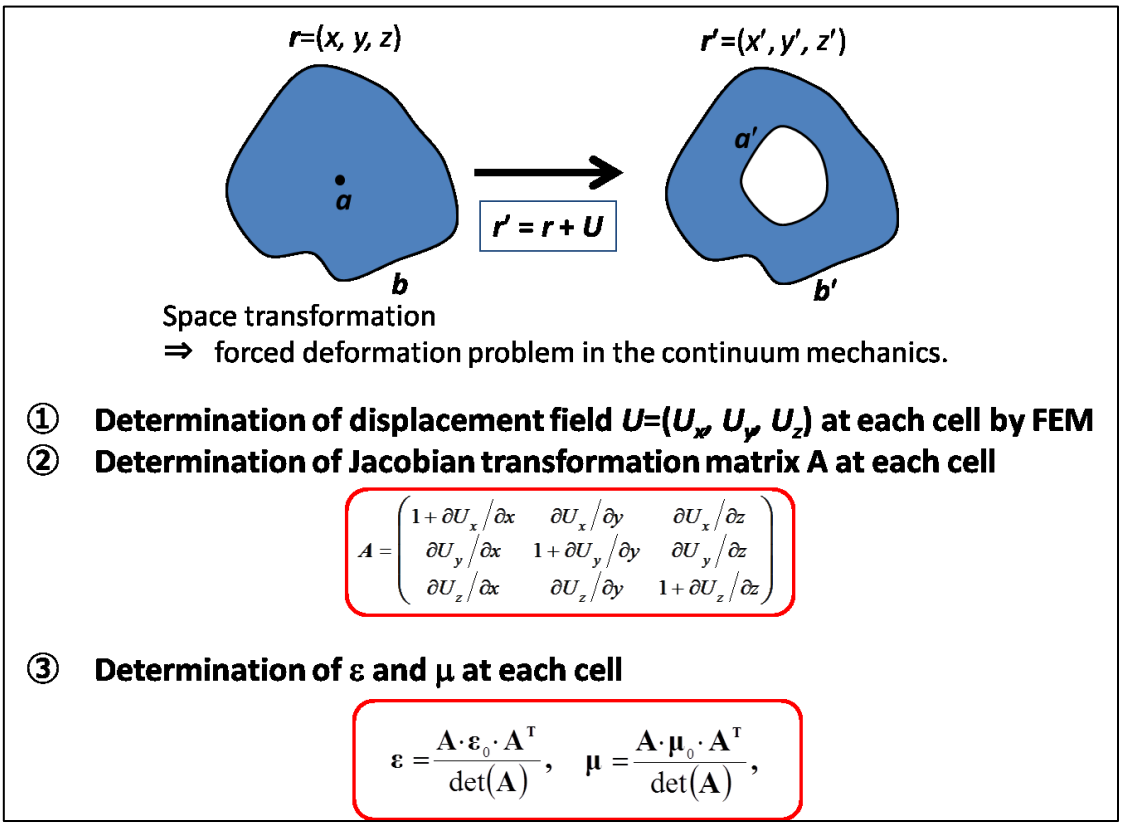

Fig. 2-3. A scheme of the numerical method for calculation of the relative permittivity tensor and permeability tensor.

References

1. D. Schurig, J. B. Pendry, and D. R. Smith, "Calculation of material properties and ray tracing in transformation media," Opt. Express **14**, 9794–9804 (2006).
2. M. M. Crosskey, A. T. Nixon, L. M. Schick, and G. Kovačič, "Invisibility cloaking via non-smooth transformation optics and ray tracing," Phys. Lett. A **375**, 1903-1911 (2011).
3. J. C. Halimeh, R. Schmied, and M. Wegener, "Newtonian photorealistic ray tracing of grating cloaks and correlation-function-based cloaking-quality assessment", Opt. Express **19**, 6078–6092 (2011).
4. J. C. Halimeh and M. Wegener, "Time-of-flight imaging of invisibility cloaks," Opt. Express **20**, 63–74 (2012).
5. J. C. Halimeh, and M. Wegener, "Photorealistic ray tracing of free-space invisibility cloaks made of uniaxial dielectrics," Opt. Express **20**, 28330–28340 (2012).
6. J.C. Halimeh, and M. Wegener, "Photorealistic rendering of unidirectional free-space invisibility cloaks", Opt. Express **21**, 9457–9472 (2013).
7. J. C. Halimeh, R. T. Thompson, and M. Wegener, "Invisibility cloaks in relativistic motion." Phys. Rev. A **93**, 013850 (2016).
8. J. C. Halimeh, and R. T. Thompson, "Fresnel-Fizeau drag: Invisibility conditions for all inertial observers," arXiv:1601.04218.
9. A. J. Danner, "Visualizing invisibility: Metamaterials-based optical devices in natural environments," Opt. Express **18**, 3332–3337 (2010).
10. A. Alireza, and A. J. Danner, "Generalization of ray tracing in a linear inhomogeneous anisotropic medium: a coordinate-free approach," J. Opt. Soc. Am. A **27**, 2558–2562 (2010).
11. C. Qiu, A. Akbarzadeh, T. Han and A. J Danner, "Photorealistic rendering of a

graded negative-index metamaterial magnifier,", New J. Phys., **14**, 033024 (2012) .

12. Y. Jiao, S. Fan, and D. A. B. Miller, "Designing for beam propagation in periodic and nonperiodic photonic nanostructures: Extended Hamiltonian method," Phys. Rev. E **70**, 036612 (2004).
13. X. Sun, Z. Yang, X. Liu, C. Li, Y. Dong, L. Xie, and J. E. Sipe, "Hamiltonian optics formalism for microring resonator structures with varying ring resonances," Opt. Express, **19**, 7176-7189 (2011).
14. M. Sluijter, D. K. G. de Boer, and J. J. M. Braat, "General polarized ray-tracing method for inhomogeneous uniaxially anisotropic media," J. Opt. Soc. Am. A, **25**, 1260–1273 (2008).
15. K. Niu, C. Song, and M.-L- Ge, "The geodesic form of light-ray trace in the inhomogeneous media," Opt. Express, **17**, 11753-11767 (2009).
16. J. A. Arnaud, Beam and Fiber Optics (Academic, New York, 1976).
17. Y. Kravtsov and Y. I. Orlov, Geometrical optics of inhomogeneous media (Springer-Verlag, Berlin, 1990).
18. A. J. Ward and J. B. Pendry, "Refraction and geometry in maxwell's equations," J. Mod. Opt. **43**, 773-793 (1996).
19. D. M. Shyroki. Exact equivalent straight waveguide model for bent and twisted waveguides. IEEE Trans. Microwave Theory Tech., **56**, 414-419 (2008).
20. C. Kottke, A. Farjadpour, and S. G. Johnson, "Perturbation theory for anisotropic dielectric interfaces, and application to sub-pixel smoothing of discretized numerical methods," Phys. Rev. E, **77**, 036611 (2008).
21. J. Hu, X. Zhou and G. Hu, "Design method for electromagnetic cloak with arbitrary shapes based on Laplace's equation," Opt. Express **17**, 1308-1320 (2009).
22. https://www.csc.fi/web/elmer.

23. W. Yan, M. Yan, Z. Ruan, and M. Qiu, “Coordinate transformations make perfect invisibility cloaks with arbitrary shape,” New J. Phys. **10**, 043040 (2008).
24. X. Wang, S. Qu, S. Xia, B. Wang, Z. Xu, H. Ma, J. Wang, C. Gu, X. Wu, L. Lu, and H. Zhou, “Numerical methods for three-dimensional electromagnetic invisible cloaks with irregular boundary shapes,” in Proceedings of Progress In Electromagnetics Research Symposium, Xi’an, China (2010), pp. 1649–1652.
25. X. Wang, S. Qu, Z. Xu, H. Ma, J. Wang, C. Gu, and X. Wu, “Three-dimensional invisible cloaks with arbitrary shapes based on partial differential equation,” Appl. Math. Comput. **216**, 426–430 (2010).
26. W. X. Jiang, J. Y. Chin, Z. Li, Q. Cheng, R. Liu, and T. J. Cui, “Analytical design of conformally invisible cloaks for arbitrarily shaped objects,” Phys. Rev. E **77**, 066607 (2008).
27. H. Ma, S. Qu, Z. Xu, and J. Wang, “Numerical method for designing approximate cloaks with arbitrary shapes,” Phys. Rev. E **78**, 036608 (2008).

CHAPTER 3

Surface-mesh Representation with Hamiltonian-based Ray Tracing Method

3.1. Introduction

A new Hamiltonian-based ray tracing method is proposed. In the proposed method, the surfaces of three-dimensional arbitrary shapes are modeled by triangular mesh representation in order to verify the cloaking effects for large-scale objects. Table 3-1 shows the classification of optical simulation methods. Full wave simulation is an ideal and can deal with arbitrary shapes [1-3], but it is impossible to calculate large-scale objects for the industrial applications. Although the ray tracing method is a practical method for large-scale objects with anisotropy or without anisotropy in their constitutive parameters, it cannot deal with inhomogeneity. Thus, Hamiltonian-based ray tracing is the only one method which can evaluate the cloaking effects for large-scale objects.

The remaining problem is how to implement arbitrary shapes of the large-scale cloaking devices. Hamiltonian-based ray tracing has two technical issues for the treatment of arbitrary shapes. The first issue is how to represent the surfaces of arbitrary shapes. The other issue is how to obtain ε and μ for arbitrary shapes.

The proposed Hamiltonian-based ray tracing with triangular mesh representation can deal with the first issue. This is the first time of the optical simulation for evaluation of

the cloaking effects of large-scale objects.

Table 3-1: Classification table of the optical simulation methods.

Functionality	Full-wave [1-3]	Ray Tracing	Hamiltonian-based ray tracing [4-14]	Hamiltonian-based ray tracing with mesh representation (Proposed Method)
Anisotropy	OK	OK	OK	OK
Inhomogeneity	OK	×	OK	OK
Macroscopic objects	×	OK	OK	OK
Arbitrary shapes	OK	OK	×	OK

OK: possible, ×: difficult

3.2. Calculation method

Cloaking performances are evaluated by using Hamiltonian-based ray tracing [4-14] as described in 2.1. In order to design a cloaking device with an arbitrary shape, the surface of the cloaking device is represented by the triangular meshes as shown in Fig. 3-1(a). This representation of a surface is called surface-mesh representation in this thesis. These meshes are prepared by using the commercial mesh generation software, HyperMesh from Altair Engineering Inc. On the other hand, if a cloaking device has a simple shape, such as sphere or cylinder, the surface of the cloaking device can be represented by a rigorous function as shown in Fig. 3-1(b). This representation of a surface is called rigorous function representation in this thesis.

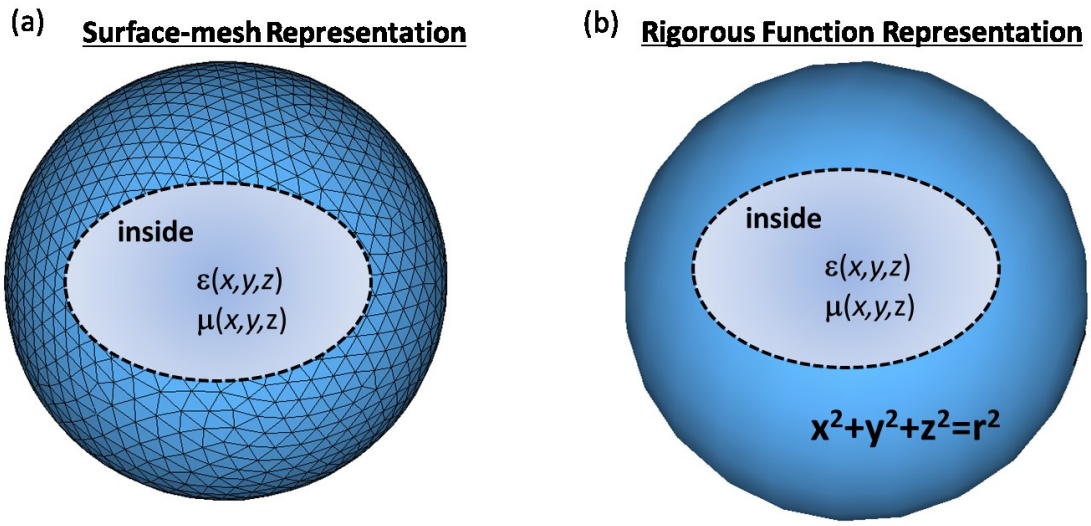

Fig. 3-1. (a) Surface-mesh represention for the surface of the cloaking device; (b) rigorous function representation for the surface of the cloaking deivice.

The relative permittivity tensor $\boldsymbol{\varepsilon}$ and permeability tensor $\boldsymbol{\mu}$ inside the cloaking device are input as functions of the position vector $\boldsymbol{r}=(x, y, z)$, where the coordinate origin is set to the center of the cloaking device. For example, in the case of sphere cloaking [4], $\boldsymbol{\varepsilon}$ and $\boldsymbol{\mu}$ can be expressed as

$$\boldsymbol{\varepsilon}=\boldsymbol{\mu}=\mathbf{n}=\frac{R_b}{R_b-R_a}\left(\mathbf{I}-\frac{2R_a r-R_a^{\,2}}{r^4}\boldsymbol{r}\otimes\boldsymbol{r}\right), \tag{3-1}$$

where R_a and R_b are the inner radius and the outer radius of the spherical shell, respectively, r is the magnitude of $\boldsymbol{r}$, $\mathbf{I}$ is the identity matrix and $\boldsymbol{r}\otimes\boldsymbol{r}$ is the outer product of the position vector r with itself.

In the case of cylinder cloaking with the rotational symmetry axis aligned along the z-axis [4], the following $\boldsymbol{\varepsilon}$ and $\boldsymbol{\mu}$ can be chosen,

$$\boldsymbol{\varepsilon}=\boldsymbol{\mu}=\mathbf{n}=\frac{\rho}{\rho-R_a}\mathbf{T}-\frac{2R_a\rho-R_a^{\,2}}{\rho^3(\rho-R_a)}\boldsymbol{\rho}\otimes\boldsymbol{\rho}+\left(\frac{R_b}{R_b-R_a}\right)^2\frac{\rho-R_a}{\rho}\mathbf{Z}, \tag{3-2}$$

where $\boldsymbol{\rho}=(x,y,0)$, ρ is the magnitude of ρ, R_a and R_b are the inner radius and the outer radius of the cylindrical shell, respectively, **T** and **Z** are the following matrixes,

$$\mathbf{T}=\begin{pmatrix}1 & 0 & 0\\ 0 & 1 & 0\\ 0 & 0 & 0\end{pmatrix}, \tag{3-3}$$

$$\mathbf{Z}=\begin{pmatrix}0 & 0 & 0\\ 0 & 0 & 0\\ 0 & 0 & 1\end{pmatrix}. \tag{3-4}$$

These relative permittivity tensor and permeability tensor are derived by using transformation optics.

In the simulation, rendering technique [5-12] is implemented to the geometrical ray tracing in order to evaluate the performance of the cloaking device. The performance is qualified by computing the cross-correlations as described in Eq. (3-5) [5],

$$C=\frac{\iint \frac{\left(f(x,y)-\langle f\rangle\right)}{\sigma(f)}\frac{\left(g(x,y)-\langle g\rangle\right)}{\sigma(g)}dxdy}{\iint\left(\frac{\left(f(x,y)-\langle f\rangle\right)}{\sigma(f)}\right)^2 dxdy}, \tag{3-5}$$

where $f(x,y)$ and $g(x,y)$ are the gray levels of the reference image without any hidden object and any cloak device, and the image with a hidden object and a cloak device, $\langle f\rangle$ and $\langle g\rangle$ are the spatial average values of f and g, and $\sigma(f)$ and $\sigma(g)$ are the values of the standard deviations of f and g. The integration was done in the region where the hidden object was seen without any cloaking device. For the case of the perfect cloaking, the value of C equals to 1.0. On the other hand, the decrease of value of C from 1.0 shows

deterioration of the performance of the cloaking device.

3.3. Numerical results

The results from the surface-mesh representation are compared with those from the rigorous function representation in order to verify the effectiveness of the proposed Hamiltonian ray tracing with the surface-mesh representation. Here, a spherical cloaking device and a cylindrical cloaking device are simulated as examples of cloaking devices.

Calculation models for the spherical cloaking device and the cylindrical cloaking device are illustrated in Figs. 3-2 and 3-3, respectively. In front of the cylinder-like object, the spherical object with a diameter of 10 mm is placed. The role of the spherical object is to disturb the visibility of an observer who looks at the cylinder-like object from the camera position. For the evaluation of the cloaking performances, the cloaking devices are placed to cover the spherical object. The inner diameter and the outer diameter of both the spherical device and the cylindrical cloaking device are 20 mm and 60 mm, respectively. The virtual point camera with a horizontal angle of view of 30°, a vertical angle of view of 22.5°, and a focal length of 50 mm is located at a distance of 150 mm from the center of the spherical object. The views of the camera are rendered by the Hamiltonian-based ray tracing.

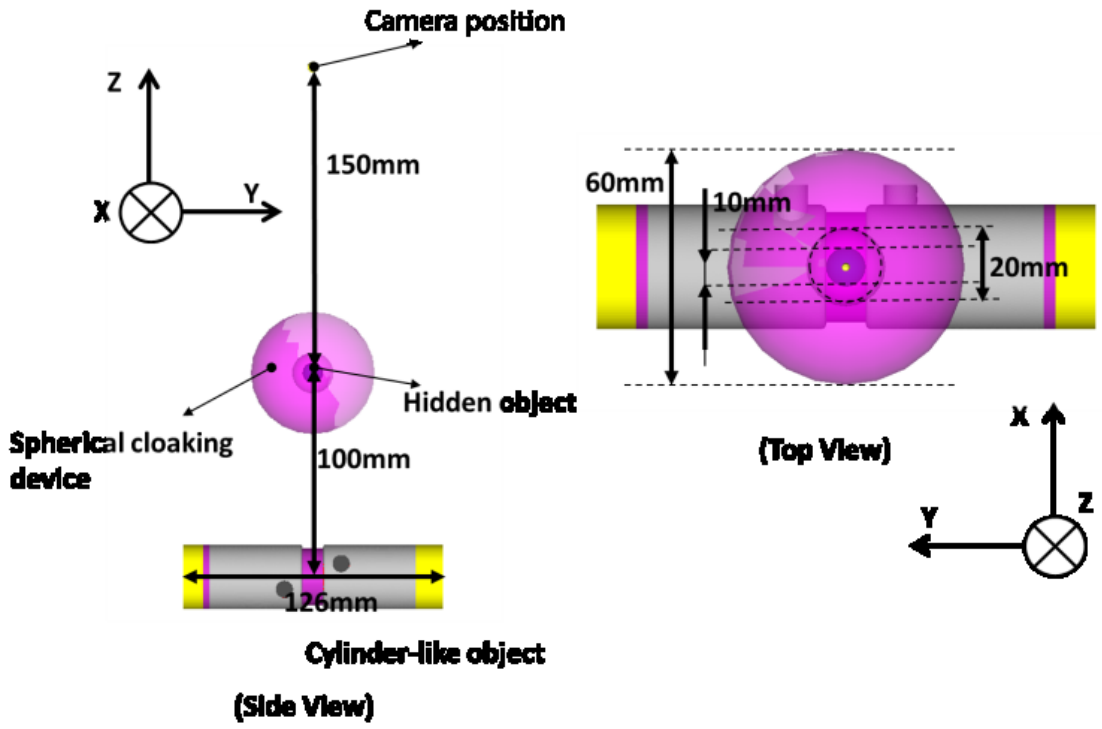

Fig. 3-2. Calculation model for the spherical cloaking.

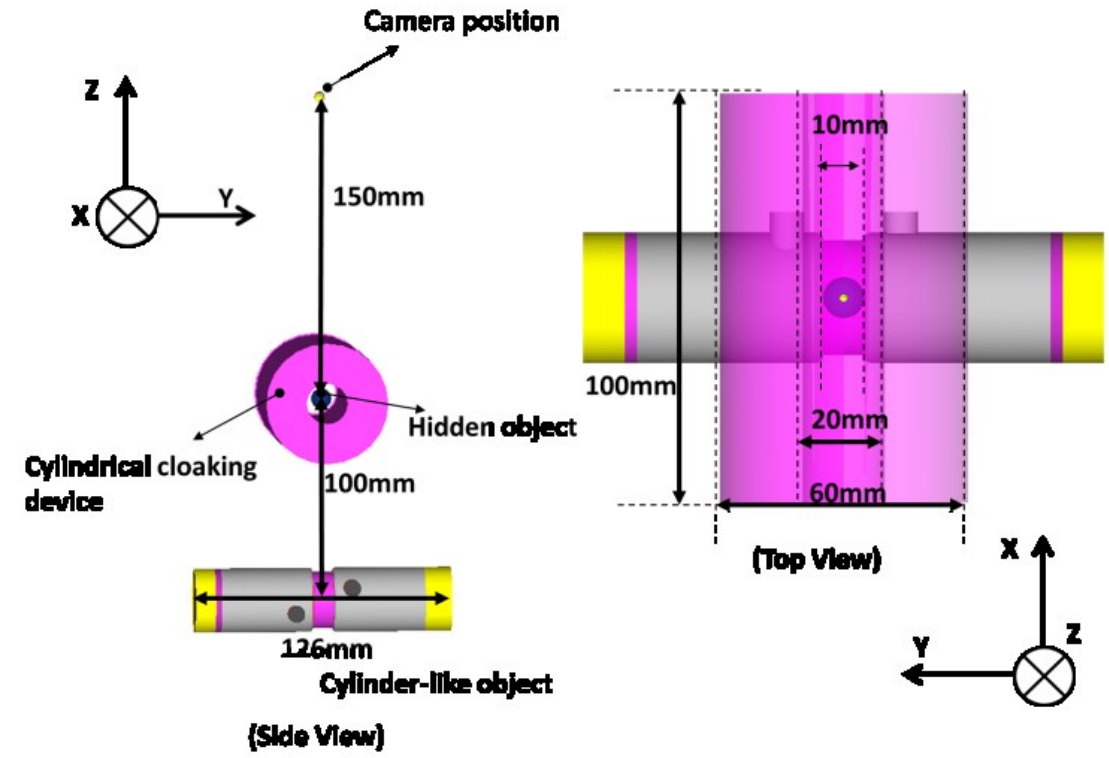

Fig. 3-3. Calculation model for the cylindrical cloaking.

3.3.1. Spherical cloaking

The rendered image without any cloaking device is depicted in Fig. 3-4(a). The spherical object to be hidden can be seen in Fig. 3-4(a). The rendered image for the spherical cloaking by the rigorous function representation is shown in Fig. 3-4(b). In Fig. 3-4(b), the spherical object to be hidden cannot be seen. In addition, no distortions of the image are found. The value of C is shown in Table 3.2., which shows C=1.00. Therefore, Fig. 3-4(b) and Table 3.2 reveal that the perfect cloaking can be obtained by the rigorous function representation.

The rendered image by the surface-mesh representation is depicted in Fig. 3-5(a), where the average length of sides of the triangle meshes is 5.0 mm (mesh1). Fig. 3-5(a) reveals that small distortion has occurred around the boundary. The distortion can also be verified from the value of C shown in Table 3-2. It is found that the value of C for the surface-mesh representation with mesh1 is smaller than that for the rigorous function representation. This suggests that the cloaking performance for the surface-mesh representation is lower than that for the rigorous function representation.

The reason for the distortion is considered to be due to the coarse surface-mesh resolution for representation of the surface of the cloaking device. The distortion should be suppressed because the distortion might affect the evaluation of a cloaking device. Accordingly, in order to suppress the distortion in the rendered image, rendering simulations with three kinds of refined mesh resolution, where the average lengths of sides of triangle meshes are 2.5 mm (mesh2), 1.0 mm (mesh3) and 0.5 mm (mesh4), have been executed.

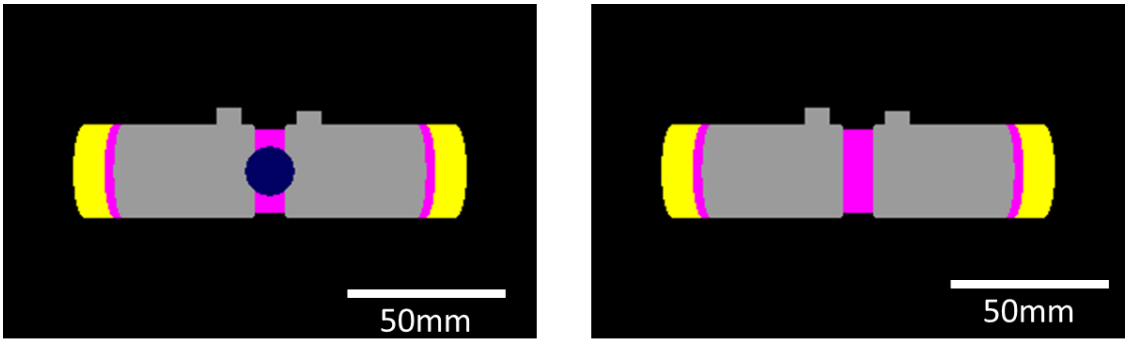

(a) (b)

Fig. 3-4. Rendered images (a) without cloaking device, (b) for spherical cloaking by the rigorous function representation approach and (c) for cylindrical cloaking by the rigorous function representation approach.

The rendered images for the spherical cloaking device with mesh2, mesh3 and mesh4 are shown in Figs. 3-5(b)-(d), respectively. Although the refinement of the mesh resolution from mesh1 to mesh3 through mesh2 is found to suppress the distortion in the rendered image, the effect of the refinement of the mesh resolution from mesh3 to mesh4 is found to be very small. The values of C shown in Table 3-2 support this finding. The value of C increases from mesh1 (C=0.72) to mesh2 (C=0.76) and from mesh2 to mesh3 (C=0.83) more significantly than from mesh3 to mesh4 (C=0.83).

Table 3-2: Cross-correlations for spherical cloaking.

Models		cross-correlations
rigorous function representation		1.00
surface-mesh representation	mesh1	0.72
	mesh2	0.76
	mesh3	0.83
	mesh4	0.83

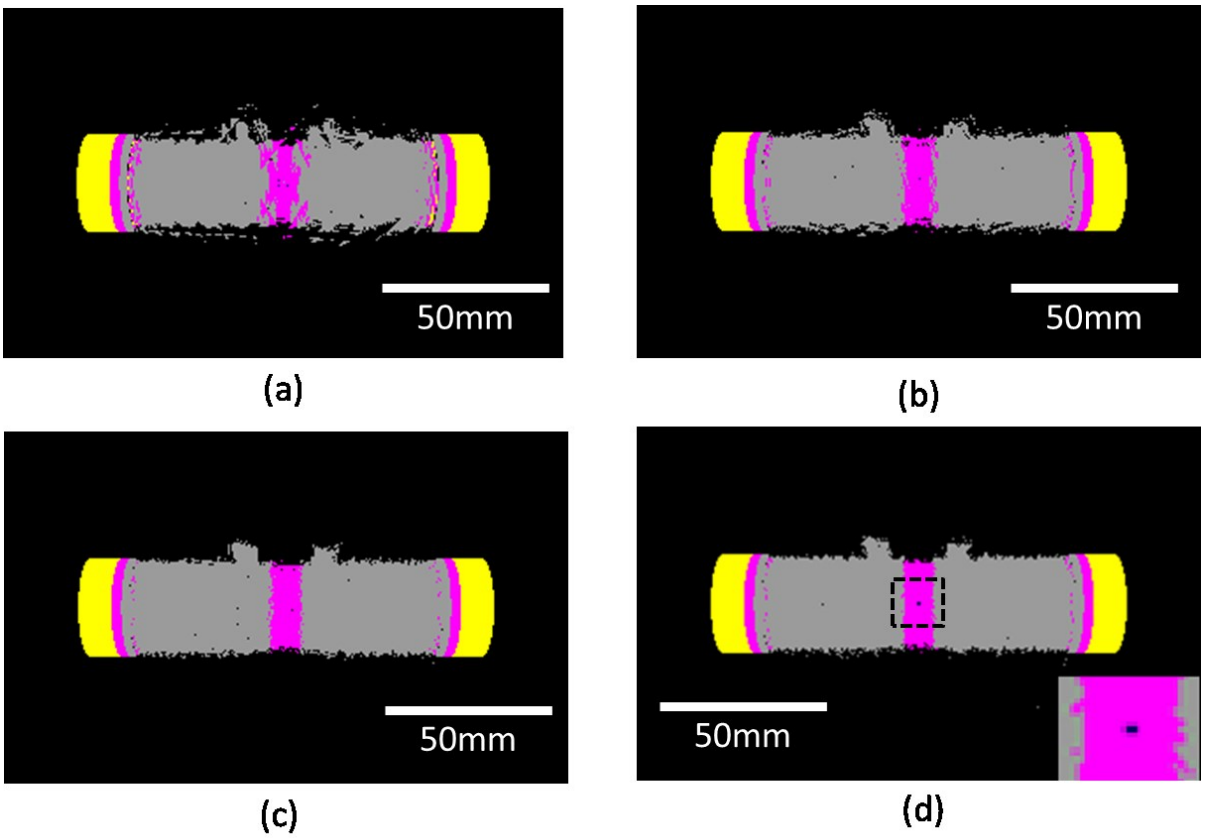

Fig. 3-5. Rendered images for spherical cloaking by the surface-mesh representation approach where the average lengths of sides of triangle meshes are (a) 5.0 mm, (b) 2.5 mm, (c) 1.0 mm, and (d) 0.5 mm.

3.3.2. Cylindrical cloaking

The rendered image for the cylindrical cloaking by the rigorous function representation approach is depicted in Fig. 3-6(a) and the rendered images by the surface-mesh representation approach with mesh1-4 are depicted in Figs. 3-6(b)-(e), respectively. Comparing Fig. 3-6(a) with Fig. 3-6(b), the distortion due to coarse surface-mesh resolution is seen with mesh1 in the case of cylindrical cloaking, too. Nevertheless, the refinement of the mesh resolution is found to suppress the distortion in the rendered image from Figs. 3-6(b)-(e). This finding can also be verified by the values of C shown in

Table 3-3.

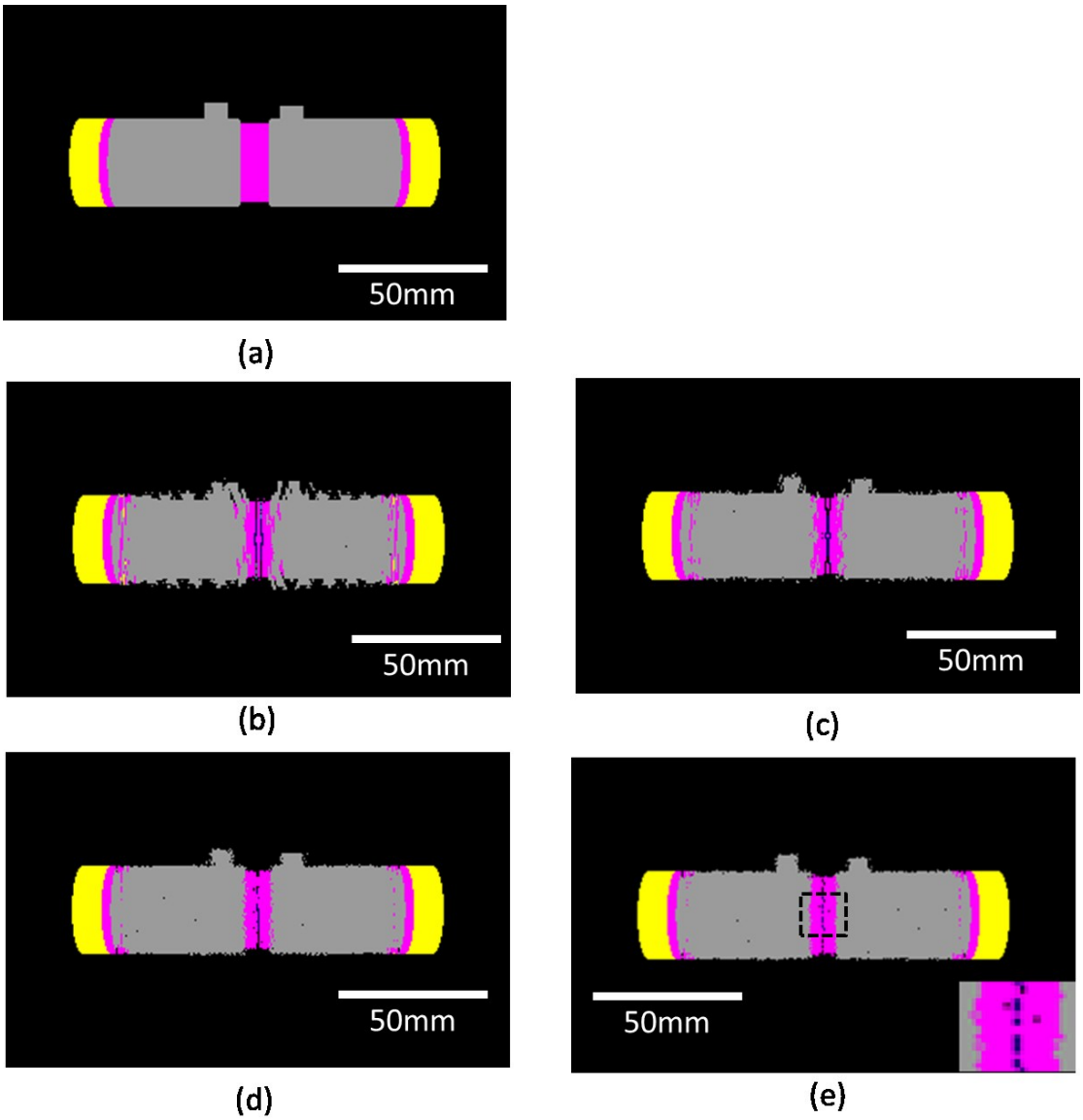

Fig. 3-6. Rendered images for cylindrical cloaking (a) by the rigorous function representation approach and by the surface-mesh representation approach where the average lengths of sides of triangle meshes are (b) 5.0 mm , (c) 2.5 mm, (d) 1.0 mm, and (e) 0.5 mm.

Table 3-3: Cross-correlations for cylindrical cloaking.

models		cross-correlations
rigorous function representation		1.00
surface-mesh representation	mesh1	0.60
	mesh2	0.60
	mesh3	0.72
	mesh4	0.76

3.4. Discussion

Comparing Table 3-2 with Table 3-3, it is found that the values of C of the spherical cloaking are larger than those of the cylindrical cloaking, which suggests that the distortion of the former is smaller than that of the latter. This is because the area of cloaking errors colored by deep blue, which is the color of the hidden object, is smaller in the spherical cloaking than in the cylindrical cloaking. In the case of the spherical cloaking, the cloaking errors are occurred as point-like as shown in Fig. 3-5(d), while in the case of the cylindrical cloaking, the cloaking errors are occurred in a straight line as shown in Fig. 3-6(e). Therefore, the former error is smaller than the latter error.

To illustrate how the cloaking errors are generated, the incident of the ray into the cloaking device as shown in Fig. 3-7(a) is considered. Since the normal vector of the surface in the surface-mesh representation is slightly different from that in the rigorous function representation, the direction of the refracted ray in the surface-mesh representation has an error from the correct direction. The error of the direction of the refracted ray causes the trajectory of the ray to change. Especially, some rays passing near the inner boundary incident into the inner boundary, and then refract out of the cloaking device as shown in Fig. 3-7(a). These rays finally incident the hidden object, resulting in the cloaking errors.

In the case of the spherical cloaking, by means of analysis of the ray trajectories, some rays passing near the inner boundary are found to incident into the cloaking device near the point P as shown in Fig. 3-7 (b). The point P is the cross point of the line, passing the center of the spherical cloaking device (O) and the camera position (C), and the outer boundary of the spherical cloaking device. Therefore, the deep blue point-like error region appeared near the point P. On the other hand, in the case of the cylindrical cloaking, some rays passing near the inner boundary are found to incident into the cloaking device near the line QR as shown in Fig. 3-7 (c). The line QR is the cross line of the plane S, passing the axis of the cylindrical cloaking device and the camera position (C), and the outer boundary of the cloaking device. Therefore, the error regions represented by deep blue becomes straight line appeared near the line QR. From the above results, it is found that it is necessary to employ very refine mesh resolution in order to suppress completely the distortion in the rendered image.

Here, the computational memory and the computational speed for the proposed Hamiltonian-based ray tracing are estimated. The calculation of the spherical cloaking device with a diameter of 60 mm requires less than 2.0 GB of memory. This suggests that the proposed Hamiltonian-based ray tracing can deal with large-scale objects with arbitrary shapes in terms of memory usages. On the other hand, in terms of computational speed, it takes approximately a day to obtain a rendered image by using 5 CPU cores (Intel Xeon E5-2687W 3.1GHz). Since the computational speed is in proportion to the number of CPU cores, sufficient computational speed for design of large-scale cloaking devices can be obtained by the parallel computation with more CPU cores.

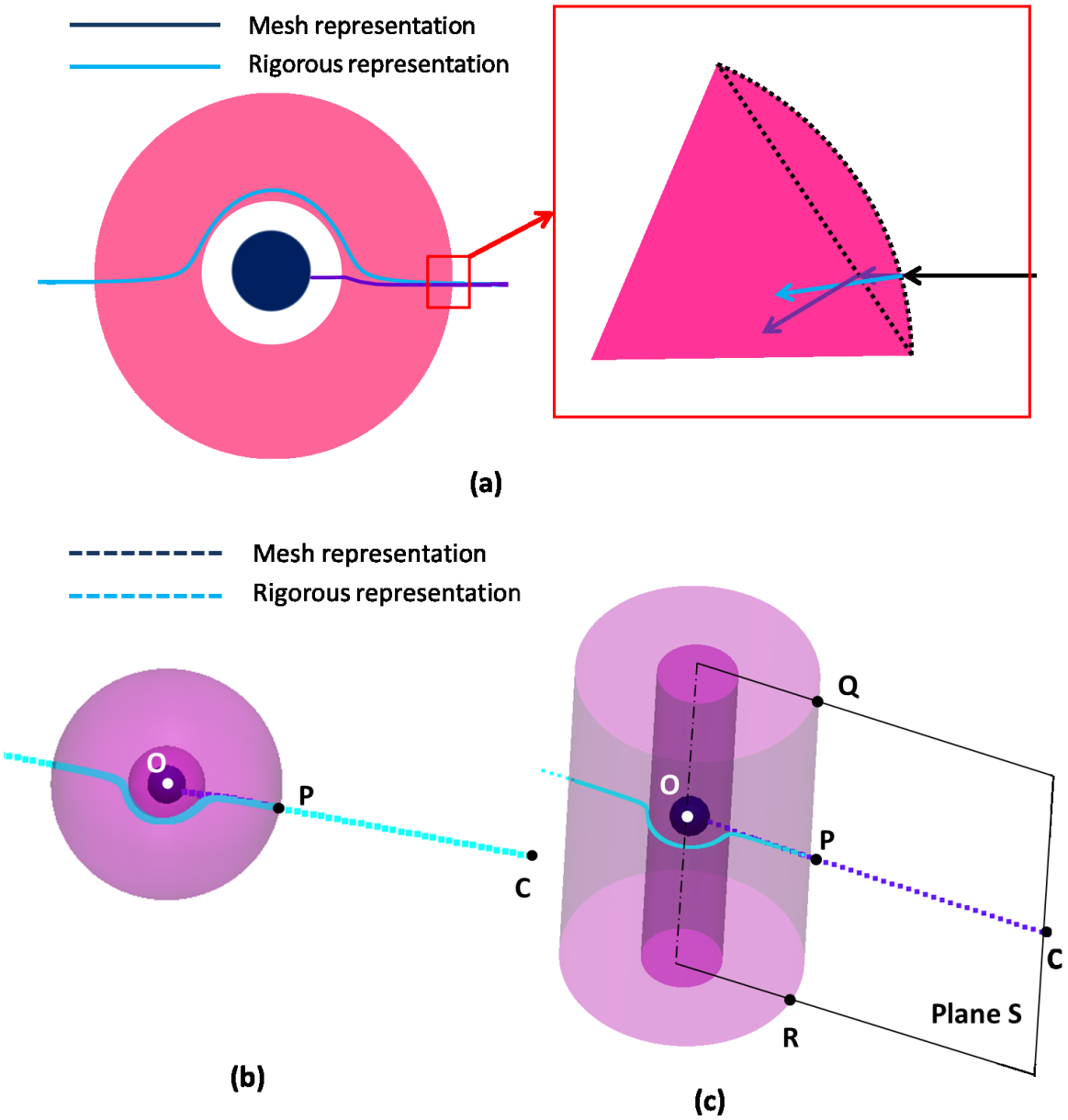

Fig. 3-7. The cloaking error in the surface-mesh representation (a). The Ray paths for the rigorous representation and the surface-mesh representation in the case of spherical cloaking (b) and cylindrical cloaking (c).

3.5. Conclusion

The simulation tool has been proposed for checking a cloaking device with an arbitrary shape by using Hamiltonian-based ray tracing. Since the media considered here are inhomogeneous and anisotropic in their electric permittivity and magnetic permeability, the ray trajectories have been calculated based on Hamiltonian equations. In order to make a model of the cloaking device with the arbitrary shape, the surface of the cloaking device is represented by triangular meshes.

In order to verify the proposed Hamiltonian ray tracing adapting the surface-mesh representation approach, the results from the surface-mesh representation approach have been compared with those from the approach where the surfaces of cloaking devices are represented by rigorous functions, adapting the spherical cloaking and the cylindrical cloaking as examples. From the comparison, it is found that the distortion due to the coarse mesh resolution has occurred with the surface-mesh representation approach, while by increasing the mesh resolution the distortion is suppressed. Because the distortion due to coarse mesh resolution might influence the evaluation of cloaking performance, it suggests that rendering simulations with high mesh resolution are necessary for accurate evaluation of cloaking performance.

References

1. X. Wang, S. Qu, S. Xia, B. Wang, Z. Xu, H. Ma, J. Wang, C. Gu, X. Wu, L. Lu, and H. Zhou, "Numberical Methods for Three-dimensional Electromagnetic Invisible Cloaks with Irregular Boundary Shapes," in Proceedings of Progress In Electromagnetics Research Symposium, 1649-1652 (2010).
2. X. Wang , S. Qu, S. Xia, B. Wang , Z. Xu, H. Ma, J. Wang, C. Gu, X. Wu, L. Lu, and H. Zhou, "Numerical method of designing three-dimensional open cloaks with arbitrary boundary shapes," Photonics and Nanostructures - Fundamentals and Applications **8**, 205–208 (2010).
3. X. Wang, S. Qu, Z. Xu, H. Ma, J. Wang, C. Gu, and X. Wu, "Three-dimensional invisible cloaks with arbitrary shapes based on partial differential equation," Appl. Math. Comput. **216**, 426-430 (2010).
4. D. Schurig, J. B. Pendry, and D. R. Smith, "Calculation of material properties and ray tracing in transformation media," Opt. Express **14**, 9794–9804 (2006).
5. J.C. Halimeh, and M. Wegener, "Photorealistic rendering of unidirectional free-space invisibility cloaks", Opt. Express **21**, 9457–9472 (2013).
6. J. C. Halimeh and M. Wegener, "Time-of-flight imaging of invisibility cloaks," Opt. Express **20**, 63–74 (2012).
7. J. C. Halimeh, R. Schmied, and M. Wegener, "Newtonian photorealistic ray tracing of grating cloaks and correlation-function-based cloaking-quality assessment", Opt. Express **19**, 6078–6092 (2011).
8. J. C. Halimeh, and M. Wegener, "Photorealistic ray tracing of free-space invisibility cloaks made of uniaxial dielectrics", Opt. Express **20**, 28330–28340 (2012).
9. G. Dolling, M. Wegener, S. Linden, and C. Hormann, "Photorealistic images of objects in effective negative-index materials," Opt. Express **14**, 1842–1849 (2006).

10. J. C. Halimeh, R. T. Thompson, and M. Wegener, “Invisibility cloaks in relativistic motion.” Phys. Rev. A 93, 013850 (2016).
11. J. C. Halimeh, and R. T. Thompson, “Fresnel-Fizeau drag: Invisibility conditions for all inertial observers,” arXiv:1601.04218.
12. A. J. Danner, “Visualizing invisibility: Metamaterials-based optical devices in natural environments,” Opt. Express **18**, 3332–3337 (2010).
13. Y. Jiao, S. Fan, and D. A. B. Miller, “Designing for beam propagation in periodic and nonperiodic photonic nanostructures: Extended Hamiltonian method,” Phys. Rev. E 70, 036612 (2004).
14. A. Alireza, and A. J. Danner, “Generalization of ray tracing in a linear inhomogeneous anisotropic medium: a coordinate-free approach,” J. Opt. Soc. Am. A **27**, 2558–2562 (2010).

CHAPTER 4

Full-mesh Representation with Hamiltonian-based Ray-tracing Method

4.1. Introduction

There are two technical issues to be solved in order to simulate cloaking devices with arbitrary large-scale shapes by the Hamiltonian-based ray-tracing [1-11]. One issue is how to represent the surfaces of cloaking devices with arbitrary shapes. In CHAPTER 3, a Hamiltonian-based ray-tracing method with surface-mesh representation, where the surfaces of arbitrary shapes are represented by the mesh structure as shown in Fig. 4-1 (a), has been proposed. It has been found that the surface-mesh representation with fine mesh resolution yields the similar cloaking performance to rigorous function representation, where the surfaces of cloaking devices are represented by analytical functions. The other issue is how to determine the constitutive parameters of cloaking devices with arbitrary shapes. This issue is expected to be solved by the numerical technique based on the finite element method (FEM) for the calculation of the constitutive parameters proposed in [12].

In this chapter, the FEM-based numerical modeling of the constitutive parameters is integrated into the Hamiltonian-based ray tracing through full-mesh representation, where both the surface and the inner part of a cloaking device are represented by the mesh

structure as shown in Fig. 4-1(b). The full-mesh representation is verified by comparing it with the rigorous function representation and the surface-mesh representation with respect to the performance of cylindrical cloaking. Subsequently, the full-mesh representation is applied to the evaluation of examples of cloaking devices with arbitrary shapes.

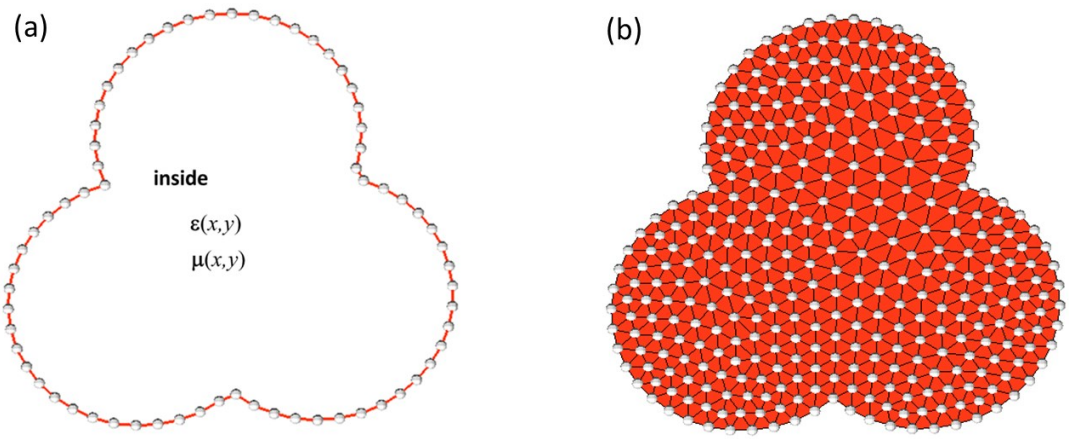

Fig. 4-1. (a) Example of linear meshes that represent the surfaces of the cloaking device. (b) Example of triangular meshes inside of the cloaking device.

4.2. Full-mesh representation of cloaking device and evaluation method for cloaking performance

The numerical technique with the FEM-based solution of the Laplace's equation [12], which is explained in 2.2., is employed to calculate ε and μ of cloaking devices with arbitrary shapes. The distributions of ε and μ obtained from the FEM-based solutions are discretized in triangular meshes inside of the cloaking device. In order to implement the discretized distributions of ε and μ into the Hamiltonian-based ray tracing, the full-mesh representation of cloaking devices as shown in Fig. 4-1 (b) is required. Additionally, since ε and μ at any position in cloaking devices are required for the Hamiltonian-based

ray tracing, interpolation between the discretized ε and μ is necessary. In the full-mesh representation, ε and μ are interpolated by linear functions of the components of the position vector inside each element employed for the solution of the Laplace's equation.

A calculation model is depicted in Fig. 4-2. One hundred rays are radiated from the point located in front of the cloaking device, within an angle of view of 60°. The ray trajectories are calculated by the Hamiltonian-based ray tracing described in 2.1. If the incidence of a ray into the inner surface of the cloaking device occurs, the ray is supposed to be absorbed by the surface. The screen for the observation of the rays is located on the back of the cloaking device as shown in Fig. 4-2. Each of the intersection points of the rays and the screen for successful cloaking is close to that without the cloaking device. By contrast, each of the intersection points for unsuccessful cloaking is different from that without the cloaking device.

For the evaluation of cloaking performance, the angle between the straight line passing the source point and the intersection point, and the y axis as shown in Fig. 4-3, is considered. The performance of the cloaking device is qualified by the root mean squared error between the angles with the cloaking device and without the cloaking device given by

$$\Delta\theta = \sqrt{\frac{\sum_{\alpha}^{N_{ray}} \left(\theta_\alpha - \theta_\alpha^{ref}\right)^2}{N_{ray}}}, \tag{4-1}$$

where α is the index of a ray, θ_α and $\theta^{ref}{}_\alpha$ are the angle with the cloaking device and without the cloaking device, respectively. N_{ray} is the number of the total rays. N_{ray} is set to be 100. The dependence of cloaking performance on the radiation angle is calculated by

$$\Delta\theta_\alpha = \left|\theta_\alpha - \theta_\alpha^{ref}\right|. \tag{4-2}$$

If the calculated value of $\theta_\alpha - \theta^{ref}{}_\alpha$ is out of the range $-30° < \theta_\alpha - \theta^{ref}{}_\alpha < 30°$ or the ray doesn't intersect the screen, the value of $|\theta_\alpha - \theta^{ref}{}_\alpha|$ is set to be 30°. $\Delta\theta$ of 0.0° reveals that perfect cloaking is obtained. On the other hand, large values of $\Delta\theta$ indicate the degradation of the performance of the cloaking device.

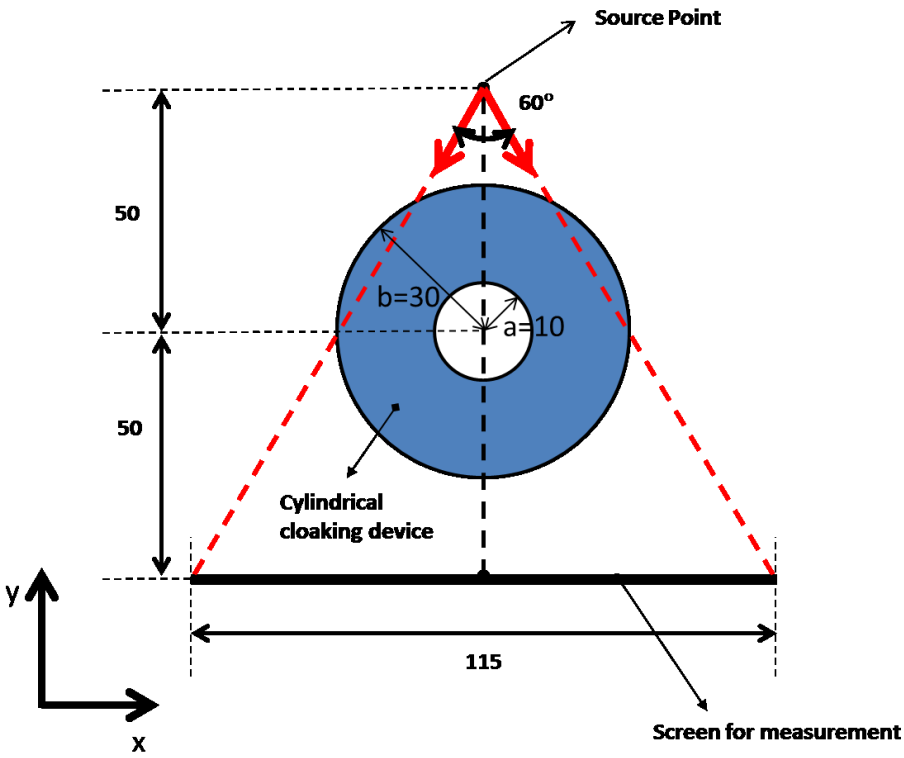

Fig. 4-2. Calculation model for the cylindrical cloaking device.

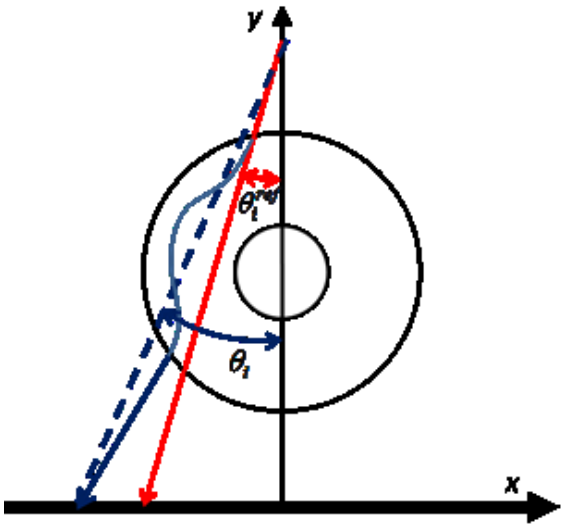

Fig. 4-3. The angle for the evaluation of cloaking performance. The red solid arrow corresponds to the ray trajectory without the cloaking device. The blue solid arrow corresponds to the ray trajectory with the cloaking device. The blue dashed line is the straight line passing the source point and the intersection point between the ray trajectory and the screen.

4.3. Numerical results and discussion

In this section, the full-mesh representation is verified by comparing with the rigorous function representation and the surface-mesh representation with respect to the performance of cylindrical cloaking. Subsequently, examples of cloaking devices with arbitrary shapes are evaluated by the full-mesh representation.

4.3.1. Cloaking performance of rigorous function representation and surface-mesh representation

In this subsection, ideal cloaking features are given by evaluation of the cloaking performance of cylindrical cloaking with the rigorous function representation and the

surface-mesh representation. In the rigorous function representation, both the geometry of the surface and the values of ε and μ inside the device are represented by analytical functions, whereas in the surface-mesh representation, the geometry of the surface is represented by meshes and the values of ε and μ inside the device are represented by analytical functions. The values of ε and μ inside the cloaking device are given by the analytical functions of the position vector, $\boldsymbol{r}=(x,y)$, as shown in Eq. (2-52). The results present the ideal performances for the verification of the full-mesh representation in 4.3.2.

The cloaking performances are evaluated by the surface-mesh representation approach with six kinds of surface-mesh resolution where the average lengths are 2.5, 1.0, 0.5, 0.25, 0.10, and 0.05 mm.

Here, the relative mesh resolution is defined as the ratio of the mesh size to the size of the cloaking device. Therefore, it can be universally applied to any other structure. When the size of the cloaking device is 60 mm and the mesh sizes are 2.5, 1.0, 0.5, 0.25, 0.10, and 0.05 mm, the relative mesh resolutions correspond to 4.17e–02, 1.67e–02, 8.33e–03, 4.17e–03, 1.67e–03, and 8.33e–04, respectively. Hereafter, the numerical results are investigated based on the relative mesh resolution.

The ray trajectories without a cloaking device are depicted in Fig. 4-4 (a), while those with the cloaking device calculated by the rigorous function representation are depicted in Fig. 4-4 (b). It is found that the ray trajectories after passing through the cloaking device shown in Fig. 4-4 (a) and the corresponding ray trajectories shown in Fig. 4-4 (b) are almost identical. The dependence of the cloaking performance on the radiation angle for the rigorous function approach is illustrated in Fig. 4-5. This suggests that the cloaking performance gets degraded in little amounts at radiation angles close to 0°. Table 4-1 shows performances of cylindrical cloaking for the rigorous function

representation and the surface-mesh representation. It indicates that the value of $\Delta\theta$ for the rigorous function approach, $\Delta\theta$=7.90e–05°, is very close to 0.0°, which suggests that the rigorous function representation yields the almost perfect cloaking.

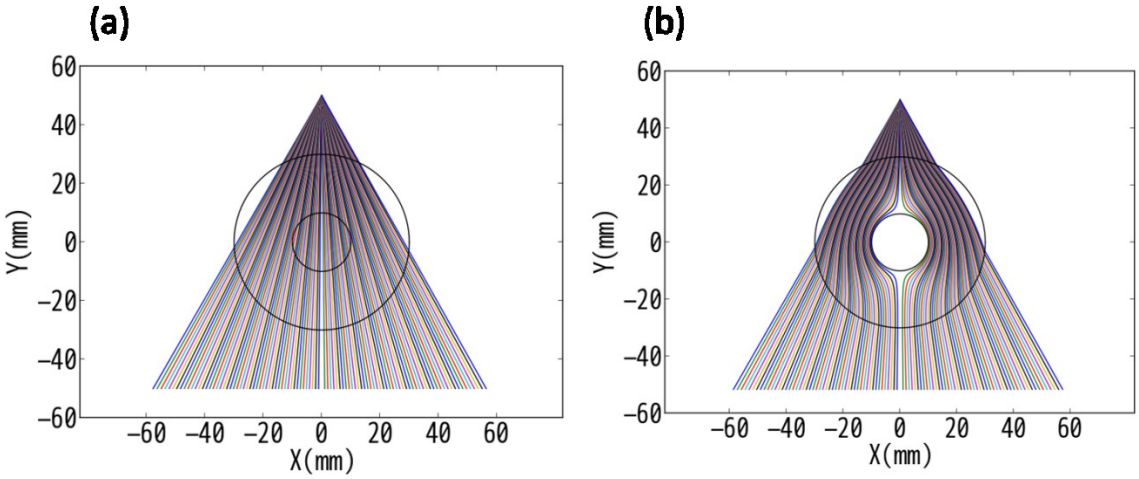

Fig. 4-4. (a) The ray paths without a cloaking device. (b) The ray paths with the cylindrical cloaking device calculated by the rigorous function representation.

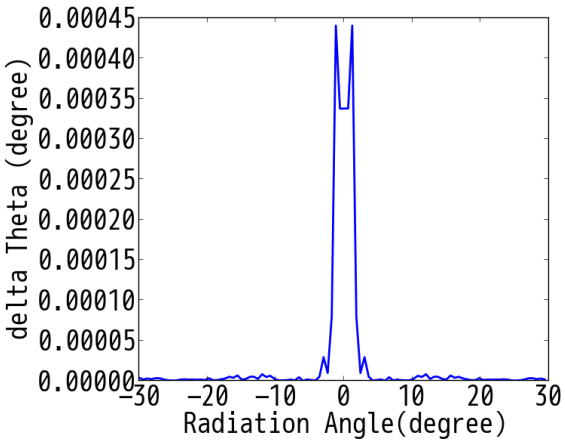

Fig. 4-5. The dependence of the cloaking performance on the radiation angle calculated by the rigorous function representation.

The ray trajectories calculated by the surface-mesh representation with the six surface-mesh resolutions are shown in Figs. 4-6 (a)-(f), respectively. The dependence of the performance on the surface-mesh resolution calculated based on the ray trajectories is shown in Table 4-1. It reveals that the performance is improved as the surface-mesh resolution becomes finer.

The reason why the degraded performance is obtained for the coarse surface-mesh resolution can be considered as follows. Since the normal vector of the surface in the surface-mesh representation slightly differs from that in the rigorous function representation, an error in the direction of the refracted ray occurs in the surface-mesh representation. The error of the direction of the refracted ray causes the change of the ray trajectory, resulting in the degraded cloaking performance.

The dependence of the cloaking performance on the radiation angle for six relative mesh resolutions is depicted in Figs. 4-7 (a)-(f), respectively. It can be noticed that the cloaking performance oscillates with the radiation angle. Furthermore, the amplitude and the period of the oscillation are found to be reduced as the relative mesh resolution becomes finer.

The reason for the oscillation can be explained by the two ray trajectories for the relative mesh resolution of 4.17e–02 shown in Fig. 4-8. The red trajectory at a radiation angle of –27.9° yields degraded performance while the blue trajectory at a radiation angle of –26.3° yields high performance. From Fig. 4-8, the difference between the two trajectories in the position of the intersection point of the ray and the surface can be noticed. The intersection point of the red ray and the surface is near the end of the surface-mesh. In contrast, the intersection point of the blue ray and the surface is at the middle of the surface-mesh.

From the geometrical consideration illustrated in Fig. 4-8, the difference of the normal

vector at the intersection point in the surface-mesh representation and that in the rigorous function representation is considered to become larger for the intersection point near the end of the surface-mesh than for that at the middle of the surface-mesh. The large difference of the normal vectors in the surface-mesh representation and in the rigorous function representation leads to the inaccuracy of the direction of the refracted ray, resulting in degraded performance as mentioned above. On the other hand, the small difference of the normal vectors leads to high performance. Therefore, since the position of the intersection point has an influence on the cloaking performance, the cloaking performance oscillates with the radiation angle as shown in 4-7 (a)-(f).

The difference of the normal vectors becomes smaller for the smaller size of the surface-mesh, that is, the finer surface-mesh resolution, leading to the smaller inaccuracy. Therefore, the amplitude of the oscillation of the cloaking performance is decreased for the finer surface-mesh resolution. Furthermore, the period of the oscillation of the cloaking performance is determined by the size of the surface-mesh. That is, the smaller size of the surface-mesh yields the shorter period of the oscillation.

Here, a criterion for high cloaking performance is set to $\Delta\theta$=1.0°. From Table 4-1, it is found that the relative mesh resolution of the surface finer than 4.17e–03 can fulfill the criterion.

Table 4-1: Performances of cylindrical cloaking calculated for the rigorous function representation and the surface-mesh representation.

Number	Representation	Relative Mesh Resolution	Δθ (°)
1	Rigorous function	-	7.99e–05
2	Surface-Mesh	4.17e–02	0.586
3		1.67e–02	0.270
4		8.33e–03	0.115
5		4.17e–03	0.0560
6		1.67e–03	0.0244
7		8.33e–04	0.0114

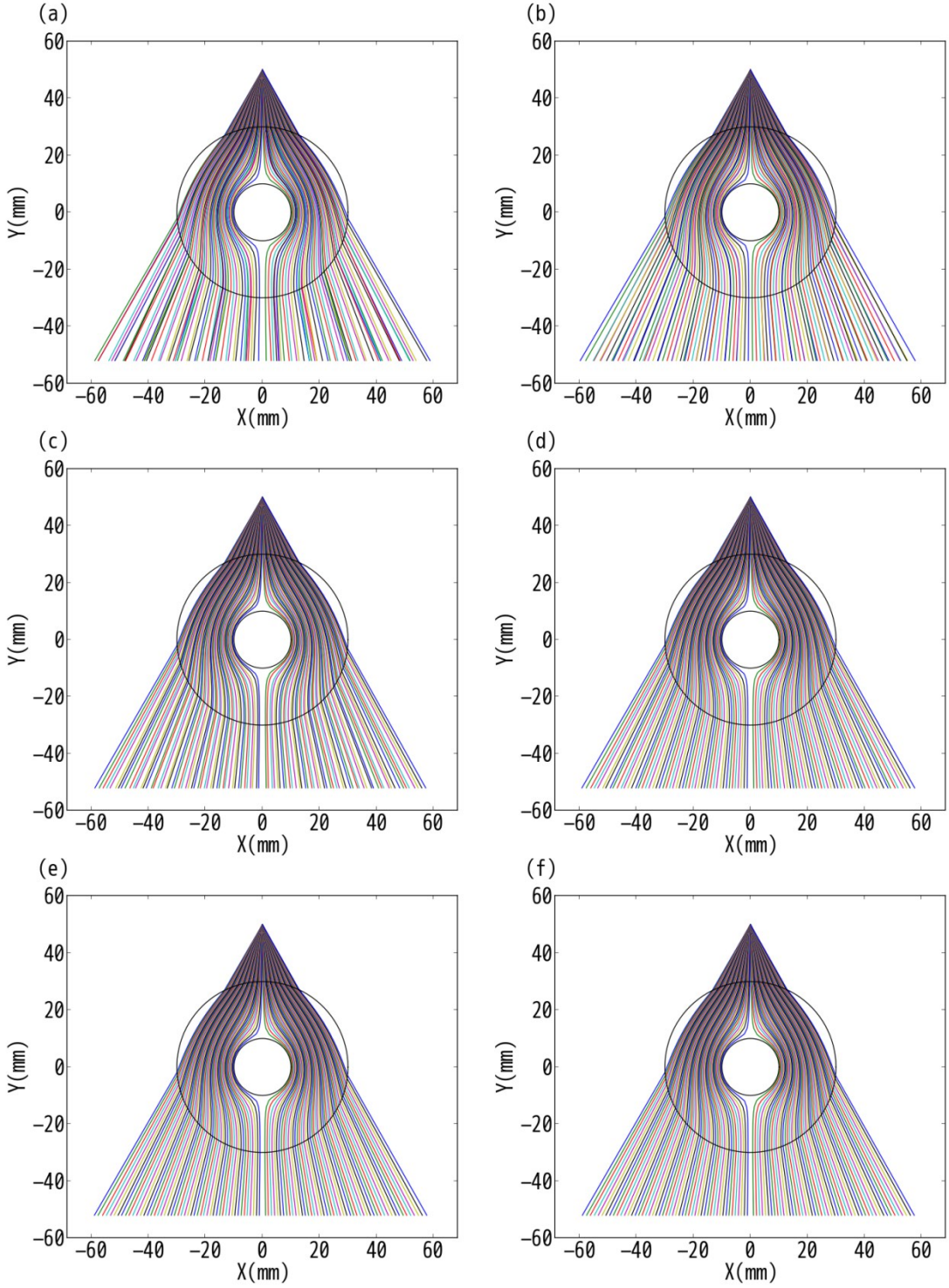

Fig. 4-6. The ray trajectories with the cylindrical cloaking device for the surface-mesh representation. The relative surface-mesh resolutions are (a) 4.17e–02, (b) 1.67e–02, (c) 8.33e–03, (d) 4.17e–03, (e) 1.67e–03, and (f) 8.33e–04.

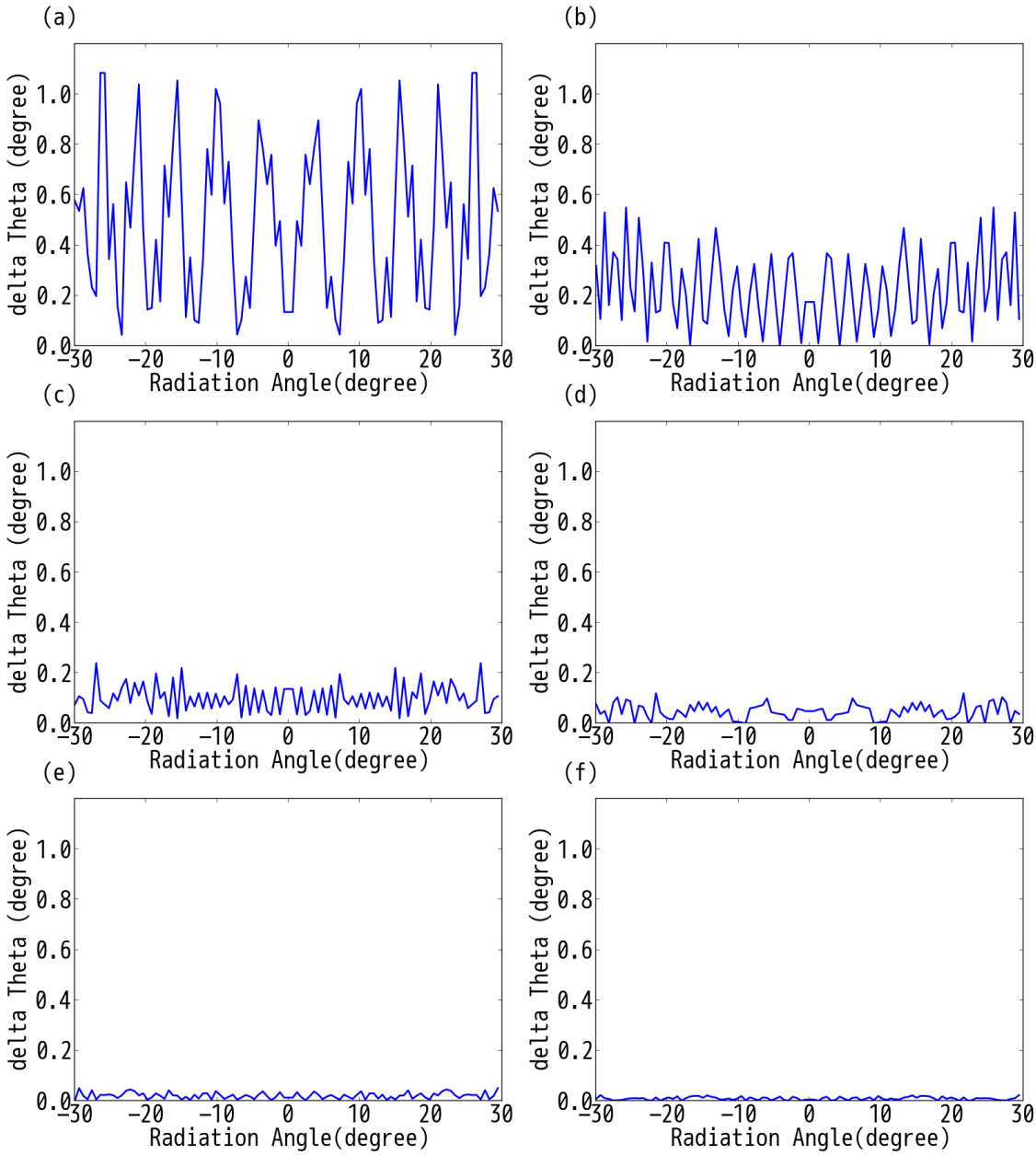

Fig. 4-7. The dependence of the cloaking performance on the radiation angle for the surface-mesh representation The relative surface-mesh resolutions are(a) 4.17e–02, (b) 1.67e–02, (c) 8.33e–03, (d) 4.17e–03, (e) 1.67e–03, and (f) 8.33e–04.

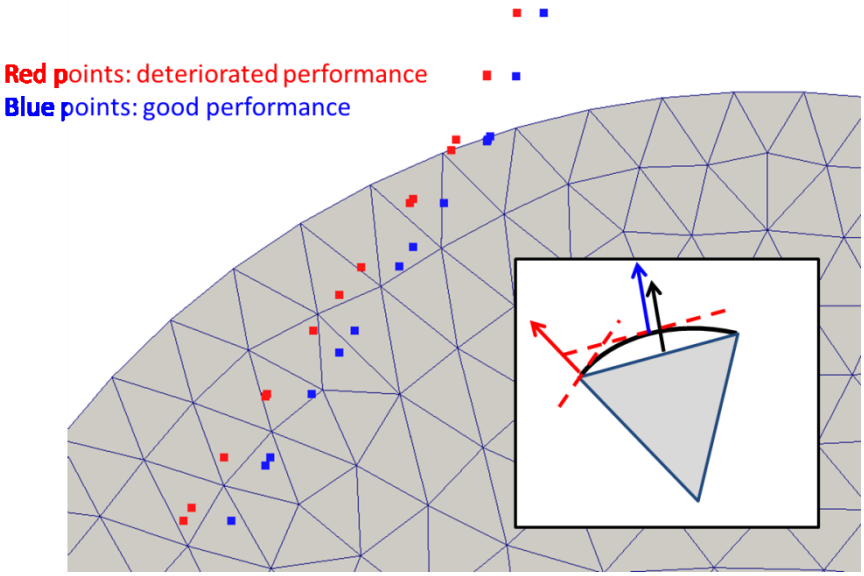

Fig. 4-8. The explanation for the oscillation of the perfomance with the radiation angle in Fig. 4-7.

4.3.2. Cloaking performance of full-mesh representation

The numerical technique for the calculation of ε and μ described in 2.2 relies on the FEM-based solution of the Laplace's equation. Therefore, the full-mesh resolution of a cloaking device is considered to contribute the cloaking performance. Here, the dependence of cloaking performance on the full-mesh resolution is investigated by calculating the cloaking performance of cylindrical cloaking with six full-mesh resolutions where the average lengths are 2.5, 1.0, 0.5, 0.25, 0.10, and 0.05 mm. Their relative mesh resolutions correspond to 4.17e–02, 1.67e–02, 8.33e–03, 4.17e–03, 1.67e–03, and 8.33e–04.

The ray trajectories calculated for the six full-mesh resolutions are depicted in Figs. 4-9 (a)-(f), respectively. The dependence of the cloaking performance on the radiation angle for the six full-mesh resolutions is shown in Figs. 4-10 (a)-(f), respectively. From

Fig. 4-9 and Fig. 4-10, it can be seen that some ray trajectories near the radiation angle of 0° are significantly degraded from the ideal ones at the full-mesh resolution from 4.17e–02 to 4.17e–03. However, as the full-mesh resolution gets finer, the number of the largely deviated rays decreases. Eventually, at the full-mesh resolution of 1.67e–03, largely deviated rays disappear. The dependence of the cloaking performance on the full-mesh resolution is shown in Table 4-2 and Fig. 4-11. It is found that the finer full-mesh resolution reveals the higher cloaking performance. It is noted that the cloaking performances at the full-mesh resolutions of 1.67e–03 and 8.33e–04 are comparable to those for the surface-mesh representation.

From the above results, it is confirmed that a full-mesh representation with a relative resolution finer than 1.67e–03 can yield the performance comparable to the surface-mesh representation.

Table 4-2: Performances of cylindrical cloaking devices calculated for the full mesh representation with the interpolation of the FEM-based solution of the Laplace's equation.

Number	Representation	Relative Mesh Resolution	Δθ (°)
1	Full-Mesh (Interpolation ofThe FEM solution of Laplace's Eqn)	4.17e–02	12.1
2		1.67e–02	5.19
3		8.33e–03	4.51
4		4.17e–03	1.43
5		1.67e–03	0.113
6		8.33e–04	0.0803

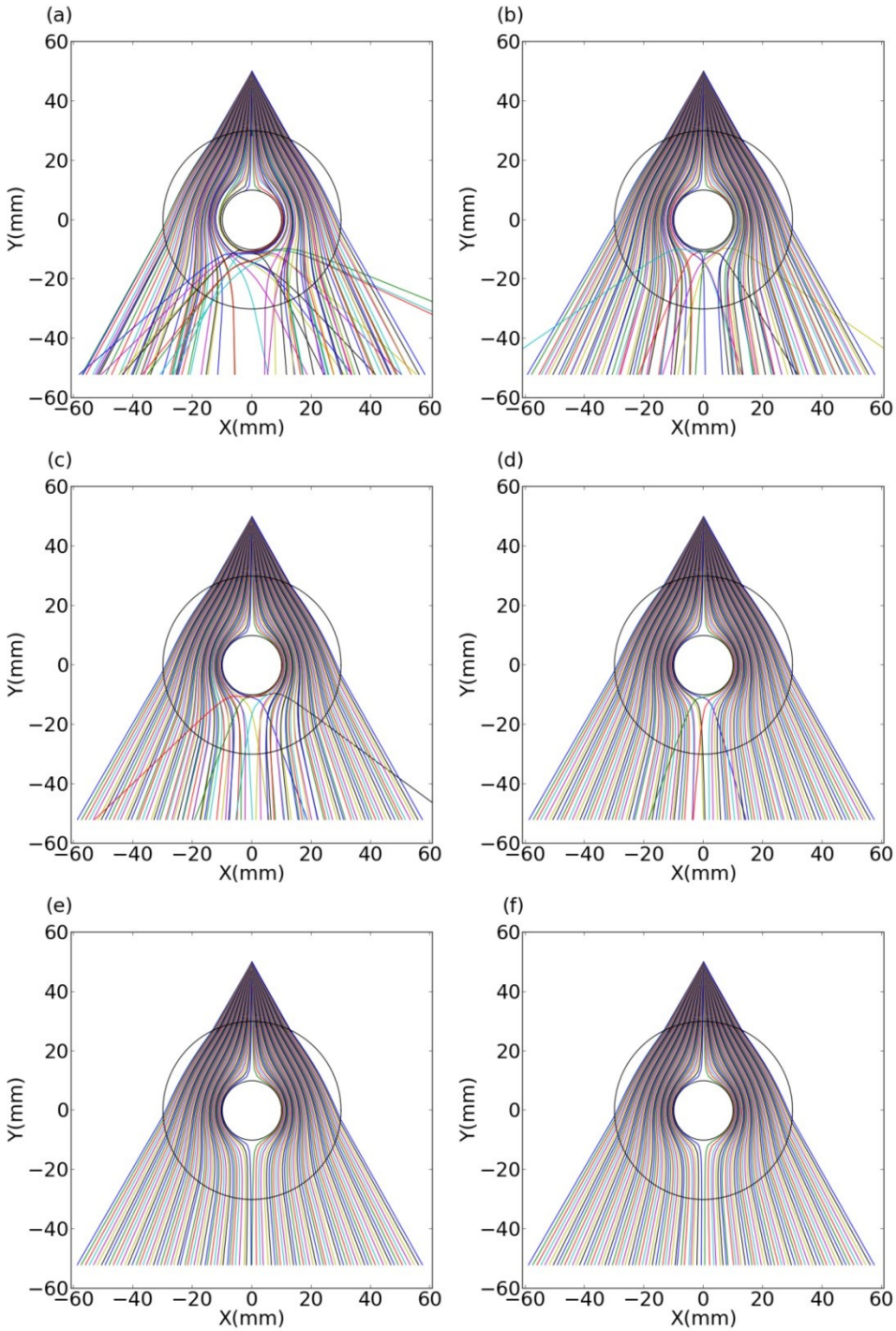

Fig. 4-9. The ray trajectories with the cylindrical cloaking device for the full-mesh representation with the interpolation of the FEM-based solution of the Laplace's equation. The relative full-mesh resolutions are (a) 4.17e–02, (b) 1.67e–02, (c) 8.33e–03, (d) 4.17e–03, (e) 1.67e–03, and (f) 8.33e–04.

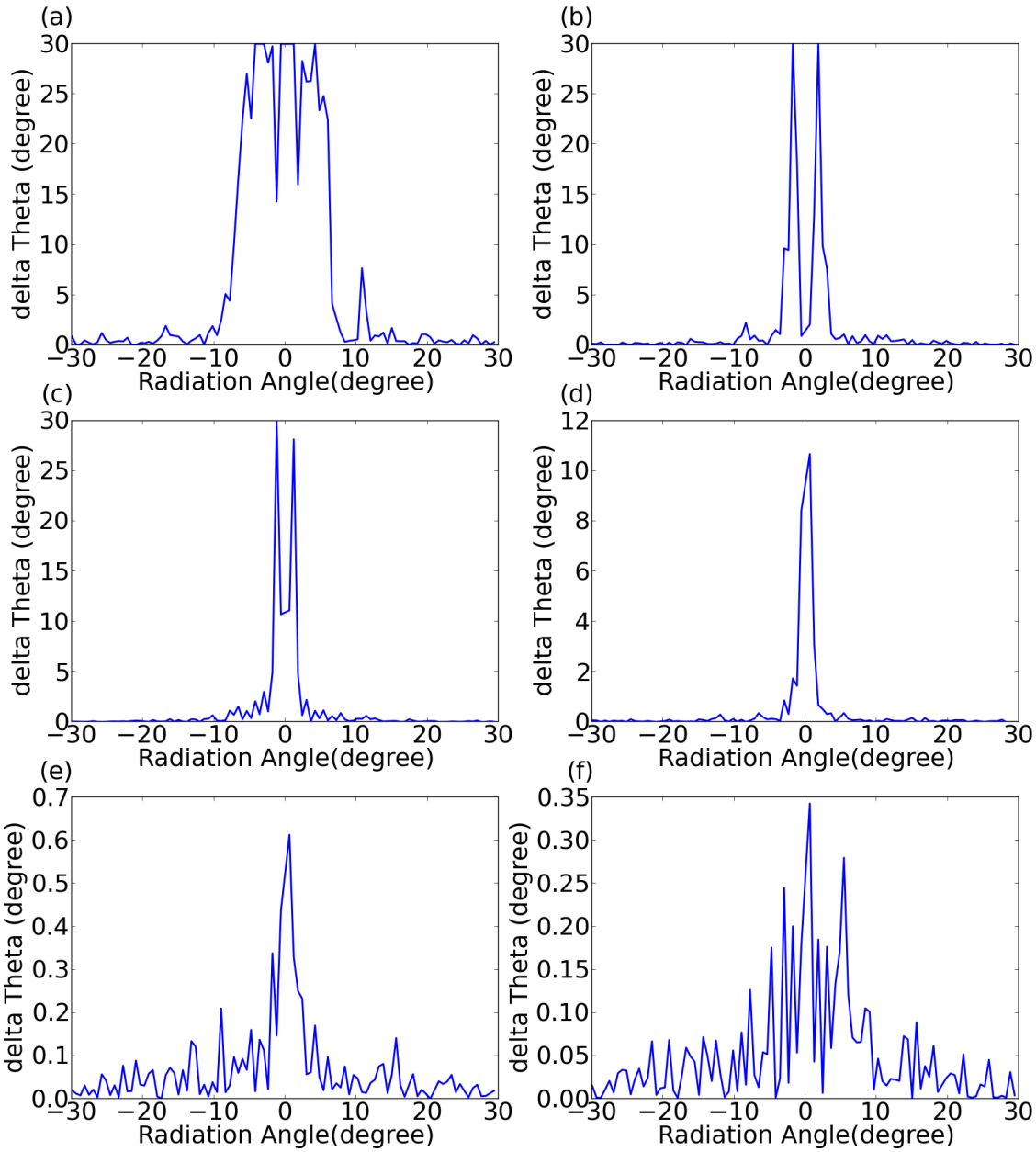

Fig. 4-10. The dependence of the cloaking performance on the radiation angle for the full-mesh representation with the FEM-based solution of the Laplace's equation. The relative full-mesh resolutions are (a) 4.17e–02, (b) 1.67e–02, (c) 8.33e–03, (d) 4.17e–03, (e) 1.67e–03, and (f) 8.33e–04.

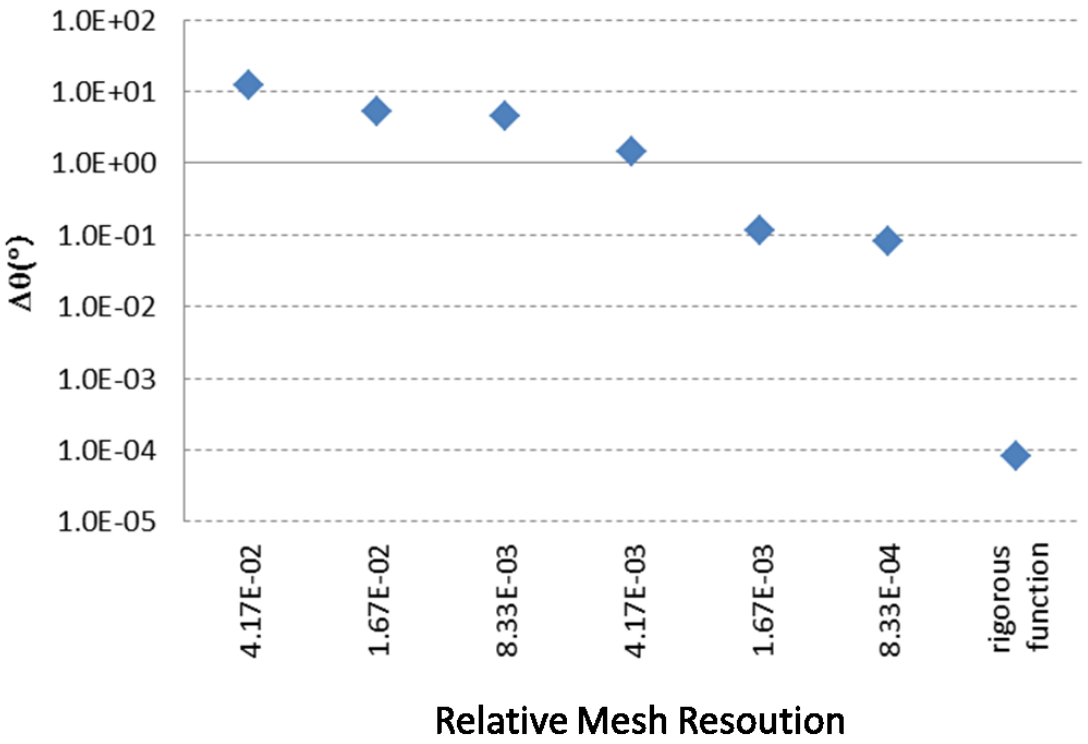

Fig. 4-11. The dependence of the cloaking performance on the full-mesh resolution.

4.3.3. Accuracy of full-mesh representation

ε and μ in the full-mesh representation are represented by the interpolation function using the values of the FEM solution. Therefore, there are two types of the accuracy of ε and μ in the full-mesh representation. One type is the accuracy of the FEM, that is, how close the FEM solution is to the rigorous solution. The other type is the accuracy of the interpolation, that is, how close the interpolation function is to the rigorous function.

Figure 4-12 illustrates the two types of accuracy schematically. As the full-mesh resolution gets finer, both of the two types of accuracy are improved, suggesting that ε and μ in the full-mesh representation converge to those in the rigorous function. ε and μ with the best accuracy of the FEM at a certain accuracy of the interpolation corresponds

to those represented by the interpolation function using the values of the rigorous solution of the Laplace's equation. Therefore, the accuracy of the FEM can be investigated by comparing the cloaking performance for ε and μ represented by the linear interpolation of the values of the FEM solution and that for ε and μ represented by the linear interpolation of the values of the rigorous solution at the same full-mesh resolution, as illustrated by the green arrow in Fig. 4-12. On the other hand, the accuracy of the interpolation is investigated by comparing the cloaking performance for ε and μ represented by the interpolation function using the values of the rigorous solution at various full-mesh resolutions, as illustrated by the blue arrow in Fig. 4-12, since no error in terms of the accuracy of the FEM is included in the rigorous solution. Therefore, if the cloaking performance for ε and μ represented by the interpolation function using the values of the rigorous solution is obtained, the accuracy can be divided into the accuracy of the FEM and the accuracy of the interpolation.

Rigorous function

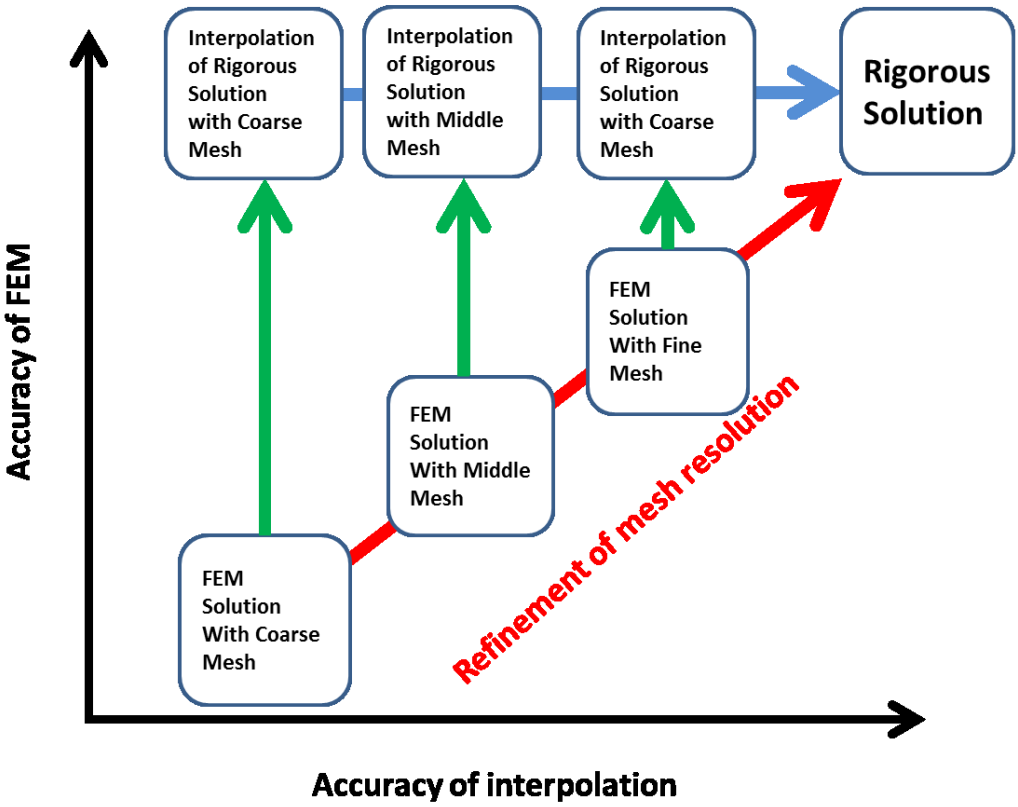

Fig. 4-12. Two types of accuracy in the full-mesh resolution: the accuracy of the interpolation and the accuracy of the FEM.

In order to divide the accuracy into the two types, the cloaking performance of cylindrical cloaking with six relative full-mesh resolutions, 4.17e–02, 1.67e–02, 8.33e–03, 4.17e–03, 1.67e–03, and 8.33e–04, is calculated by employing ε and μ represented by linear interpolations of the values of the rigorous solution of the Laplace's equation.

The ray trajectories calculated with the six relative full-mesh resolutions are illustrated in Figs. 4-13 (a)-(f), respectively. The dependence of the cloaking performance on the full-mesh resolution is shown in Table 4-3. Figure 4-13 and Table 4-3 indicate that low accuracy of the interpolation degrade the cloaking performance significantly.

The dependence of the cloaking performance on the radiation angle for the six relative

full-mesh resolutions is depicted in Figs. 4-14 (a)-(f), respectively. From Fig. 4-14, the difference of the accuracy of the interpolation is distinct in small radiation angles, which correspond to the significantly errored ray trajectories depicted in Fig. 4-13.

Table 4-3: Performances of cylindrical cloaking devices calculated for the full mesh representation with the interpolation of the rigorous solution of the Laplace's equation.

Number	Representation	Mesh resolution	Δθ (°)
1	Full-Mesh (Interpolation ofThe Rigorous solution of Laplace's Eqn)	4.17e–02	11.0
2		1.67e–02	5.36
3		8.33e–03	3.62
4		4.17e–03	1.13
5		1.67e–03	0.182
6		8.33e–04	0.0874

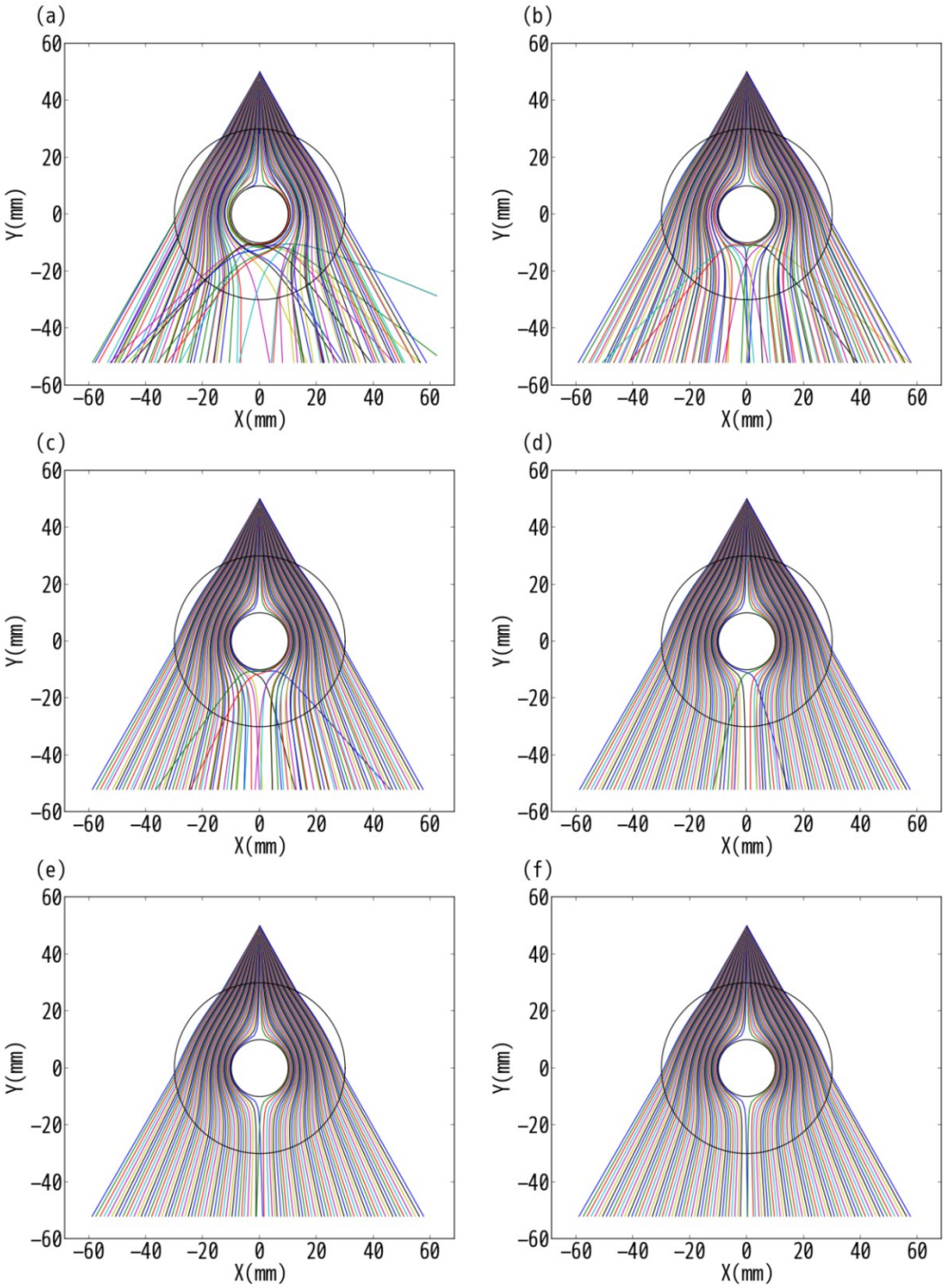

Fig. 4-13. The ray trajectories with the cylindrical cloaking device for the full-mesh representation with the interpolation of the rigorous solution of the Laplace's equation. The relative full-mesh resolutions are (a) 4.17e–02, (b) 1.67e–02, (c) 8.33e–03, (d) 4.17e–03, (e) 1.67e–03, and (f) 8.33e–04.

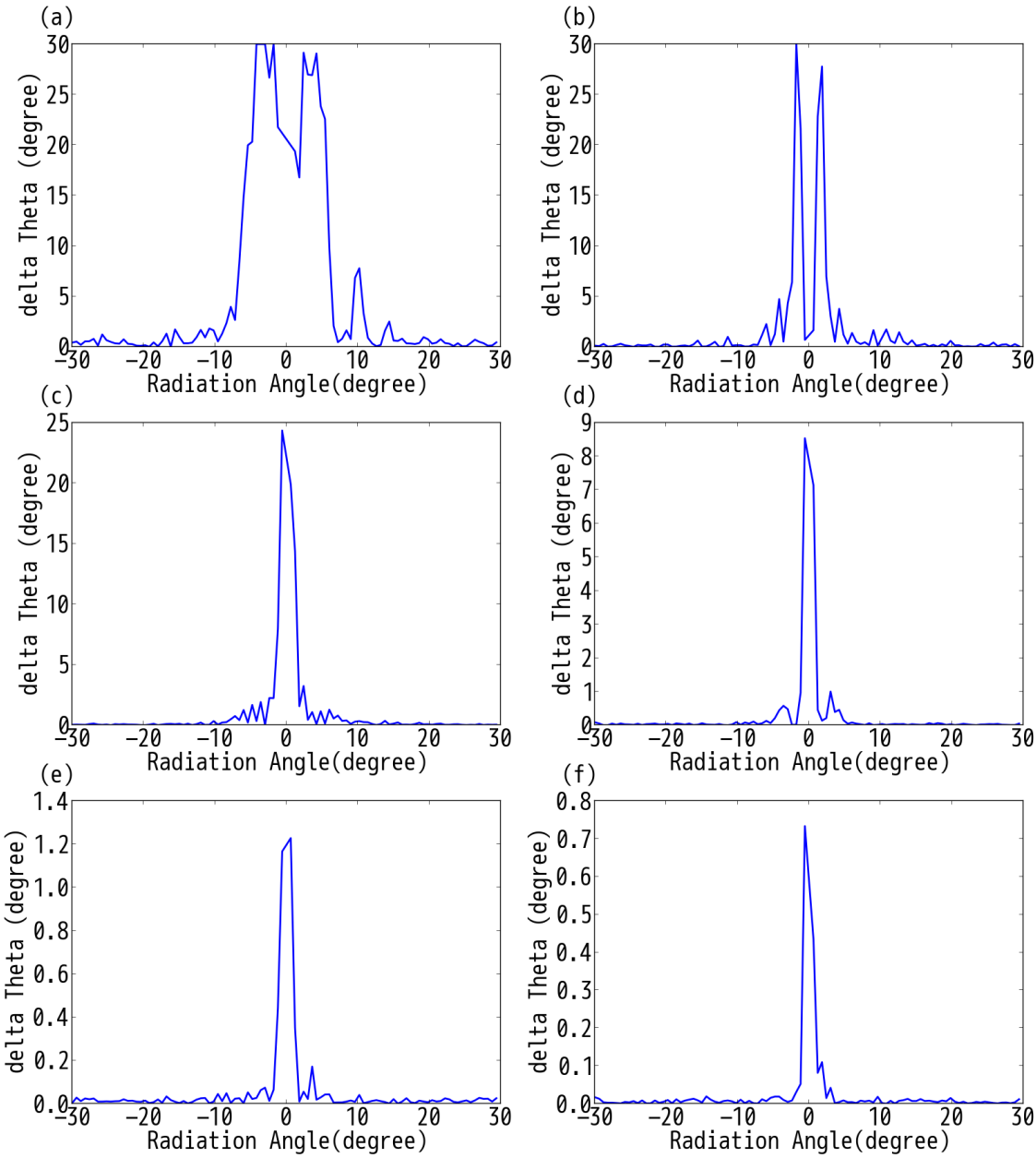

Fig. 4-14. The dependence of the cloaking performance on the radiation angle for the full-mesh representation with the interpolation of the rigorous solution of the Laplace's equation. The relative full-mesh resolutions are (a) 4.17e–02, (b) 1.67e–02, (c) 8.33e–03, (d) 4.17e–03, (e) 1.67e–03, and (f) 8.33e–04.

Here, let us consider the reason why the rays in the small radiation angles have large error with the low accuracy of the interpolation. The profiles of the rigorous solution of ε_ϕ and the linear interpolation of the rigorous solution of ε_ϕ are depicted in Fig. 4-15. The interpolation can approximate the rigorous solution except for the area near the inner boundary because the variation of ε_ϕ is gradual. On the other hand, near the inner boundary, the variation of ε_ϕ is very steep since the values on the inner boundary are infinity. Therefore, the difference between the interpolation and the rigorous solution becomes very large with the interpolation with a low accuracy as shown in Fig 4-15 (a). When a ray enters into an element with the inner boundary where the difference is large, the ray trajectory cannot be calculated accurately as shown in Fig. 4-16. That is why the rays in the small radiation angles, which can approach the inner boundary sufficiently, cause large error. As the accuracy of the interpolation is improved by using fine full-mesh, the area near the inner boundary with large error can be reduced as shown in Fig. 4-15 (b), leading to the decline of the number of the largely deviated rays.

By comparing Fig. 4-13 with Fig. 4-9, or Fig. 4-14 with Fig. 4-10, it is found that the ray trajectories from the rigorous solution are similar to those from the FEM-based solution. In addition, the cloaking performance for ε and μ represented by linear interpolations of the rigorous solution are compared with that for ε and μ represented by linear interpolations of the FEM solution in Fig 4-17. Figure 4-17 shows the very small difference between the cloaking performances at a certain full-mesh resolution, which suggests that the FEM solution is close to the rigorous solution. Therefore, the accuracy of the FEM is sufficiently high with six relative full-mesh resolutions. In other word, the effect of the accuracy of the interpolation is very large.

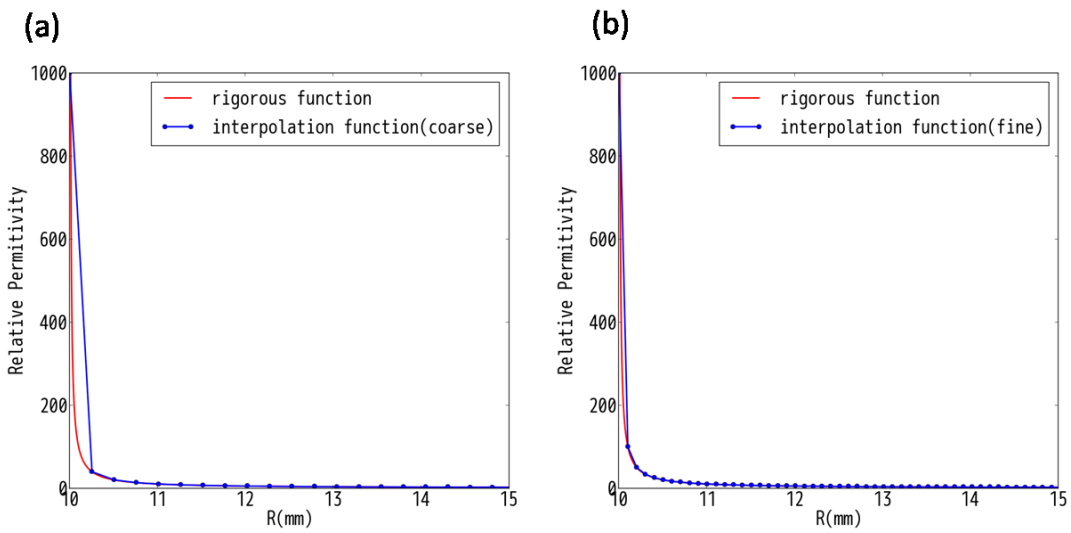

Fig. 4-15. The profiles of the rigorous solution of ε_ϕ and the linear interpolation of the rigorous solution of ε_ϕ: (a) the interpolation with the coarse mesh, (b) the interpolation with the fine mesh.

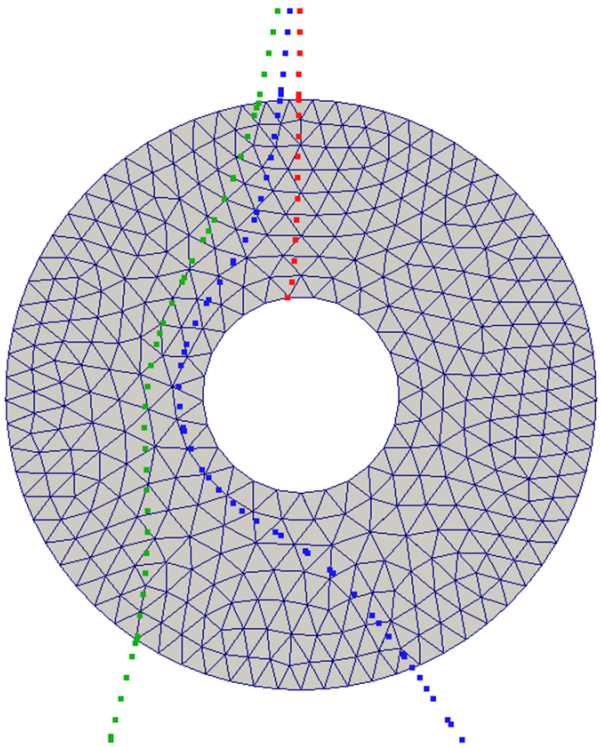

Fig. 4-16. The three ray trajectories passing near the inner boundary.

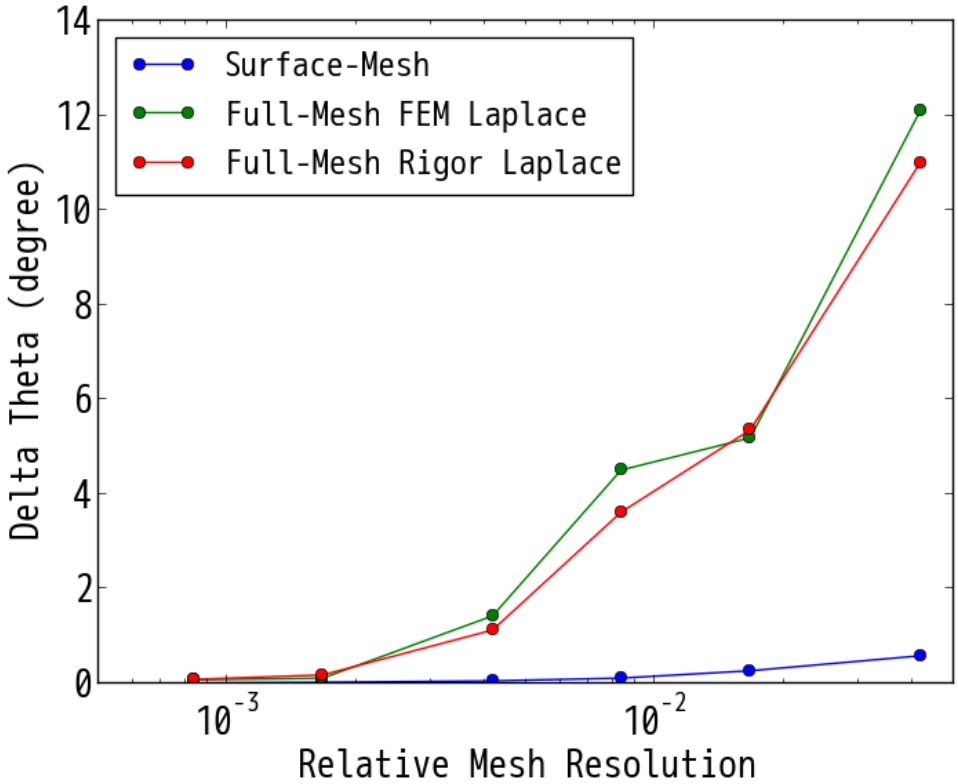

Fig. 4-17. The relationship between mesh resolution and cloaking performance for the surface-mesh representation, the full-mesh representation with the FEM-based solution of the Laplace's equation, and the full-mesh representation with the rigorous solution of the Laplace's equation.

4.3.4. Analysis of double cylindrical cloaking device

A double cylindrical cloaking device shown in Fig. 4-18 is analyzed as an example of cloaking devices with arbitrary shapes. Based on the results obtained in 4.3.2., the relative full-mesh resolution of 1.67e–03 is employed.

Shown in Fig. 4-19 (a) are the calculated ray trajectories. The performance calculated from the ray trajectories is $\Delta\theta = 0.215°$. The value of $\Delta\theta$ suggests that the performance of the double cylindrical cloaking device is comparable to the cylindrical cloaking device. Shown in Fig. 4-20 (a) is the dependence of the cloaking performance on the radiation

angle. From Fig. 4-20 (a), it is found that performances around the radiation angle of 0°, which correspond to the ray trajectories passing near the inner boundary, are degraded significantly as well as the cylindrical cloaking device. Additionally, it is noticed that performances around the radiation angle of −18° are degraded. The radiation angle corresponds to the ray trajectory passing near one of the two points where the two cylinders are connected. These points are considered to show singularity in the solution of the FEM, leading to the steep variation of ε and μ near the points. Because the linear interpolation of the solution of the FEM cannot approximate the steep variation correctly, the ray trajectories passing near the points cannot be calculated accurately. This is the same issue as the low accuracy of the interpolation described in 4.3.2.

The degradation of the cloaking performance due to the singularity is expected to be reduced by refinement of mesh resolution because the accuracy of the linear interpolation is improved by employing finer mesh resolution. Here, the double cylindrical cloaking device with a finer relative full-mesh resolution of 8.33e−04 is analyzed in order to elucidate whether the degradation can be reduced by refinement of mesh resolution. The calculated ray trajectories are depicted in Fig. 4-19 (b). The performance calculated from the ray trajectories is $\Delta\theta = 0.125°$. Hence, $\Delta\theta$ declines from 0.215° to 0.125° by refinement of mesh resolution, which suggests the degradation of the cloaking performance is reduced by refinement of mesh resolution. The dependence of the cloaking performance on the radiation angle is shown in Fig. 4-20 (b). From Fig. 4-20 (b), it is found that performances around the radiation angle of 0° and −18° are improved by refining mesh resolution, resulting in the decline of $\Delta\theta$.

Therefore, it is considered to be possible to reduce the degradation of cloaking performance due to the singularity in the solution of the FEM by refining mesh resolution.

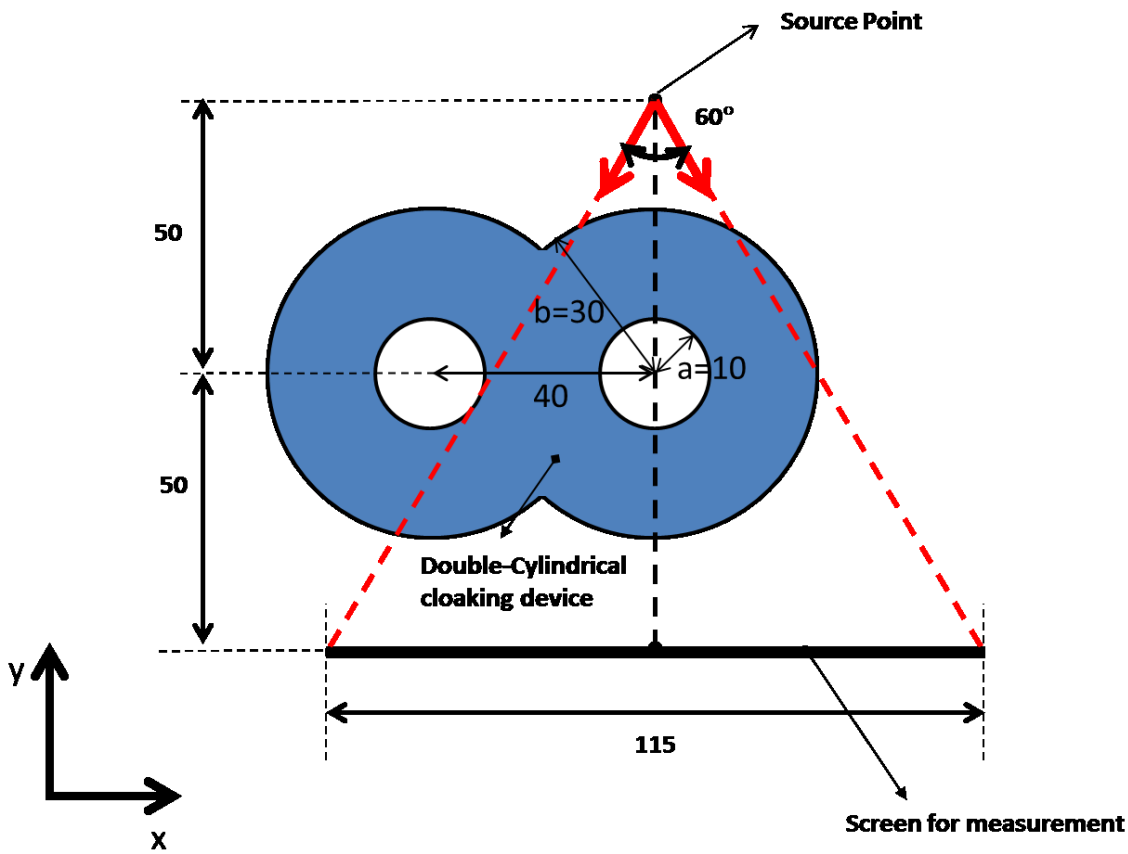

Fig. 4-18. Calculation model for the double-cylindrical cloaking device.

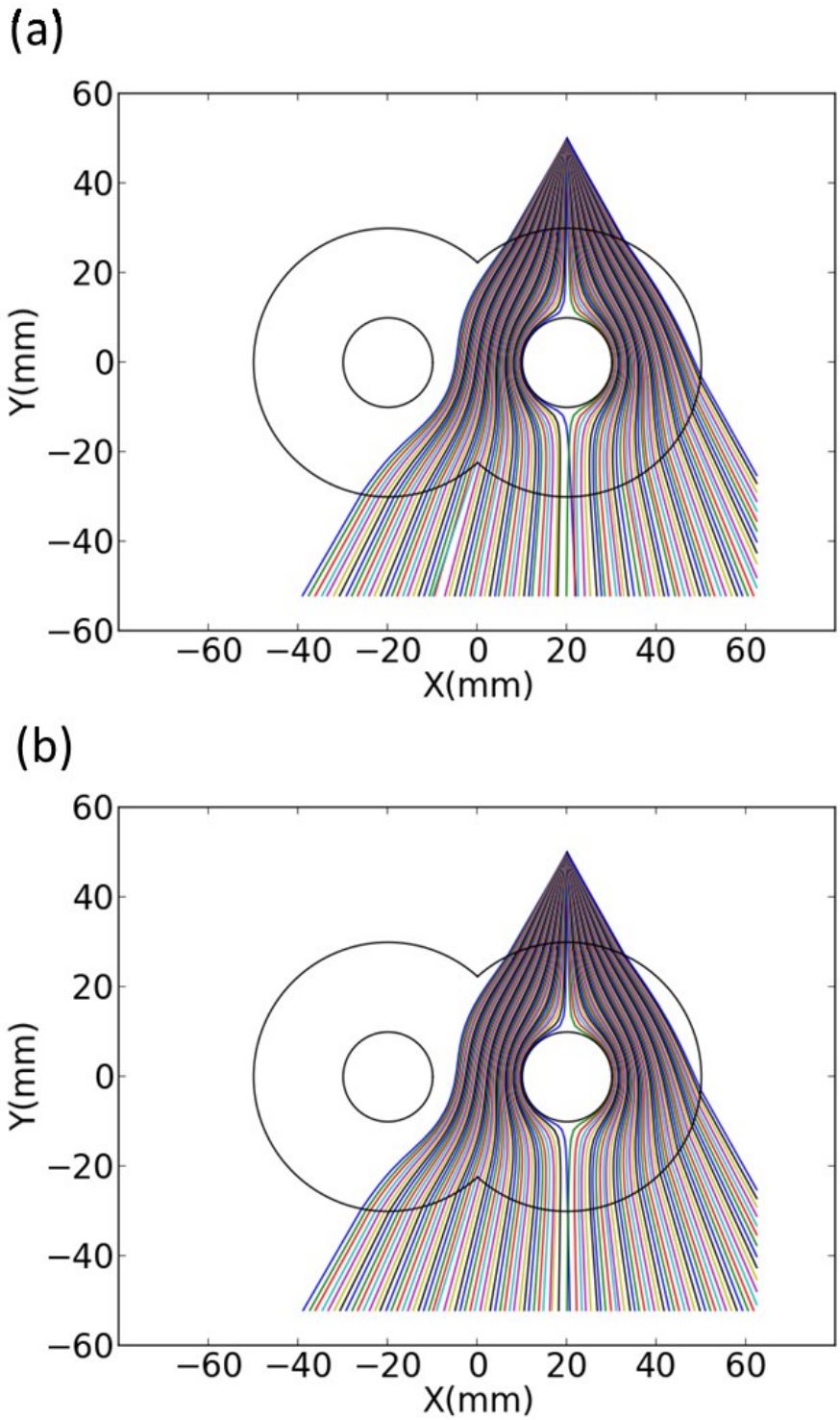

Fig. 4-19. The ray trajectories with the double-cylindrical cloaking device. The relative full-mesh resolutions are (a) 1.67e−03 and (b) 8.33e−04.

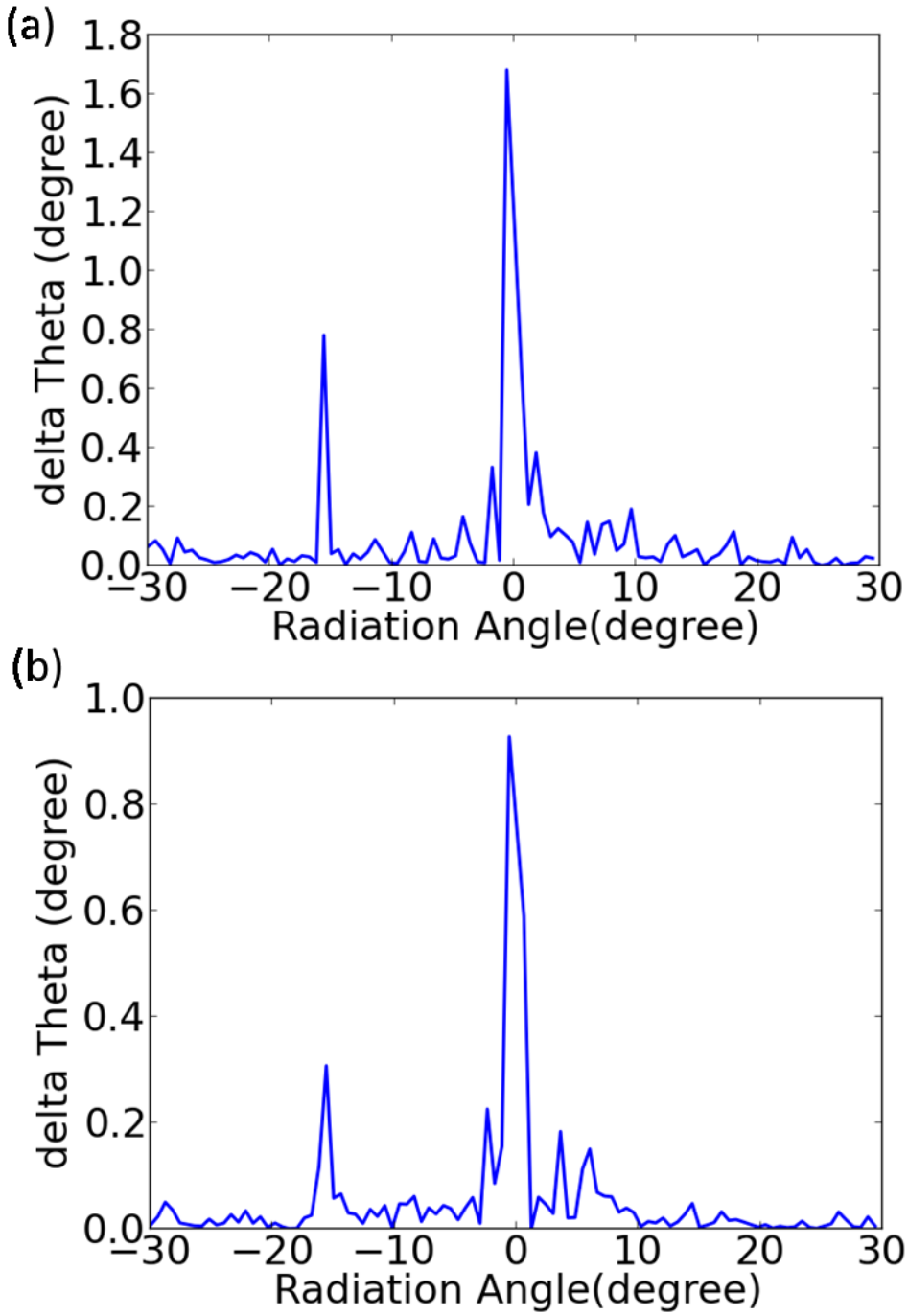

Fig. 4-20. The dependence of the double-cloaking performance on the radiation angle. The relative full-mesh resolutions are (a) 1.67e−03 and (b) 8.33e−04.

4.3.5. Analysis of huge arbitrary cloaking device

As the other example of cloaking devices with arbitrary shapes, a huge cloaking device with the completely arbitrary shape as shown in Fig. 4-20 [1], whose size is approximately 6 m, is analyzed. The relative full-mesh resolution of 1.67e–03 is employed as well as the double cylindrical cloaking device described in 4.3.3. The representative length for determining the relative full-mesh resolution is determined to be 6 m from the size of the cloaking device. Therefore, the actual full-mesh resolution corresponds to 0.01 m.

The calculated ray trajectories are shown in Fig. 4-22 (a). The performance calculated from the ray trajectories is $\Delta\theta = 2.54°$, which suggests that the performance for the cloaking device is not higher than that for the cylindrical cloaking device. The dependence of the cloaking performance on the radiation angle is shown in Fig. 4-23 (a). It is found that the performance is degraded at the radiation angle close to 0.0°. The reason for the degradation of the performance is considered to be the low accuracy of the interpolation described in 4.3.2.

Since the accuracy of the interpolation can be improved by refining the full-mesh resolution, ray trajectories is calculated with a finer relative full-mesh resolution of 8.33e–04. Shown in Fig. 4-22 (b) are the calculated ray trajectories. By comparing Fig. 4-22 (b) with Fig. 4-22 (a), it is found that the error of the ray trajectories becomes smaller at the relative full-mesh resolution of 8.33e–04 than at that of 1.67e–03. The performance calculated from the ray trajectories is $\Delta\theta = 0.343°$ that is smaller than that at the full-mesh resolution of 1.67e–03.

The dependence of the cloaking performance on the radiation angle is shown in Fig. 4-23 (b). By comparing Fig. 4-23 (b) with Fig. 4-23 (a), it is found that performances

around a radiation angle of 0.0° are improved significantly by refining the full-mesh resolution.

From the above results, it can be seen that a finer full-mesh resolution is required for high performance of cloaking devices with general shapes than with regular shapes like a cylinder. The reason why a fine full-mesh resolution is required for cloaking devices with general shapes is considered as follows. A cloaking device with an inner boundary as shown in Fig. 4-21, shows steeper variation of ε and μ near the inner boundary than a cylindrical cloaking device. Therefore, in order to approximate the variation of ε and μ in the cloaking device by linear interpolation, finer full-mesh resolution is required than a cylindrical cloaking device.

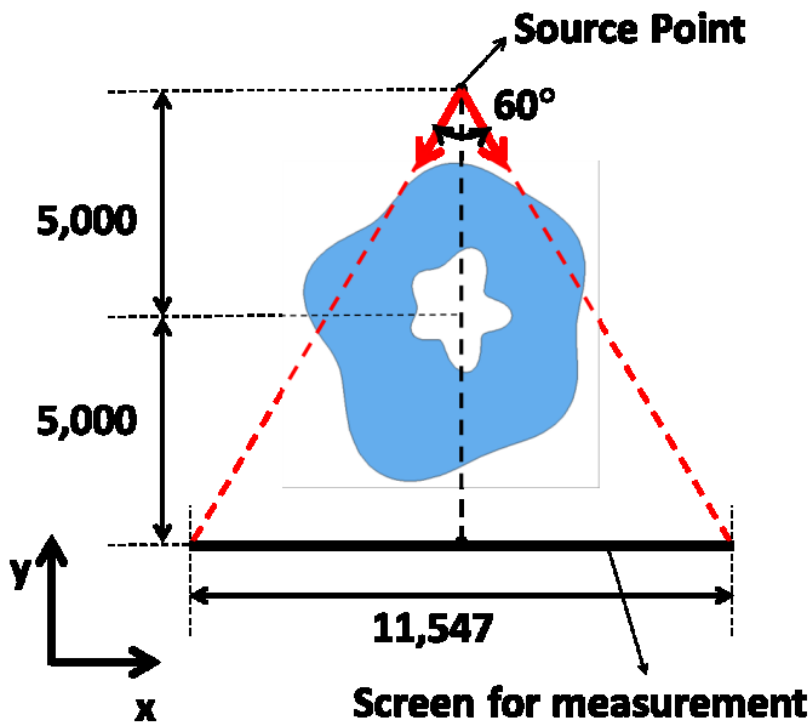

Fig. 4-21. Calculation model for the huge arbitrary cloaking device.

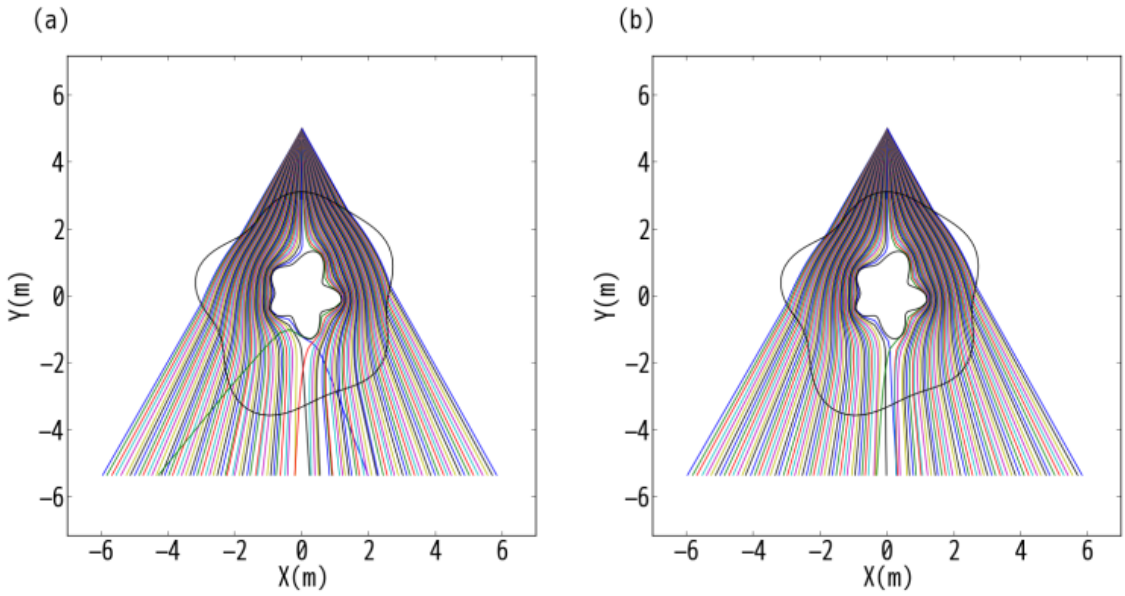

Fig. 4-22. The ray trajectories with the huge arbitrary cloaking device. The relative full-mesh resolutions are (a) 1.67e–03 and (b) 8.33e–04.

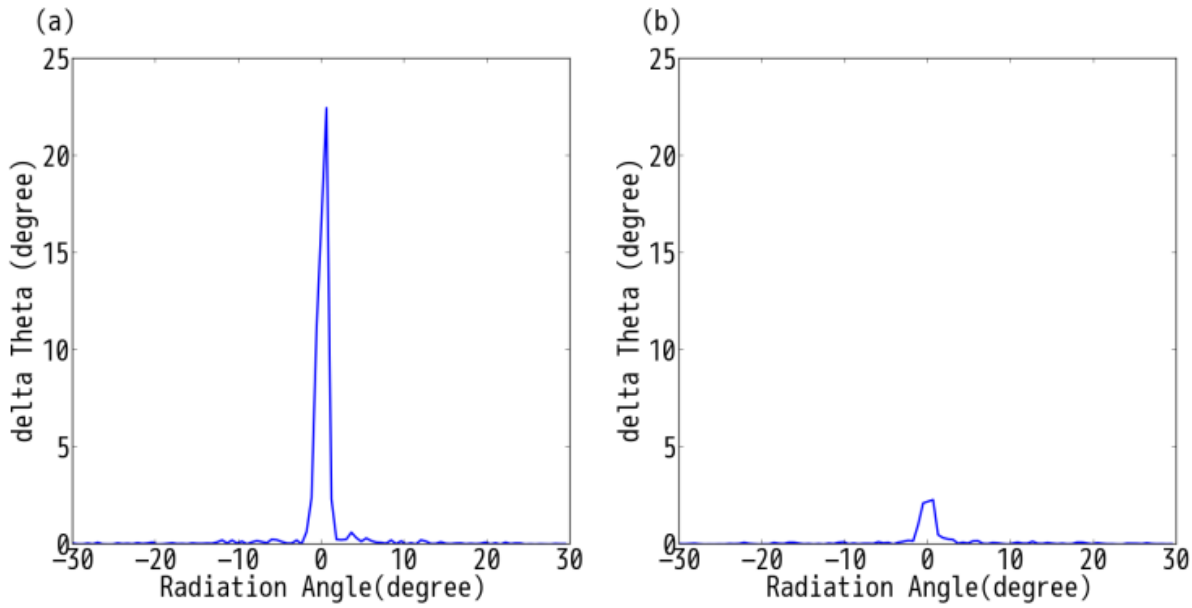

Fig. 4-23. The dependence of the cloaking performance of the huge arbitrary cloaking device on the radiation angle. The relative full-mesh resolutions are (a) 1.67e–03 and (b) 8.33e–04.

4.3.6. Computational memory and speed

Here, the computational memory and the computational speed is estimated for the proposed Hamiltonian-based ray tracing. In the case of the huge cloaking device with the completely arbitrary shape with the full-mesh resolution of 8.33e–04, less than 2.5 GB of memory is required for the proposed Hamiltonian-based ray tracing. If the same model is calculated by full-wave simulation, more than 300 PB of memory is estimated to be required. The usage of such a huge amount of memory is beyond the capacities of current supercomputers. Therefore, in terms of memory usages, the proposed Hamiltonian-based ray tracing is efficient for large-scale objects.

In terms of computational speed, it takes approximately 5 hours to obtain ray trajectories by using 5 CPU cores (Intel Xeon E5-2687W 3.1GHz). This calculation speed is much faster than full-wave simulation. If more CPU cores are available in the parallel computation, the computational speed can be faster in proportion to the number of CPU cores, leading to sufficient computational speed for the design of large-scale cloaking devices.

4.3.7. Feasibility of fabrication of cloaking devices

From 4.3.2, 4.3.4, and 4.3.5, a relative mesh resolution finer than 1.67e–03 is found to be required for high performance for cloaking devices with regular shapes like a cylinder, whereas a relative full-mesh resolution finer than 8.33e–04 is found to be required for cloaking devices with general shapes. The relative mesh resolution of 1.67e–3 corresponds to the mesh resolution of 0.1 mm for the cylindrical cloaking device with the diameter of 60 mm. This suggests that a resolution for the fabrication

finer than 0.1 mm is required at least. Here, let us consider the feasibility of the fabrication of the cloaking device which is divided with a resolution of 0.1 mm by assuming that a unit structure of metamaterial which yields the constitutive parameter at each region can be found.

Two approaches can be considered for assignment of the constitutive parameter by using metamaterial at each region. A first approach is that each region is represented by one unit structure of the metamaterial as shown in Fig. 4-24 (a). Therefore, since the size of each region is the same as that of the unit structure of the metamaterial, one unit structure of the metamaterial is assigned to each region with a size of 0.1 mm. By employing this approach, cloaking devices have been realized at microwave wavelengths [13, 15]. Furthermore, cloaking devices based on carpet cloaking, which is another type of cloaking, have been validated in the wavelength range of visible light [40-43].

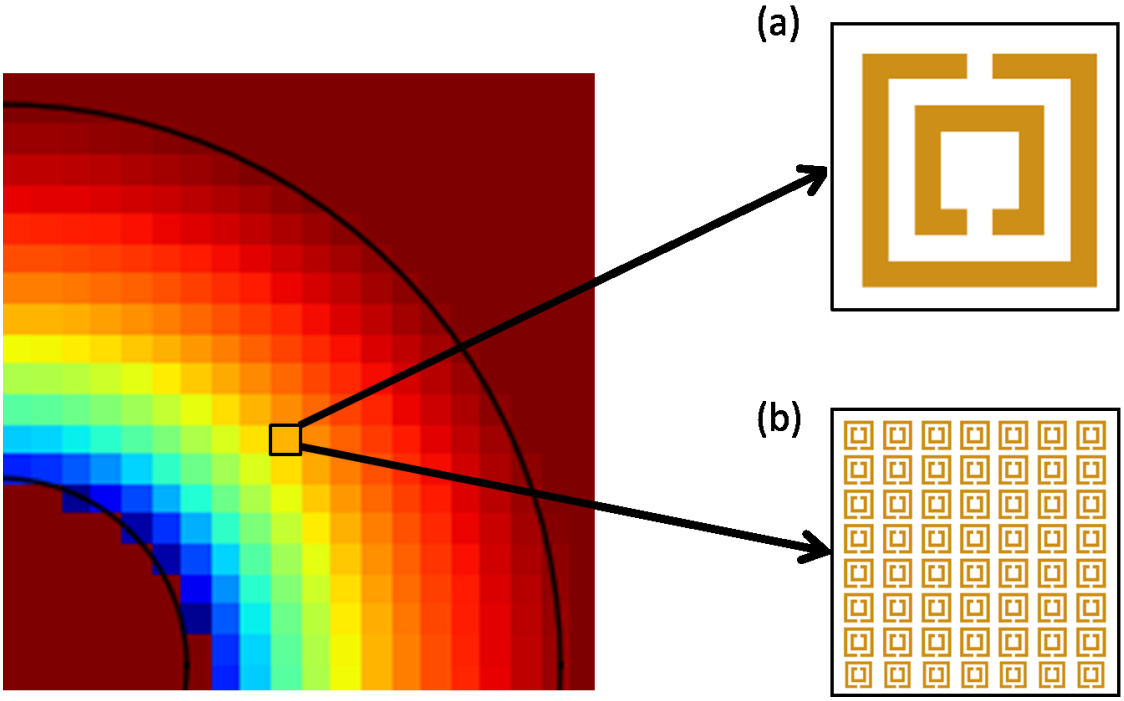

Fig. 4-24. Two approaches for assignment of the constitutive parameter by using metamaterial at each region. (a) Each region is represented by one unit structure of the metamaterial. (b) Each region is represented by the array of unit structure of the metamaterial.

Here, the relation between the operation wavelength (λ) and the size of the unit structure of each of metamaterials which have been fabricated is shown in Table 4-4 [13-48]. The relation is plotted in Fig. 4-25. As λ becomes shorter, the size of the unit structure is found to become smaller. It is also seen that most of the sizes of the unit structures are smaller than λ. This indicates that the size of the unit structure of a metamaterial is required to be smaller than λ in order for the metamaterial to behave as an effective medium [13]. In the wavelength range of visible light, the size of the unit structure needs to be less than 400 nm - 800 nm. Therefore, one unit structure cannot be assigned to the region with a size of 0.1 mm in the wavelength range of visible light.

The other approach is that each region is represented by the array of a unit structure

of the metamaterial as shown in Fig. 4-24 (b), which suggests that the size of the region can be larger than that of the unit structure. By using a unit structure with a size smaller than λ, the metamaterial behaves as an effective medium. From Fig. 4-25, at the wavelengths longer than 1e–05 m (10 μm), the sizes of the unit structures are found to close to λ/10, whereas at the wavelengths shorter than 1e–05 m (10 μm), most of the sizes of the unit structures are found to range from λ/10 to λ. This indicates that for long λ, the sizes of the unit structures can be sufficiently small compared with λ, whereas for short λ, fabricating a metamaterial with a sufficiently small unit structure compared with λ is difficult.

In Table 4-4, the relation between the size of the unit structure of each of metamaterials which have been fabricated and the year when each study was published is also shown. The relation is plotted in Fig. 4-26. It is found that the size of the unit structure can be reduced from the order of 1e–03 m to the order of 1e–06 m in 2005. The reduction of the size of the unit structure was due to the utilization of electron-beam lithography, which enables a fabrication with a resolution finer than the wavelength of visible light.

Table 4-4: The relation between the wavelength and the size of the unit structure of metamaterial.

Frequency (GHz)	Wavelength (m)	Size of unit structure (m)	Year	Ref.
5.00e+00	6.00e–02	8.00e–03	2000	[13]
5.45e+00	5.50e–02	4.00e–03	2013	[14]
8.50e+00	3.53e–02	3.18e–03	2006	[15]
1.00e+01	3.00e–02	5.00e–03	2001	[16]
1.00e+01	3.00e–02	5.00e–03	2002	[17]
1.30e+01	2.31e–02	3.30e–03	2003	[18]
5.00e+02	6.00e–04	1.70e–04	2010	[19]

1.00e+03	3.00e−04	4.30e−05	2004	[20]
6.00e+03	5.00e−05	7.00e−06	2005	[21]
6.00e+04	5.00e−06	6.00e−07	2005	[22]
1.00e+05	3.00e−06	6.75e−07	2004	[23]
1.50e+05	2.00e−06	8.38e−07	2005	[24]
1.50e+05	2.00e−06	7.00e−07	2008	[25]
1.54e+05	1.95e−06	8.50e−07	2011	[26]
1.76e+05	1.70e−06	6.00e−07	2007	[27]
2.00e+05	1.50e−06	3.00e−07	2005	[28]
2.00e+05	1.50e−06	1.80e−06	2005	[29]
2.00e+05	1.50e−06	6.00e−07	2006	[30]
2.00e+05	1.50e−06	6.00e−07	2006	[31]
2.00e+05	1.50e−06	8.00e−07	2015	[32]
2.00e+05	1.50e−06	8.00e−07	2010	[33]
2.00e+05	1.50e−06	6.50e−07	2010	[34]
2.13e+05	1.41e−06	6.45e−07	2007	[35]
2.14e+05	1.40e−06	4.00e−07	2011	[36]
3.00e+05	1.00e−06	1.00e−06	2005	[37]
3.33e+05	9.00e−07	2.40e−07	2006	[38]
3.85e+05	7.80e−07	3.00e−07	2007	[39]
3.89e+05	7.72e−07	3.00e−07	2007	[40]
3.90e+05	7.70e−07	3.65e−07	2013	[41]
4.29e+05	7.00e−07	3.50e−07	2011	[42]
4.48e+05	6.70e−07	3.50e−07	2011	[43]
4.55e+05	6.60e−07	1.10e−07	2008	[44]
5.00e+05	6.00e−07	3.00e−07	2014	[45]
5.00e+05	6.00e−07	4.00e−07	2005	[46]
5.00e+05	6.00e−07	1.30e−07	2011	[47]
5.17e+05	5.80e−07	2.20e−07	2009	[48]

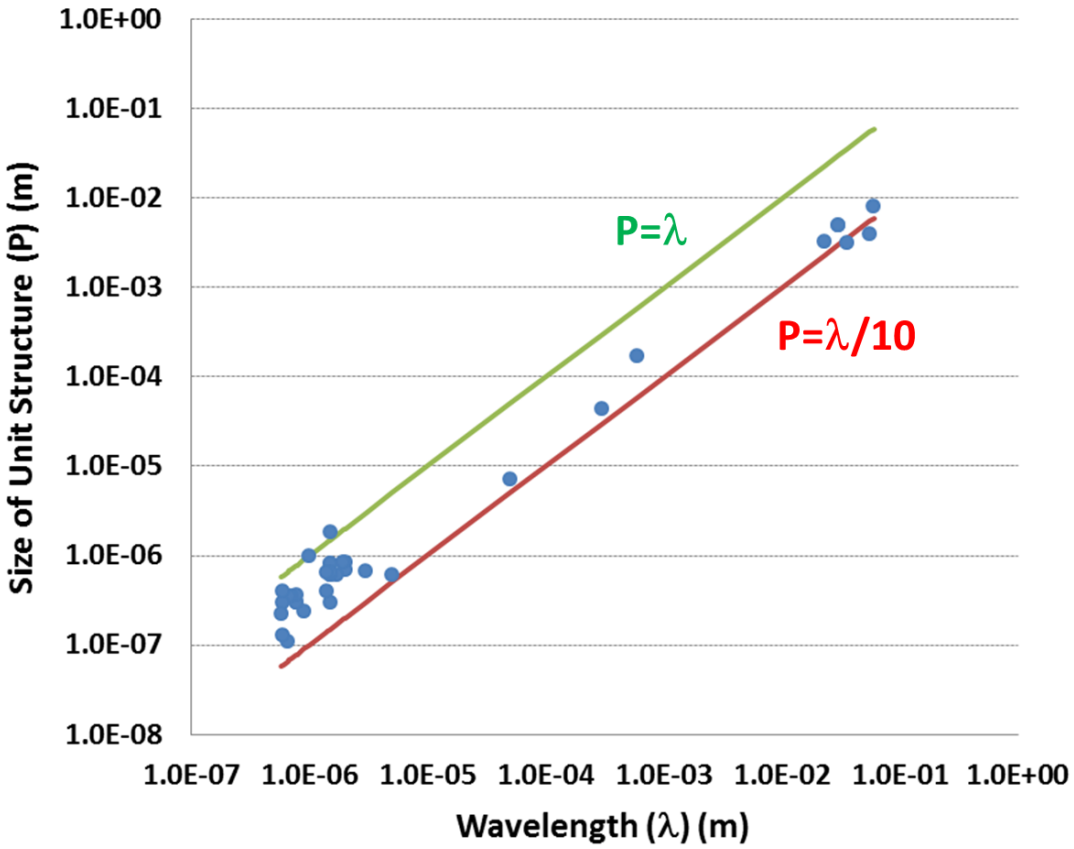

Fig. 4-25. The relation between the wavelength and the size of the unit structure of metamaterial.

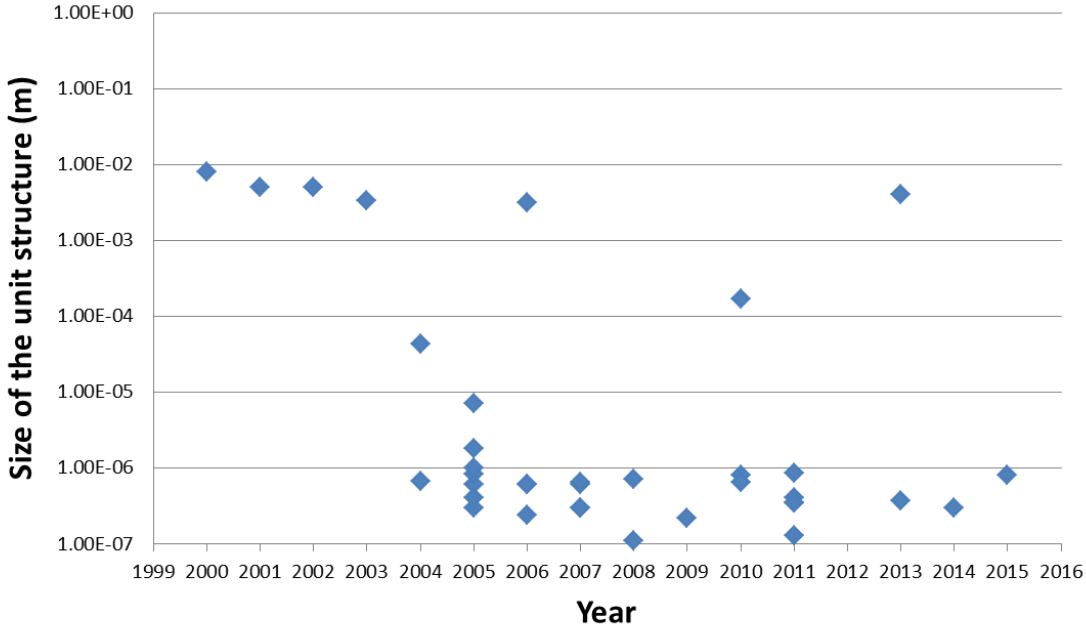

Fig. 4-26. The relation between the size of the unit structure of each of metamaterials which have been fabricated and the year when each study was published.

On the other hand, it is necessary to discuss the feasibility that a metamaterial with such a large size as 0.1 mm can be fabricated by repeating a unit structure with a size smaller than 400 nm - 800 nm. Recently, large-area metamaterials have been fabricated by using standard electron-beam lithography (EBL) [23, 25, 28-31, 37-39], deep UV (DUV) lithography [34], interferometric lithography [24], direct laser writing (DLW) [33, 42] and nanoimprint lithography (NIL) [26, 27, 36, 41, 45]. Table 4-5 shows the summary of the size of the total dimension fabricated by using these technologies. Many studies have used standard EBL since it can very easily lead to devices with feature sizes on the order of a few tens of nanometers. Table 4-5 indicates that EBL can fabricate the metamaterial with a large area of 0.1mm^2. However, large-area fabrication can be prohibitively expensive and time consuming. DLW, which has an advantage in fabrication of three-dimensional metamaterial, can also realize the metamaterial with a large area of several tens μm. Nevertheless it suffers from low throughput as well as

EBL. On the other hand, DUV lithography, interferometric lithography, and NIL can fabricate metamaterial with high throughput. DUV lithography is compatible to the current fabrication process of semiconductor, potentially leading to the mass fabrication. From Table 4-5, NIL has the highest potential to yield large metamaterial.

Therefore, although any of standard EBL, DUV lithography, interferometric lithography, DLW or NIL is considered to have the ability to fabricate metamaterial with a size of 0.1 mm (100 μm), either of DUV lithography, interferometric lithography or NIL is preferred for the fabrication method in terms of throughput.

Table 4-5: Total dimension of metamaterial fabricated by various methods.

Frequency (THz)	Wavelength (nm)	Size of unit structure (nm)	Total dimension (mm)	Method	Year	Ref.
100	3000	675	0.025	EBL	2004	[23]
150	2000	838	10	Interferometric lithography	2005	[24]
150	2000	700	0.2	EBL	2008	[25]
154	1950	850	87	NIL	2011	[26]
176	1700	600	0.5	NIL	2007	[27]
200	1500	300	0.1	EBL	2005	[28]
200	1500	1800	2	EBL	2005	[29]
200	1500	600	0.1	EBL	2006	[30]
200	1500	600	0.1	EBL	2006	[31]
200	1500	800	0.03	DLW	2010	[33]
200	1500	650	2	DUV lithography	2010	[34]
214	1400	400	9	NIL	2011	[36]
300	1000	1000	0.08	EBL	2005	[37]
333	900	240	0.02	EBL	2006	[38]
385	780	300	0.1	EBL	2007	[39]
390	770	365	10	NIL	2013	[41]
429	700	350	0.05	DLW	2011	[42]
500	600	300	25	NIL	2014	[45]

4.4. Conclusion

The Hamiltonian-based ray tracing method integrating the numerical modeling of the constitutive parameters based on the FEM by adapting the full-mesh representation for dealing with large-scale cloaking devices with arbitrary shapes has been proposed. The full-mesh representation has been evaluated by comparing the rigorous function representation and the surface-mesh representation with respect to the performance of cylindrical cloaking to show the effectiveness of the proposed method.

Subsequently, the proposed Hamiltonian-based ray tracing with the full-mesh representation has been applied to the evaluation of the two examples of cloaking devices with arbitrary shapes, the double cylindrical cloaking device and the huge arbitrary cloaking device. The numerical results of these cloaking devices have shown high performance. Therefore, the proposed Hamiltonian ray tracing with the full-mesh representation can be applied to the evaluation of the performance of cloaking devices with arbitrary shapes.

From the obtained results, a general guideline for the full-mesh resolution can be proposed as follows. A relative full-mesh resolution finer than 1.67e−03 is required for high performance for cloaking devices with regular shapes like a cylinder, whereas a relative full-mesh resolution finer than 8.33e−04 is required for cloaking devices with general shapes.

The full-mesh representation also has an advantage in terms of the fabrication of cloaking devices. Since the continuous distributions of the constitutive parameters obtained from transformation optics rigorously cannot be realized by the current fabrication technology, the continuous distributions of the constitutive parameters have to be discretized with certain resolution depending on the technology used for the

fabrication of cloaking devices. On the other hand, since the resolution of the full-mesh representation corresponds to that for the fabrication, cloaking devices can be designed taking the resolution for the fabrication into account. Therefore, the full-mesh representation is useful to fabricate actual devices.

References

1. D. Schurig, J. B. Pendry, and D. R. Smith, "Calculation of material properties and ray tracing in transformation media," Opt. Express **14**, 9794–9804 (2006).
2. J.C. Halimeh, and M. Wegener, "Photorealistic rendering of unidirectional free-space invisibility cloaks," Opt. Express **21**, 9457–9472 (2013).
3. J. C. Halimeh and M. Wegener, "Time-of-flight imaging of invisibility cloaks," Opt. Express **20**, 63–74 (2012).
4. J. C. Halimeh, R. Schmied, and M. Wegener, "Newtonian photorealistic ray tracing of grating cloaks and correlation-function-based cloaking-quality assessment," Opt. Express **19**, 6078–6092 (2011).
5. J. C. Halimeh, and M. Wegener, "Photorealistic ray tracing of free-space invisibility cloaks made of uniaxial dielectrics," Opt. Express **20**, 28330–28340 (2012).
6. G. Dolling, M. Wegener, S. Linden, and C. Hormann, "Photorealistic images of objects in effective negative-index materials," Opt. Express **14**, 1842–1849 (2006).
7. J. C. Halimeh, R. T. Thompson, and M. Wegener, "Invisibility cloaks in relativistic motion," Phys. Rev. A 93, 013850 (2016).
8. J. C. Halimeh, and R. T. Thompson, "Fresnel-Fizeau drag: Invisibility conditions for all inertial observers," arXiv:1601.04218.
9. A. J. Danner, "Visualizing invisibility: Metamaterials-based optical devices in natural environments," Opt. Express **18**, 3332–3337 (2010).
10. Y. Jiao, S. Fan, and D. A. B. Miller, "Designing for beam propagation in periodic and nonperiodic photonic nanostructures: Extended Hamiltonian method," Phys. Rev. E 70, 036612 (2004).
11. A. Alireza, and A. J. Danner, "Generalization of ray tracing in a linear inhomogeneous anisotropic medium: a coordinate-free approach," J. Opt. Soc. Am.

A **27**, 2558–2562 (2010).

12. J. Hu, X. Zhou and G. Hu, "Design method for electromagnetic cloak with arbitrary shapes based on Laplace's equation," Opt. Express **17**, 1308-1320 (2009).
13. D. R. Smith, W. J. Padilla, D. C. Vier, S. C. Nemat-Nasser, and S. Schultz, "Composite Medium with Simultaneously Negative Permeability and Permittivity," Phys. Rev. Lett., **84**, 4184-4187 (2000).
14. Y. Ma, Y. Liu, L. Lan, T. Wu, W. Jiang, C. K. Ong, and S. He, "First experimental demonstration of an isotropic electromagnetic cloak with strict conformal mapping," Scientific Reports, **3**, 2182 (2013).
15. D. Schurig, J. J. Mock, B. J. Justice, S. A. Cummer, J. B. Pendry, A. F. Starr, and D. R. Smith, "Metamaterial electromagnetic cloak at microwave frequencies," Science, **314**, 977-980 (2006).
16. R. A. Shelby, D. R. Smith, and S. Schultz, "Experimental Verification of a Negative Index of Refraction," Science, **292**, 77-79 (2001).
17. M. Bayindir, K. Aydin, E. Ozbay, P. Markos, and C. M. Soukoulis, "Transmission properties of composite metamaterials in free space," Appl. Phys. Lett., **81**, 120-122 (2002).
18. R. B. Greegor, C. G. Parazzoli, K. Li, and M. H. Tanielian, "Origin of dissipative losses in negative index of refraction materials," Appl. Phys. Lett., **82**, 2356-2358 (2003).
19. F. Miyamaru, S. Kuboda, K. Taima, K. Takano, M. Hangyo, and M. W. Takeda, "Three-dimensional bulk metamaterials operating in the terahertz range," Appl. Phys. Lett., **96**, 081105 (2010).
20. T. J. Yen, W. J. Padilla, N. Fang, D. C. Vier, D. R. Smith, J. B. Pendry, D. N. Basov,

X. Zhang, “Terahertz Magnetic Response from Artificial Materials,” Science, **303**, 1494-1496 (2004).

21. N. Katsarakis, G. Konstantinidis, A. Kostopoulos, R. S. Penciu, T. F. Gundogdu, M. Kafesaki, and E. N. Economou, T. Koschny, and C. M. Soukoulis, “Magnetic response of split-ring resonators in the far infrared frequency regime,” Opt. Lett., **30**, 1348-1350 (2005).
22. S. Zhang, W. Fan, B. K. Minhas, A. Frauenglass, K. J. Malloy, and S. R. J. Brueck, “Mid-infrared resonant magnetic nanostructures exhibiting a negative permeability,” Phys. Rev. Lett., **94**, 037402 (2005).
23. S. Linden, C. Enkrich, M. Wegener, J. Zhou, T. Koschny, C. M. Soukoulis, “Magnetic response of metamaterials at 100 THz,” Science, 306, 1351-1353 (2004).
24. S. Zhang, W. Fan, N. C. Panoiu, K. J. Malloy, R. M. Osgood and S. R. J. Brueck, “Experimental demonstration of near-infrared negative-index metamaterials,” Phys. Rev. Lett., **95**, 137404 (2005).
25. N. Liu, H. Guo, L. Fu, S. Kaiser, H. Schweizer, and H. Giessen, “Three-dimensional photonic metamaterials at optical frequencies,” Nature Mater., **7**, 31-37, (2008).
26. D. Chanda, K. Shigeta, S. Gupta, T. Cain, A. Carlson, A. Mihi, A. J. Baca, G. R. Bogart, P. Braun and J. A. Rogers, “Large-area flexible 3D optical negative index metamaterial formed by nanotransfer printing,” Nature Nanotechnology, **6**, 402-407 (2011).
27. W. Wu, E. Kim, E. Ponizovskaya, Y. Liu, Z. Yu, N. Fang, Y. R. Shen, A. M. Bratkovsky, W. Tong, C. Sun, X. Zhang, S. Wang and R. S. Williams, ”Optical Metamaterials at Near and Mid IR Range Fabricated by Nanoimprint Lithography,”

Appl. Phys. A: Materials Science & Processing, **87**, 143-150 (2007).

28. C. Enkrich, M. Wegener, S. Linden, S. Burger, L. Zschiedrich, F. Schmidt, J. F. Zhou, T. Koschny, and C. M. Soukoulis, "Magnetic metamaterials at telecommunication and visible frequencies," Phys. Rev. Lett., **95**, 203901 (2005).
29. V. M. Shalaev, W. Cai, U. K. Chettiar, H. Yuan, A. K. Sarychev, V. P. Drachev, and A. V. Kildishev, "Negative index of refraction in optical metamaterials," Opt. Lett., **30**, 3356-3358 (2005).
30. G. Dolling, C. Enkrich, M. Wegener, C. M. Soukoulis, and S. Linden, "Simultaneous negative phase and group velocity of light in a metamaterial," Science, **312**, 892-894 (2006).
31. G. Dolling, C. Enkrich, M. Wegener, C. M. Soukoulis, and S. Linden, "Low-loss negative-index metamaterial at telecommunication wavelengths," Opt. Lett., **31**, 1800-1802 (2006).
32. M. F. Schumann, S. Wiesendanger, J. C. Goldschmidt, B. Blasi, K. Bittkau, U. W. Paetzold, A. Sprafke, R. B. Wehrspohn, C. Rockstuhl, and M. Wegener, "Cloaked contact grids on solar cells by coordinate transformations: designs and prototypes," Optica, **2**, 850-853 (2015).
33. T. Ergin, N. Stenger, P. Brenner, J. B. Pendry, and M. Wegener, "Three-Dimensional Invisibility Cloak at Optical Wavelengths," Science, **328**, 337-339 (2010).
34. N. Dutta, I. O. Mirza, S. Shi and D. W. Prather, "Fabrication of Large Area Fishnet Optical Metamaterial Structures Operational at Near-IR Wavelengths," Materials, **3**, 5283-5292 (2010).
35. G. Dolling, M. Wegener, and S. Linden, "Realization of a three-functional-layer negative-index photonic metamaterial," Opt. Lett., **32**, 551-553 (2007).

36. I. Bergmair, B. Dastmalchi, M. Bergmair, A. Saeed, W. Hilber, G. Hesser, C. Helgert, E. Pshenay-Severin, T. Pertsch, E. B. Kley, U. H¨ubner, N. H. Shen, R. Penciu, M. Kafesaki, C. M. Soukoulis, K. Hingerl, M. Muehlberger, and R. Schoeftner, "Single and multilayer metamaterials fabricated by nanoimprint lithography," Nanotechnology, **22**, 325301 (2011).
37. G. Dolling, C. Enkrich, M. Wegener, J. F. Zhou, and C. M. Soukoulis, S. Linden, "Cut-wire pairs and plate pairs as magnetic atoms for optical metamaterials," Opt. Lett., **30**, 3198-3200 (2005).
38. M. W. Klein, C. Enkrich, M. Wegener, C. M. Soukoulis, and S. Linden, "Single-slit split-ring resonators at optical frequencies: Limits of size scaling," Opt. Lett., **31**, 1259-1261 (2006).
39. G. Dolling, M. Wegener, C. M. Soukoulis, and S. Linden, "Negative-index metamaterial at 780 nm wavelength," Opt. Lett., **32**, 53-55 (2007).
40. U. K. Chettiar, A. V. Kildishev, H. Yuan, W. Cai, S. Xiao, V. P. Drachev, and V. M. Shalaev, "Dual-band negative index metamaterial: Double negative at 813 nm and single negative at 772 nm," Opt. Lett., **32**, 1671-1673 (2007).
41. T. W. H. Oates, B. Dastmalchi, C. Helgert, L. Reissmann, U. Huebner, E. Kley, M. A. Verschuuren, I. Bergmair, T. Pertsch, K. Hingerl, and K. Hinrichs, "Optical activity in sub-wavelength metallic grids and fishnet metamaterials in the conical mount," Opt. Mat. Express, **3**, 439-451 (2013).
42. J. Fischer, T. Ergin, and M. Wegener, "Three-dimensional polarization-independent visible-frequency carpet invisibility cloak," Opt. Lett., **36**, 2059-2061 (2011).
43. C. García−Meca, J. Hurtado, J. Martí, A. Martínez, W. Dickson, and A. V. Zayats, "Low-loss multilayered metamaterial exhibiting a negative index of visible of

refraction at visible wavelengths," Phys. Rev. Lett., **106**, 067402 (2011).

44. J. Yao, Z. Liu, Y. Liu, Y. Wang, C. Sun, G. Bartal, A. M. Stacy, X. Zhang, "Optical negative refraction in bulk metamaterials of nanowires," Science, **321**, 930 (2008).
45. L. Gao, K. Shigeta, A. Vazquez-Guardado, C. J. Progler, G. R. Bogart, J. A. Rogers, and D. Chanda, "Nanoimprinting Techniques for Large-Area Three-Dimensional Negative Index Metamaterials with Operation in the Visible and Telecom Bands," ACS nano, **8**, 5535-5542 (2014).
46. A. N. Grigorenko, A. K. Geim, H. F. Gleeson, Y. Zhang, A. A. Firsov, I. Y. Khrushchev and J. Petrovic, "Nanofabricated media with negative permeability at visible frequencies," Nature, **438**, 335-338 (2005).
47. M. Gharghi, C. Gladden, T. Zentgraf, Y. Liu, X. Yin, J. Valentine and X. Zhang, "A Carpet Cloak for Visible Light," Nano Lett., **11**, 2825–2828 (2011).
48. S. M. Xiao, U. K. Chettiar, A. V. Kildishev, V. P. Drachev, and V. M. Shalaev, "Yellow-light negativeindex metamaterials," Opt. Lett., **34**, 3478-3480 (2009).

CHAPTER 5

Design of the Distribution of Constitutive Parameters

5.1. Introduction

From the analysis of cloaking devices by using the proposed Hamiltonian ray tracing in CHAPTER 4, the following issue for design of cloaking devices has been revealed. A coarse mesh representation causes the degradation of cloaking performance, especially for the ray passing through near the inner boundary. This degradation is considered to be due to the abrupt changes of relative permittivity and permeability near the inner boundary, which cannot be modelled by full-mesh representation accurately.

This issue will become very serious when cloaking devices are manufactured because the processing technology can realize the distributions of constituent parameters with finite resolution, but not rigorously. The resolution depends on the processing method. If only the processing method with low resolution can be utilized, the cloaking devices have to be designed by using coarse mesh representation, resulting in the degradation of cloaking performance. Therefore, the countermeasure has to be considered in order to improve cloaking performance with coarse mesh representation.

On the other hand, the distribution of the constituent parameters can be modified by changing the partial differential equation used in the numerical technique for the calculation of the constitutive parameters based on the Finite Element Method (FEM) [1].

If the distribution near the inner boundary can be made less decent, the cloaking performance is expected to be improved because the distribution can be modelled by the full-mesh representation accurately.

In this chapter, the improvement of performance of cylindrical cloaking is investigated by the design of distributions of constitutive parameters. The distributions of the constituent parameters are modified by employing the Navier's equation with various distributions of Young's modulus as the partial differential equation for the numerical technique for the calculation of the constitutive parameters. The performance of cylindrical cloaking is evaluated by Hamiltonian ray tracing.

5.2. Calculation of relative permittivity tensor and permeability tensor

As described in 2.2., relative permittivity tensor $\boldsymbol{\varepsilon}$ and relative permeability tensor $\boldsymbol{\mu}$ of cloaking devices with arbitrary shapes can be calculated by using the numerical technique with the FEM-based solution of the Laplace's equation. Besides the Laplace's equation, other partial differential equation can be adopted in order to calculate the displacement field and the deformation gradient tensor [2], resulting in the different distributions of $\boldsymbol{\varepsilon}$ and $\boldsymbol{\mu}$. In this thesis, the Navier's equation, corresponding to linear theory of elastic deformation of solids, is used to modify the distributions of $\boldsymbol{\varepsilon}$ and $\boldsymbol{\mu}$. The Navier's equation is expressed as follows,

$$-\nabla \cdot \boldsymbol{\tau} = 0, \tag{5-1}$$

where $\boldsymbol{\tau}$ is the stress tensor given by

$$\boldsymbol{\tau} = \frac{Y}{2(1+\kappa)}\zeta + \frac{Y\kappa}{(1+\kappa)(1-2\kappa)}\mathrm{tr}(\zeta)\cdot\mathbf{I}, \tag{5-2}$$

where Y is Young's modulus, κ Poisson ratio, $\mathbf{I}$ the identify matrix, tr(•) the trace function, and ζ the strain tensor given by

$$\zeta = \frac{1}{2}\left(\nabla \boldsymbol{U} + (\nabla \boldsymbol{U})^T\right), \tag{5-3}$$

where $\boldsymbol{U}$ is the displacement field.

Equations (5-1)-(5-3) indicate that the displacement field and the deformation gradient tensor can be changed by adjusting the distribution of Young's modulus, resulting in various distributions of ε and μ.

The solutions of the Laplace's equation and the Navier's equation are attained based on the FEM by employing the open source program, Elmer from CSC [3].

The FEM-based solution for ε and μ are discretized in triangular meshes inside of the cloaking device as shown in Fig. 5-1. On the other hand, the Hamiltonian-based ray tracing requires ε and μ in the entire region of cloaking devices. Therefore, interpolation of ε and μ is necessary for the Hamiltonian-based ray tracing. In this thesis, ε and μ are expressed as linear functions of the components of position vector inside each element used for the solution of the Laplace's equation or the Navier's equation.

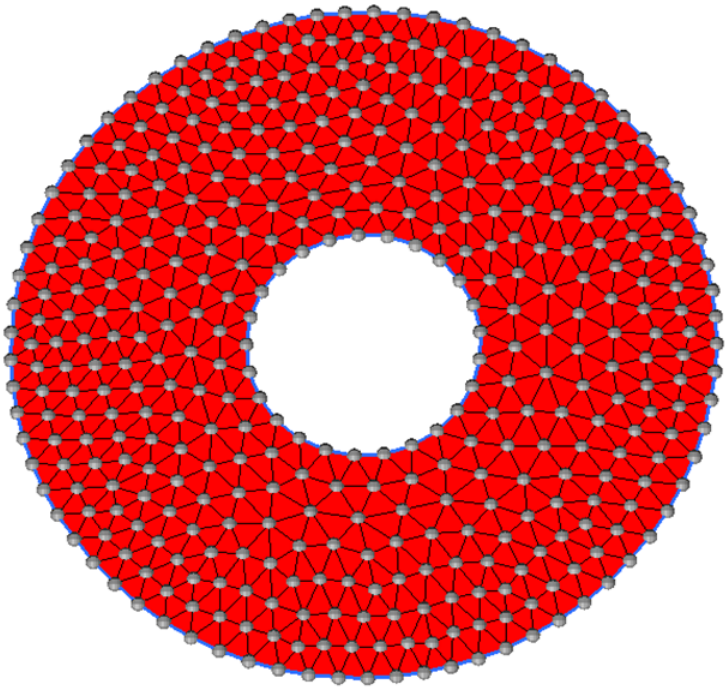

Fig. 5-1. The full-mesh representation approach.

5.3. Numerical results

5.3.1. Distributions of ε and μ for various Young's moduli

The distributions of ε and μ for the cylindrical cloaking device with the inner radius of 10 mm and the outer radius of 30 mm are calculated by the FEM-based numerical technique with five full-mesh resolutions of 2.5, 1.0, 0.5, 0.25, and 0.10 mm. As a partial differential equation, the Navier's equation with various distributions of Young's modulus is employed. In addition, the distributions of ε and μ for the Laplace's equation are calculated for comparison with those for the Navier's equation. Here, the relative full-mesh resolution defined as the ratio of the mesh size and the representative length of the cloaking device in 4.3.1, is adopted so that it can be generally applied to any other

structure. The representative length is determined to be the size of the cloaking device. The size of the cloaking device corresponds to 60 mm, the diameter of the outer cylinder of the cylindrical cloaking device. Therefore, the relative mesh resolutions for 2.5, 1.0, 0.5, 0.25, and 0.10 mm correspond to 4.17e–02, 1.67e–02, 8.33e–03, 4.17e–03, and 1.67e–03. Hereafter, the numerical results are investigated based on the relative mesh resolution.

The value of the Young's modulus (Y) depends on the distance between the position and the center of the cylinder represented by d. In the numerical evaluation, the following seven distributions are considered: (i) $Y = d^{-5}$, (ii) $Y = d^{-3}$, (iii) $Y = d^{-1}$, (vi) $Y = d^{0}$, (v) $Y = d^{1}$, (vi) $Y = d^{3}$, and (vii) $Y = d^{5}$. The seven distributions of Young's modulus are depicted in Fig. 5-2. Here, since the cloaking media are supposed to be impedance-matched with the surrounding medium, ε is equal to μ. Therefore, only the calculation results of ε are shown hereafter.

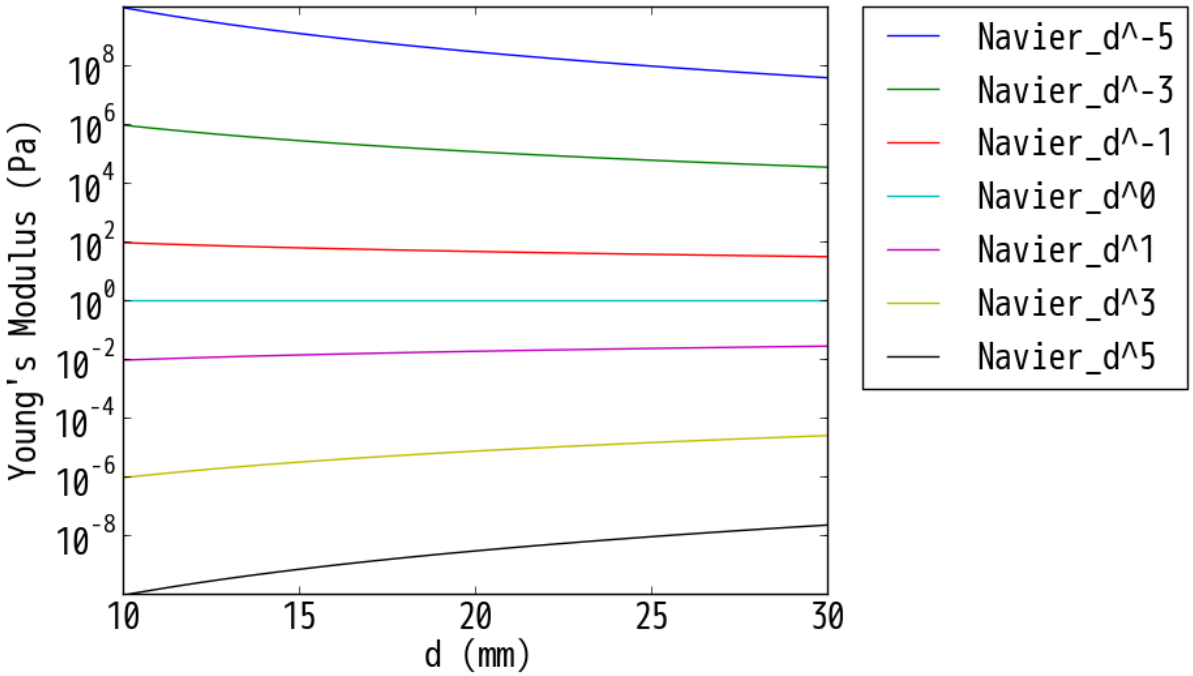

Fig. 5-2. The various distributions of Young's modulus.

The distributions of the three principal permittivities, ε_r, ε_ϕ, and ε_z calculated for the Laplace's equation at the relative full-mesh resolution of 1.67e–03 are illustrated in Fig. 5-3. The principal axes for ε_r, ε_ϕ, and ε_z correspond to the radial axis, the azimuthal axis, and the z axis, respectively. Figure 5-3 reveals that each distribution has the axial symmetry. In the same way, the distributions of the three principal permittivities calculated for the Navier's equation with various distributions of Y have the axial symmetry.

The profiles of ε_r, ε_ϕ, and ε_z along the radial axis at the relative full-mesh resolution of 1.67e–03 are depicted in Fig. 5-4. In addition, the profiles of ε_ϕ near the inner boundary and the outer boundary are extended in Fig. 5-5. From Fig. 5-4 and Fig. 5-5, the following common characteristics for the different distributions of Y in each of the three principal permittivities can be noticed. ε_ϕ increases drastically near the inner boundary,

while ε_r and ε_z approach 0.0. Although these characteristics lead to superluminal propagation, they are required to realize invisibility cloaking.

Generally, the three principal permittivities of the cylindrical cloaking device with the inner radius of a and the outer radius of b can be represented by considering the space transformation from (r, ϕ, z) to (r', ϕ', z') as [1]

$$\varepsilon_r = \frac{\psi \cdot r}{r'}, \tag{5-4a}$$

$$\varepsilon_\phi = \frac{r'}{\psi \cdot r}, \tag{5-4b}$$

$$\varepsilon_z = \frac{r}{\psi \cdot r'}, \tag{5-4c}$$

where ψ is the derivative of r' with respect of r expressed as

$$\psi = \frac{dr'}{dr}. \tag{5-5}$$

Equations (5-4a)-(5-4c) can explain the characteristics of the distributions of the three principal permittivities described above as follows,

$$r' \to a,\ r \to 0 \Rightarrow\ \varepsilon_r \to 0,\ \varepsilon_\phi \to \infty,\ \varepsilon_z \to 0. \tag{5-6}$$

By contrast, the variation of distribution of Y can yield the following differences in the profiles. The increase rate of ε_r and the decrease rate of ε_ϕ with the increase of d can be changed. The increase rate of ε_r gets larger in the order from $Y=d^{-5}$ to $Y=d^5$, resulting in the increase of the value of ε_r at the outer boundary in the same order. On the other hand, the decrease rate of ε_ϕ decreases in the same order, leading to the decrease of the value of ε_ϕ at the outer boundary in the same order. Furthermore, it can be noticed that the profiles of ε_z have a turning point around d=22 mm. The increase rate of ε_z increases in the order

from $Y=d^{-5}$ to $Y=d^{5}$ in the range between the inner boundary and the turning point, while it increases in the order from $Y=d^{5}$ to $Y=d^{-5}$ in the range between the turning point and the outer boundary. Hence, the value of ε_z at the outer boundary increases in the order from $Y=d^{5}$ to $Y=d^{-5}$.

By comparing the profiles from the Navier's equation with those from the Laplace's equation, it can be seen that the profiles from Laplace's equation are very similar to those from the Navier's equation with $Y=d^{0}$.

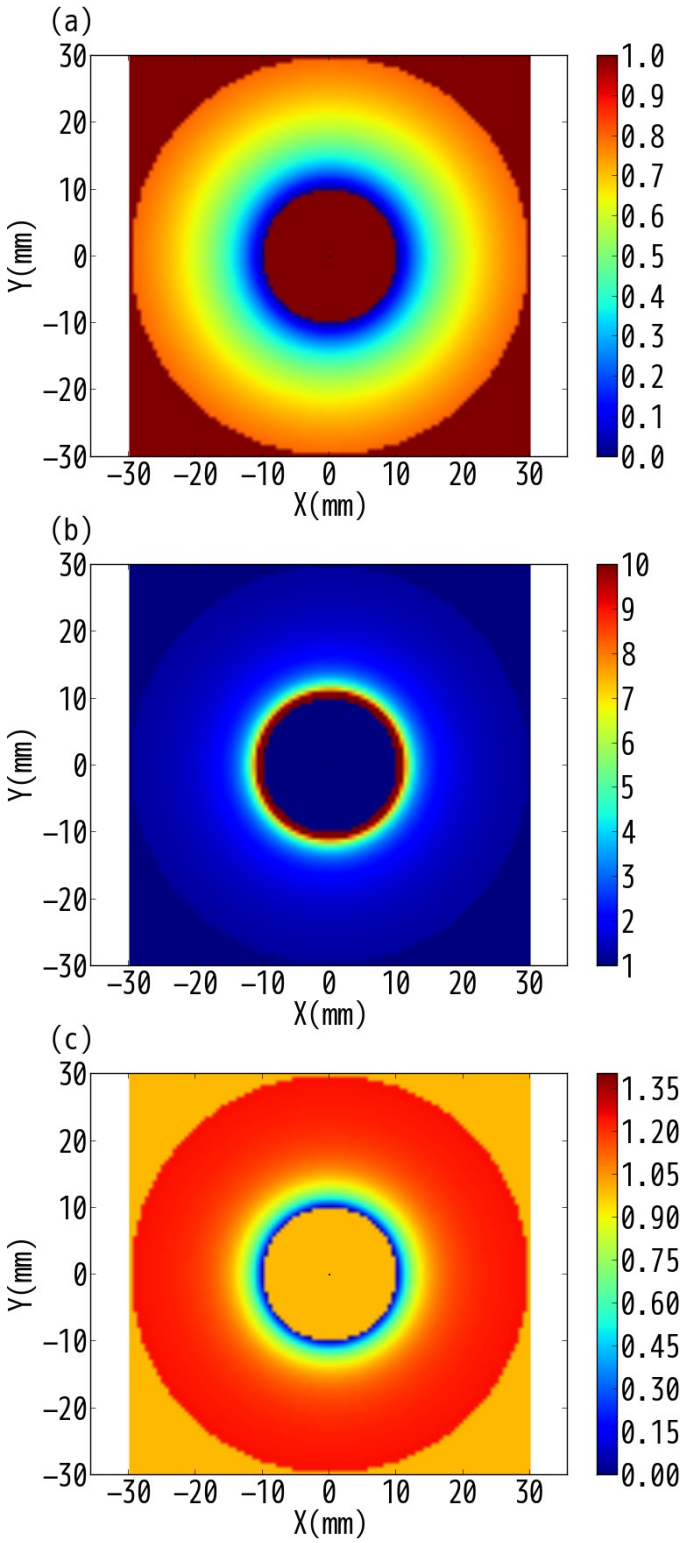

Fig. 5-3. The distributions of the three principal permittivities, (a) ε_r, (b) ε_ϕ, and (c) ε_z for the Laplace's equation.

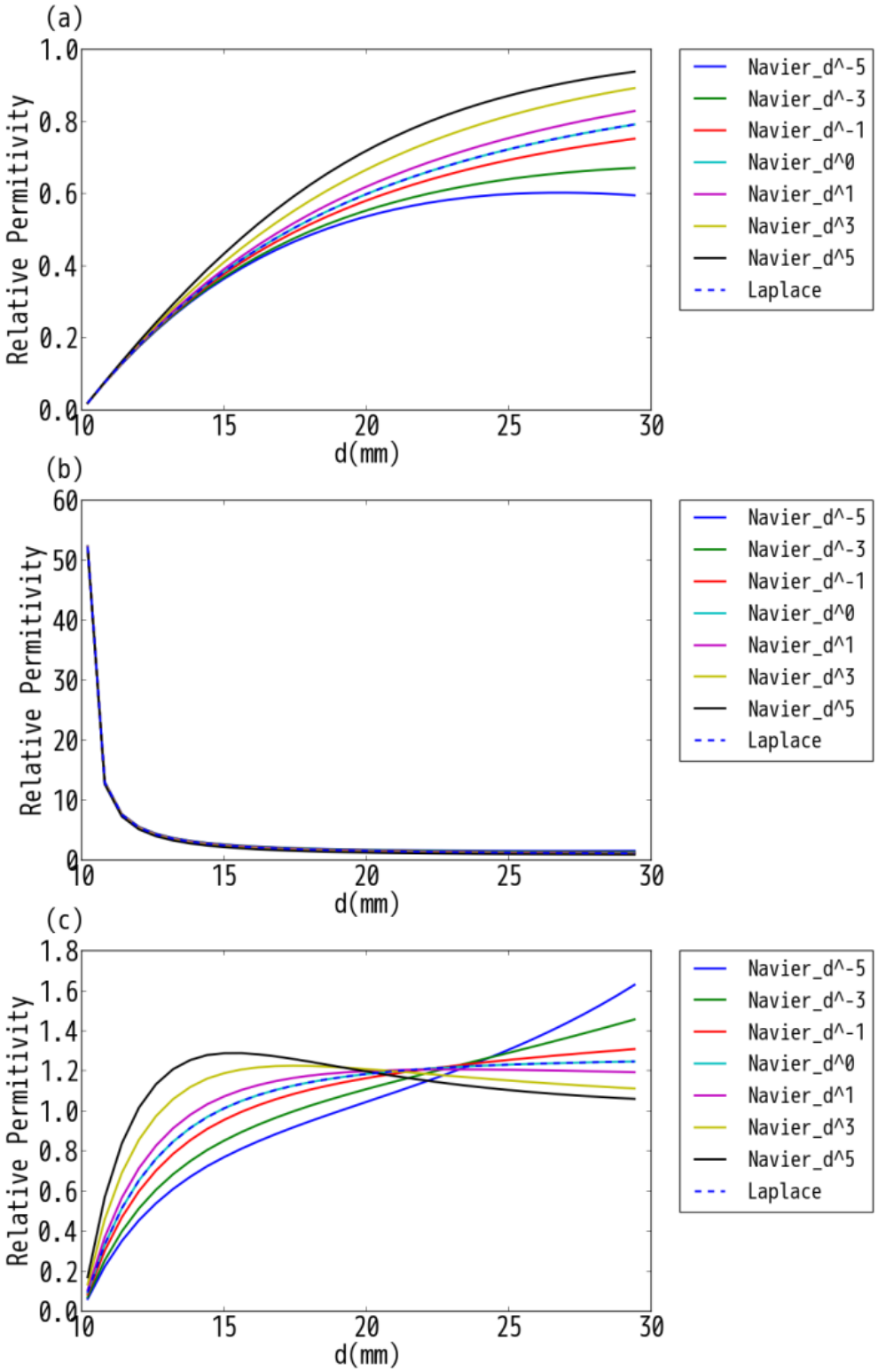

Fig. 5-4. The profiles of (a) ε_r, (b) ε_ϕ, and (c) ε_Z along the radial axis.

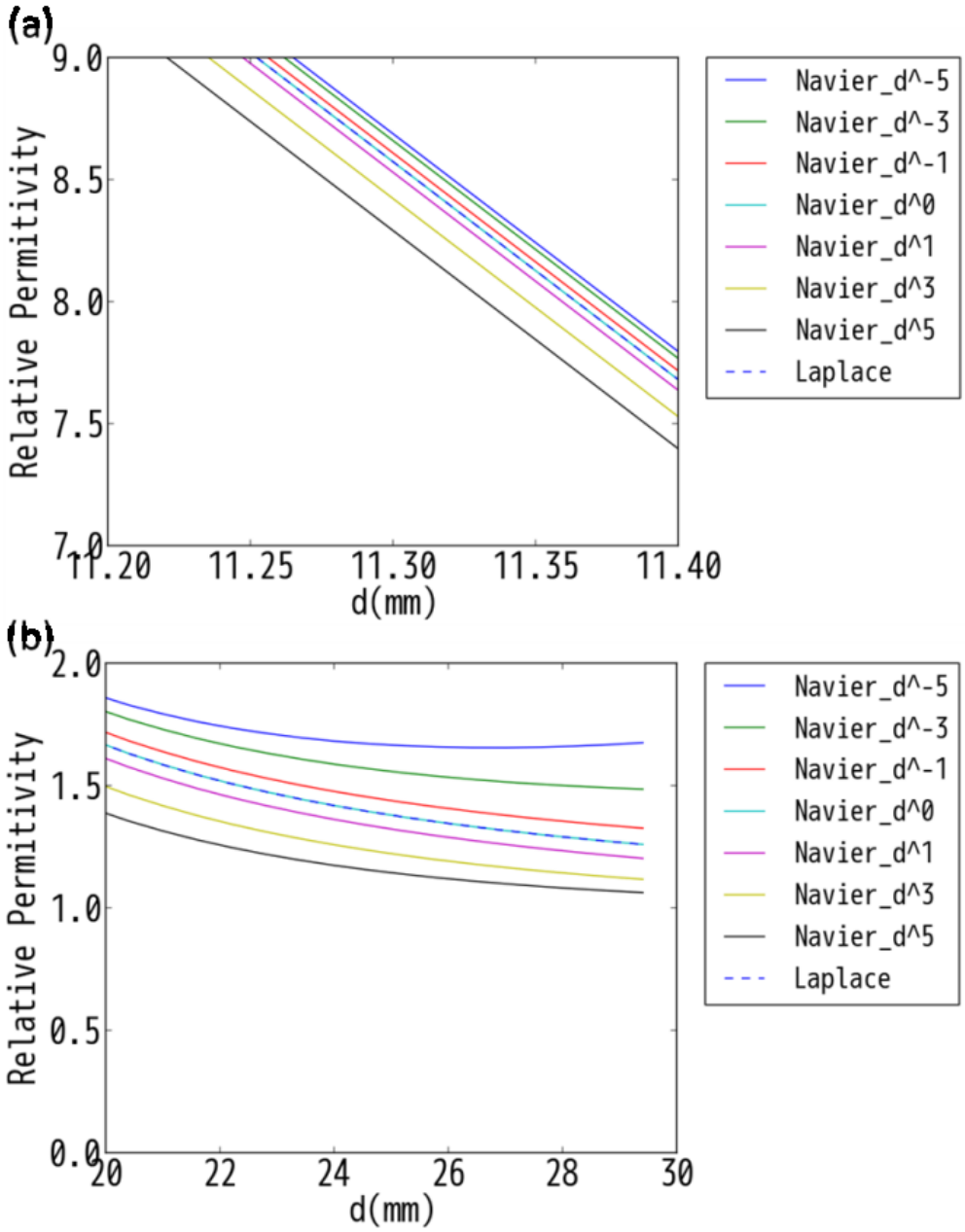

Fig. 5-5. The profiles of ε_ϕ along the radial axis; (a) near the inner boundary, (b) near the outer boundary.

5.3.2. Performance for various Young's modulus

The performance of the cylindrical cloaking device is calculated by the Hamiltonian-based ray tracing with the distributions of ε and μ obtained in 5.3.1. The cloaking device is represented by the full-mesh representation with five relative full-mesh resolutions of 4.17e–02, 1.67e–02, 8.33e–03, 4.17e–03, and 1.67e–03.

The ray trajectories calculated for the five relative full-mesh resolutions are depicted in Figs. 5-6, 5-8, 5-10, 5-12, and 5-14, respectively. The dependence of the cloaking performance on the radiation angle for the five relative full-mesh resolutions are shown in Figs. 5-7, 5-9, 5-11, 5-13, and 5-15, respectively. Table 5-1 summarizes the calculated cloaking performance. Table 5-1 reveals the tendency that the cloaking performance becomes higher in the order from $Y=d^5$ to $Y=d^{-5}$. Especially, this trend is found to be distinct at the relative full-mesh resolution of 4.17e–03 as shown in Fig. 5-16.

Figures 5-12 and 5-13 indicate that the performance at the relative full-mesh resolution of 4.17e–03 is degraded around a radiation angle of 0.0° for the Navier's equation with $Y=d^m$ (m=–1, 1, 3, and 5) as well as for the Laplace's equation. By contrast, it is found to be improved for $Y=d^m$ (m=–3, –5) in comparison with the Laplace's equation. These results suggest the possibility that the modification of the distribution of Y can heighten the cloaking performance.

Additionally, the performance for the Laplace's equation is found to be similar to that for the Navier's equation with $Y=d^0$. This can be explained by the very similar distributions of ε and μ for the two cases as described in 5.3.1.

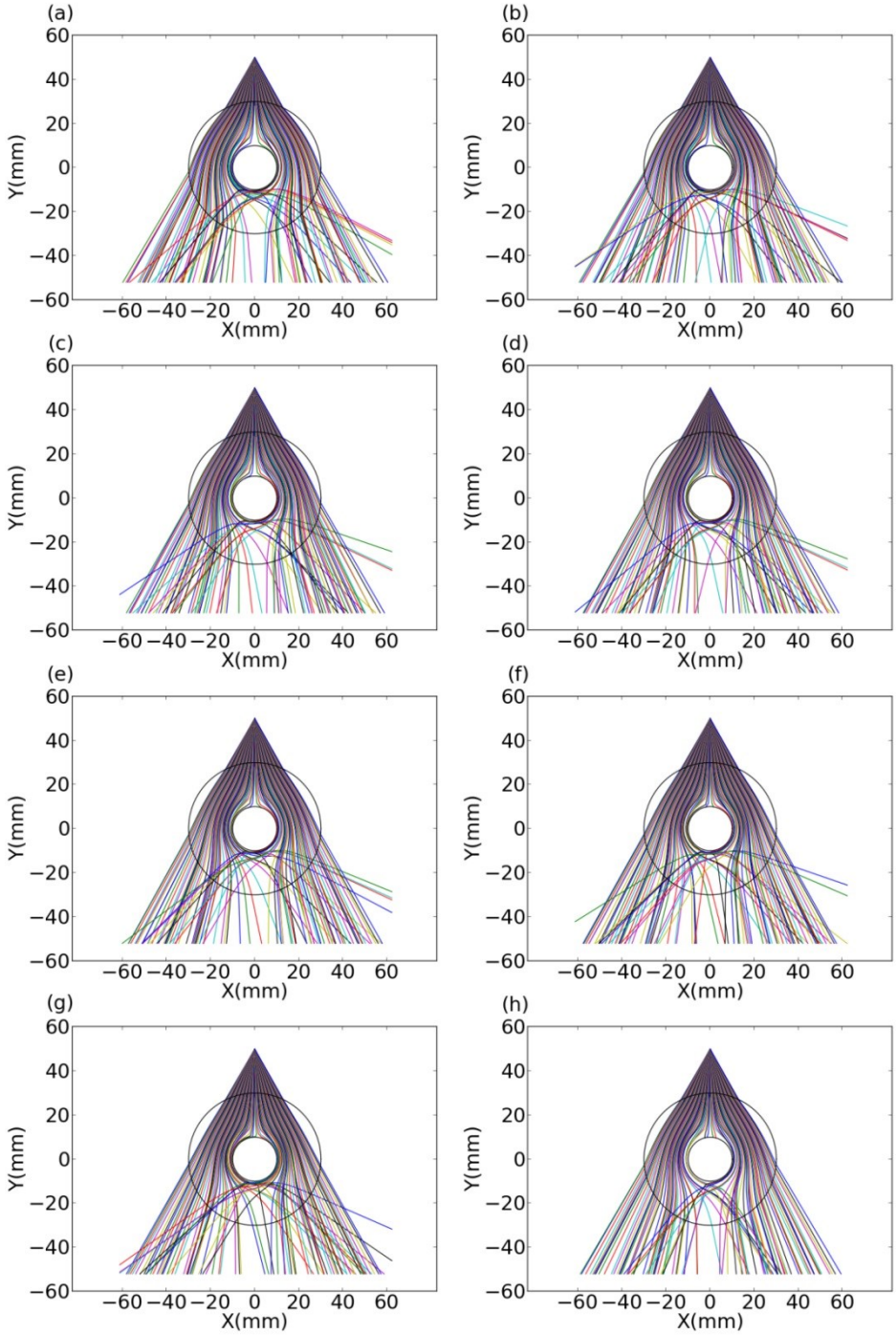

Fig. 5-6. The ray trajectoriess with the cylindrical cloaking device for the distributions of **ε** and **μ** obtained by the FEM-based solution of the Navier's equation with various distribution of Young modulus (Y); (a) $Y = d^{-5}$, (b) $Y = d^{-3}$, (c) $Y = d^{-1}$, (d) $Y = d^{0}$, (e) $Y = d^{1}$, (f) $Y = d^{3}$, and (g) $Y = d^{5}$. As a reference, the rays trajectories for the Laplace's equation is shown in (h). The relative full-mesh resolution is 4.17e−02.

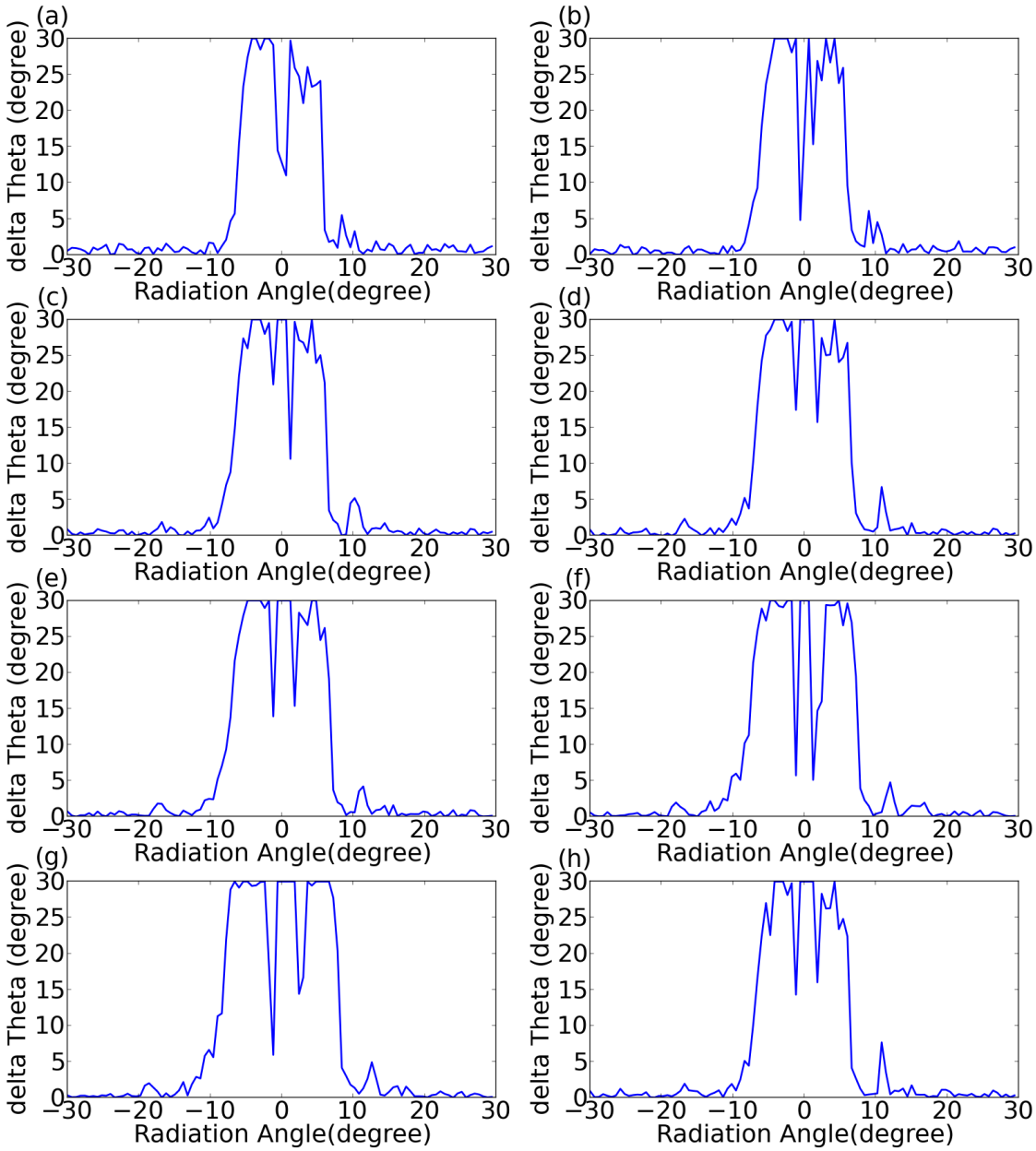

Fig. 5-7. The dependences of the cloaking performance on the radiation angle for the distributions of ε and μ obtained by the FEM-based solution of the Navier's equation with various distribution of Young modulus (Y); (a) $Y = d^{-5}$, (b) $Y = d^{-3}$, (c) $Y = d^{-1}$, (d) $Y = d^{0}$, (e) $Y = d^{1}$, (f) $Y = d^{3}$, and (g) $Y = d^{5}$. As a reference, the profile for the Laplace's equation is shown in (h). The relative full-mesh resolution is 4.17e−02.

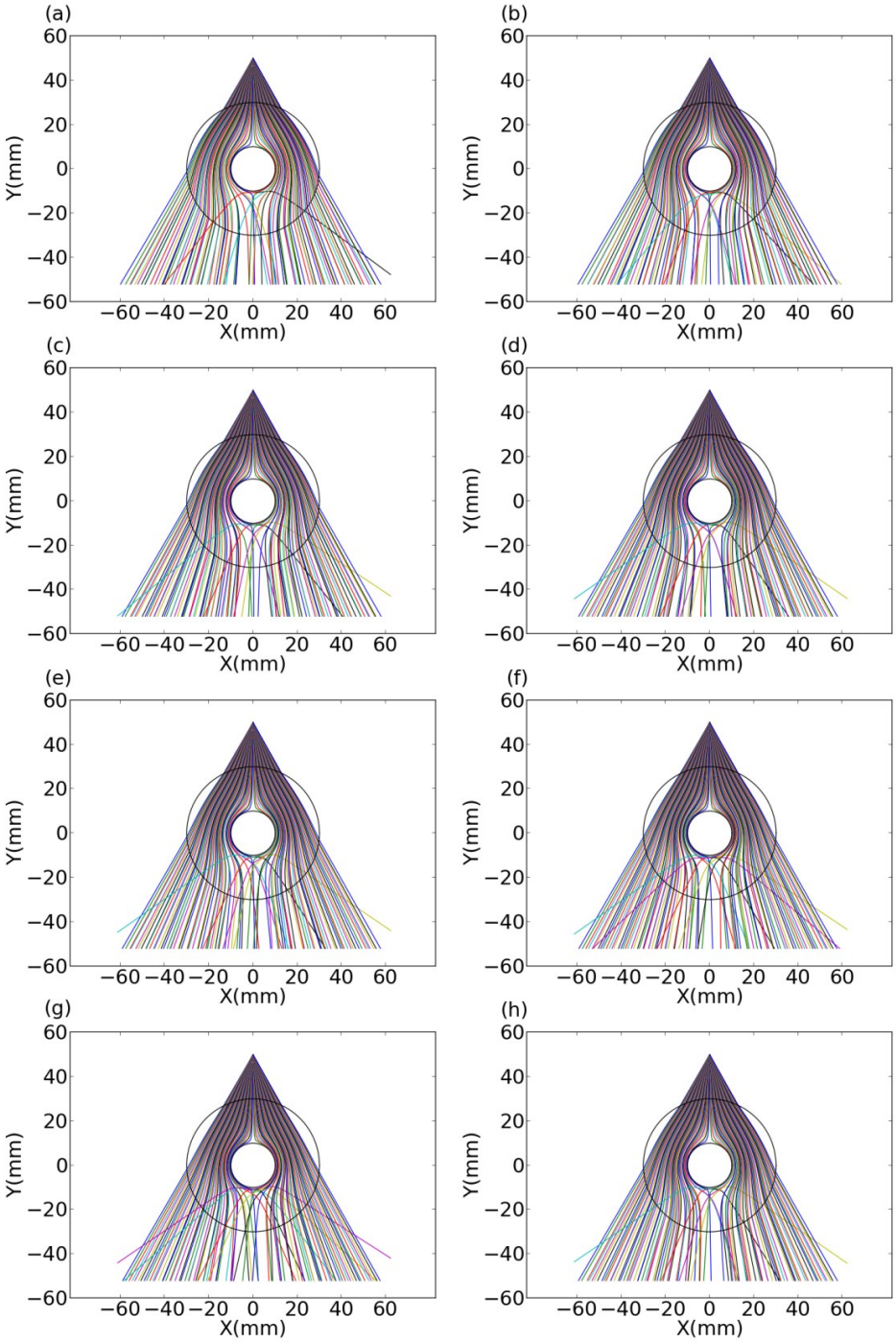

Fig. 5-8. The ray trajectoriess with the cylindrical cloaking device for the distributions of **ε** and **μ** obtained by the FEM-based solution of the Navier's equation with various distribution of Young modulus (Y); (a) $Y = d^{-5}$, (b) $Y = d^{-3}$, (c) $Y = d^{-1}$, (d) $Y = d^{0}$, (e) $Y = d^{1}$, (f) $Y = d^{3}$, and (g) $Y = d^{5}$. As a reference, the rays trajectories for the Laplace's equation is shown in (h). The relative full-mesh resolution is 1.67e–02.

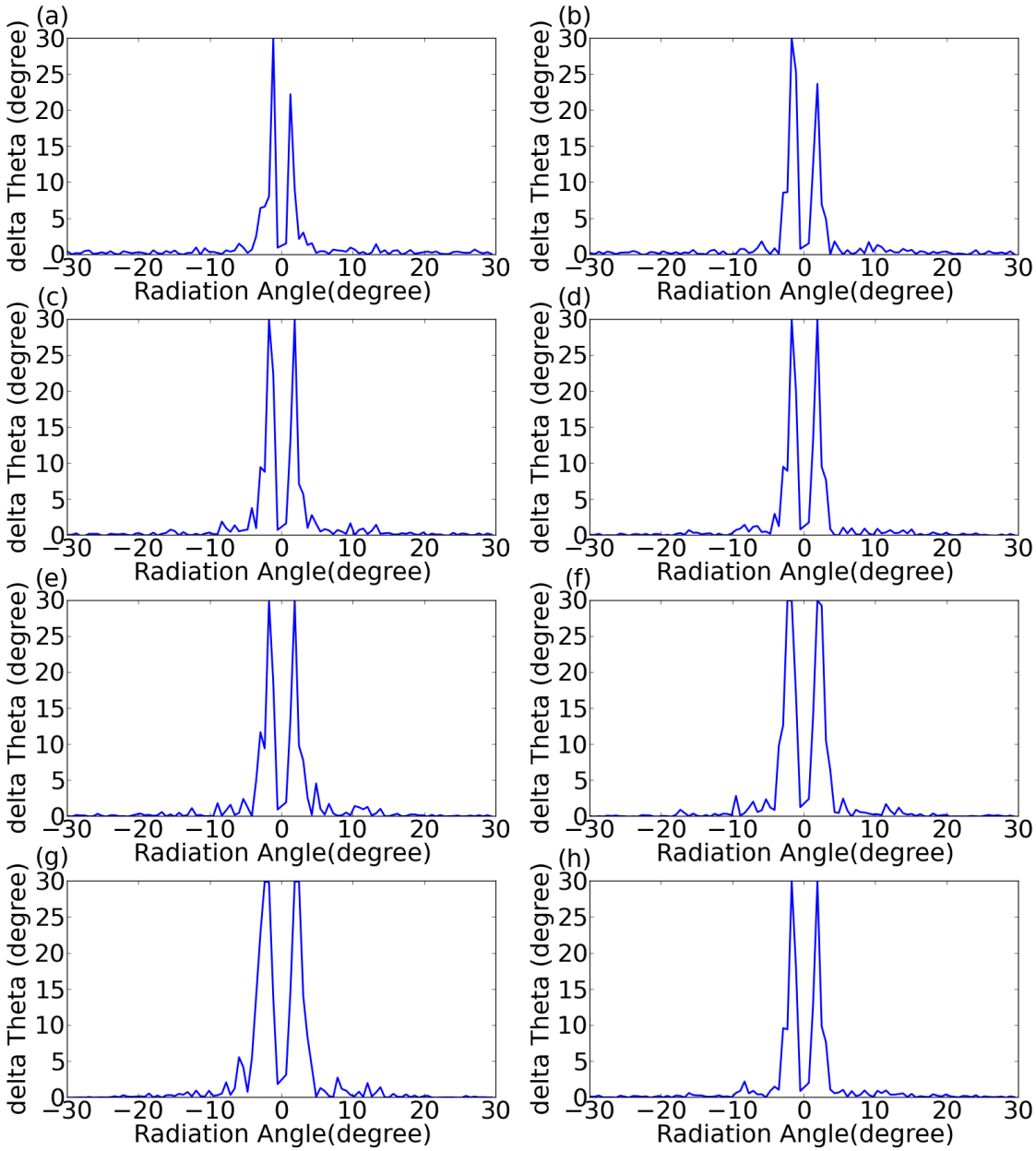

Fig. 5-9. The dependences of the cloaking performance on the radiation angle for the distributions of ε and μ obtained by the FEM-based solution of the Navier's equation with various distribution of Young modulus (Y); (a) $Y = d^{-5}$, (b) $Y = d^{-3}$, (c) $Y = d^{-1}$, (d) $Y = d^{0}$, (e) $Y = d^{1}$, (f) $Y = d^{3}$, and (g) $Y = d^{5}$. As a reference, the profile for the Laplace's equation is shown in (h). The relative full-mesh resolution is 1.67e−02.

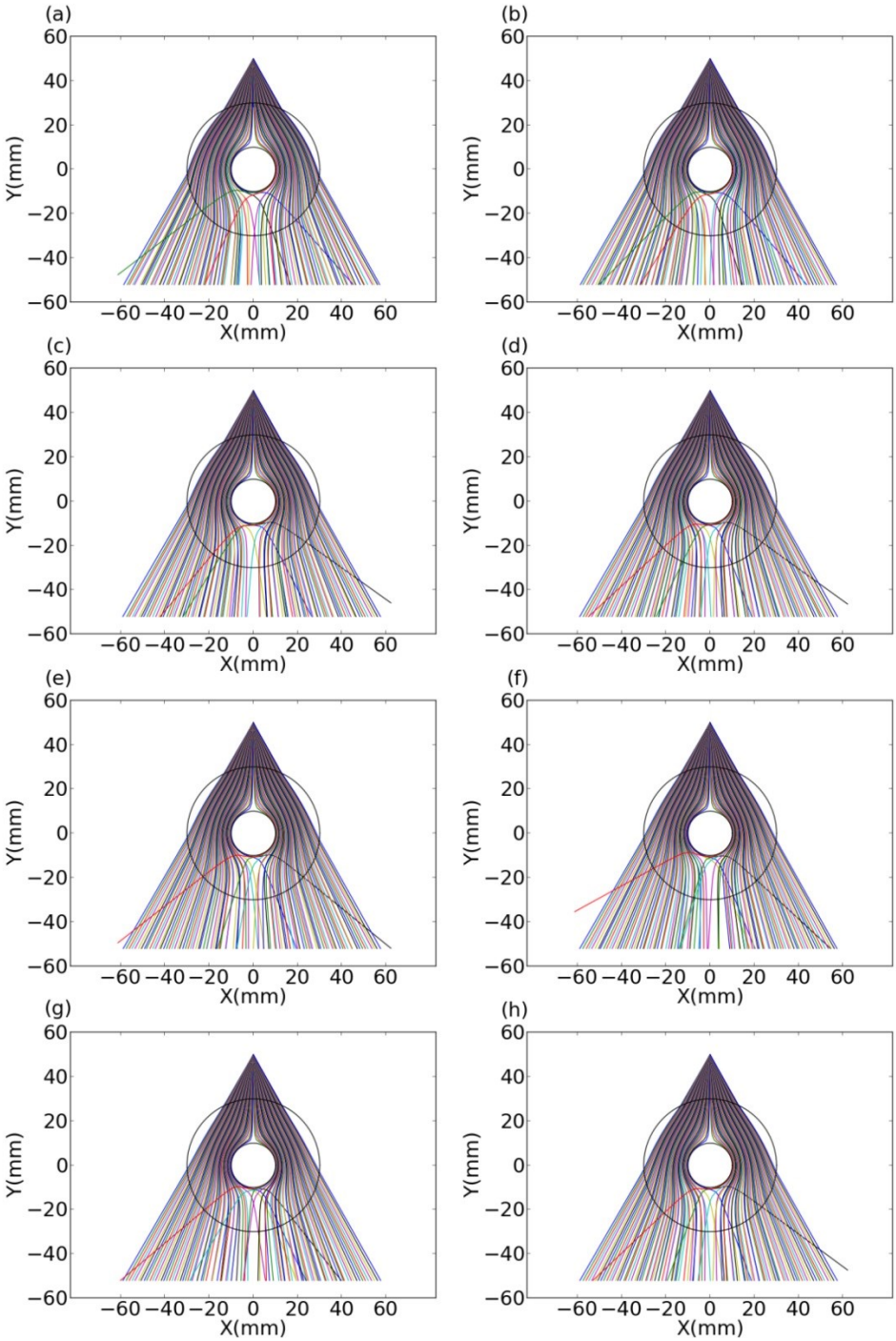

Fig. 5-10. The ray trajectoriess with the cylindrical cloaking device for the distributions of **ε** and **μ** obtained by the FEM-based solution of the Navier's equation with various distribution of Young modulus (Y); (a) $Y = d^{-5}$, (b) $Y = d^{-3}$, (c) $Y = d^{-1}$, (d) $Y = d^{0}$, (e) $Y = d^{1}$, (f) $Y = d^{3}$, and (g) $Y = d^{5}$. As a reference, the rays trajectories for the Laplace's equation is shown in (h). The relative full-mesh resolution is 8.33e–03.

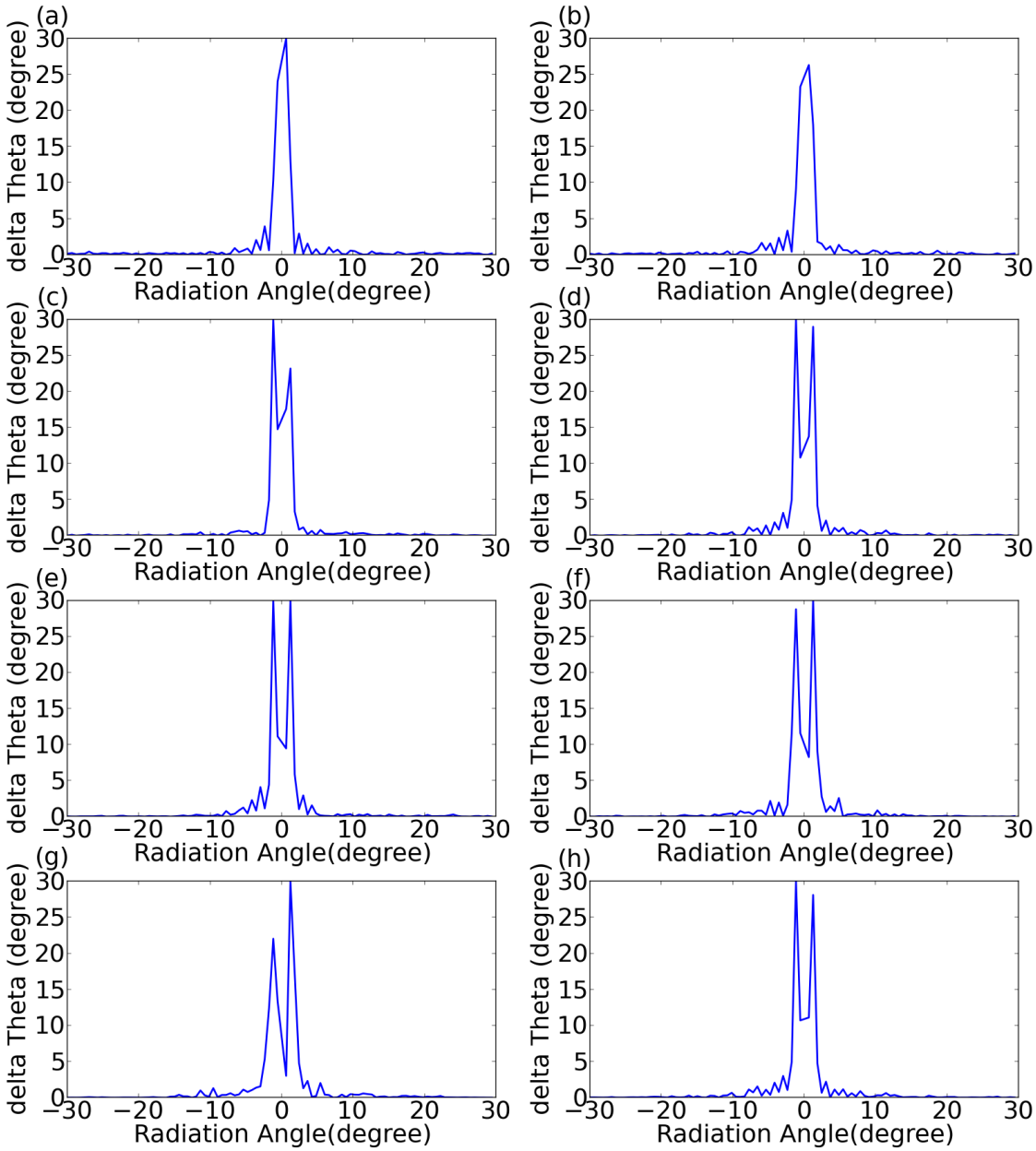

Fig. 5-11. The dependences of the cloaking performance on the radiation angle for the distributions of ε and μ obtained by the FEM-based solution of the Navier's equation with various distribution of Young modulus (Y); (a) $Y = d^{-5}$, (b) $Y = d^{-3}$, (c) $Y = d^{-1}$, (d) $Y = d^{0}$, (e) $Y = d^{1}$, (f) $Y = d^{3}$, and (g) $Y = d^{5}$. As a reference, the profile for the Laplace's equation is shown in (h). The relative full-mesh resolution is 8.33e−03.

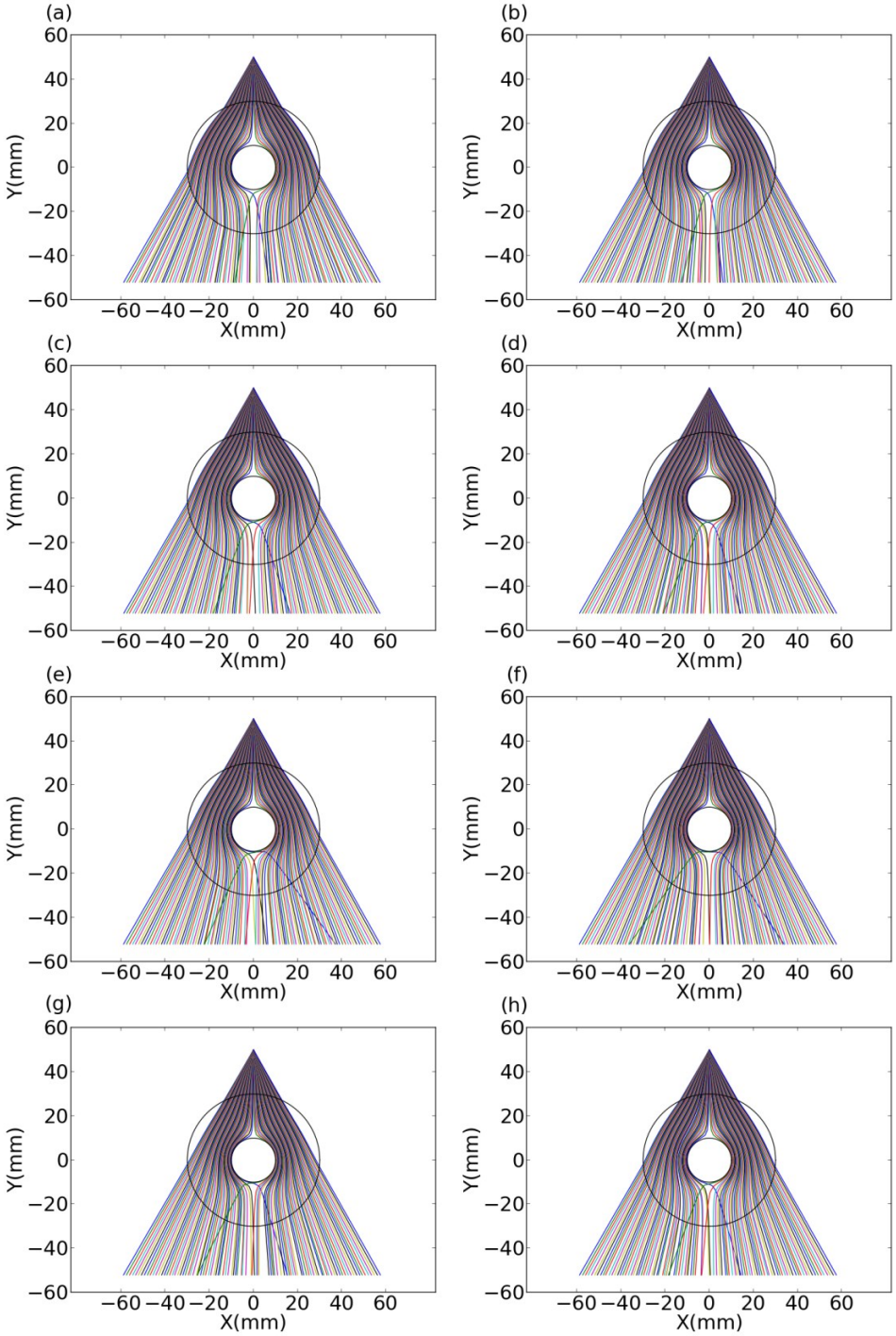

Fig. 5-12. The ray trajectoriess with the cylindrical cloaking device for the distributions of **ε** and **μ** obtained by the FEM-based solution of the Navier's equation with various distribution of Young modulus (Y); (a) $Y = d^{-5}$, (b) $Y = d^{-3}$, (c) $Y = d^{-1}$, (d) $Y = d^{0}$, (e) $Y = d^{1}$, (f) $Y = d^{3}$, and (g) $Y = d^{5}$. As a reference, the rays trajectories for the Laplace's equation is shown in (h). The relative full-mesh resolution is 4.17e–03.

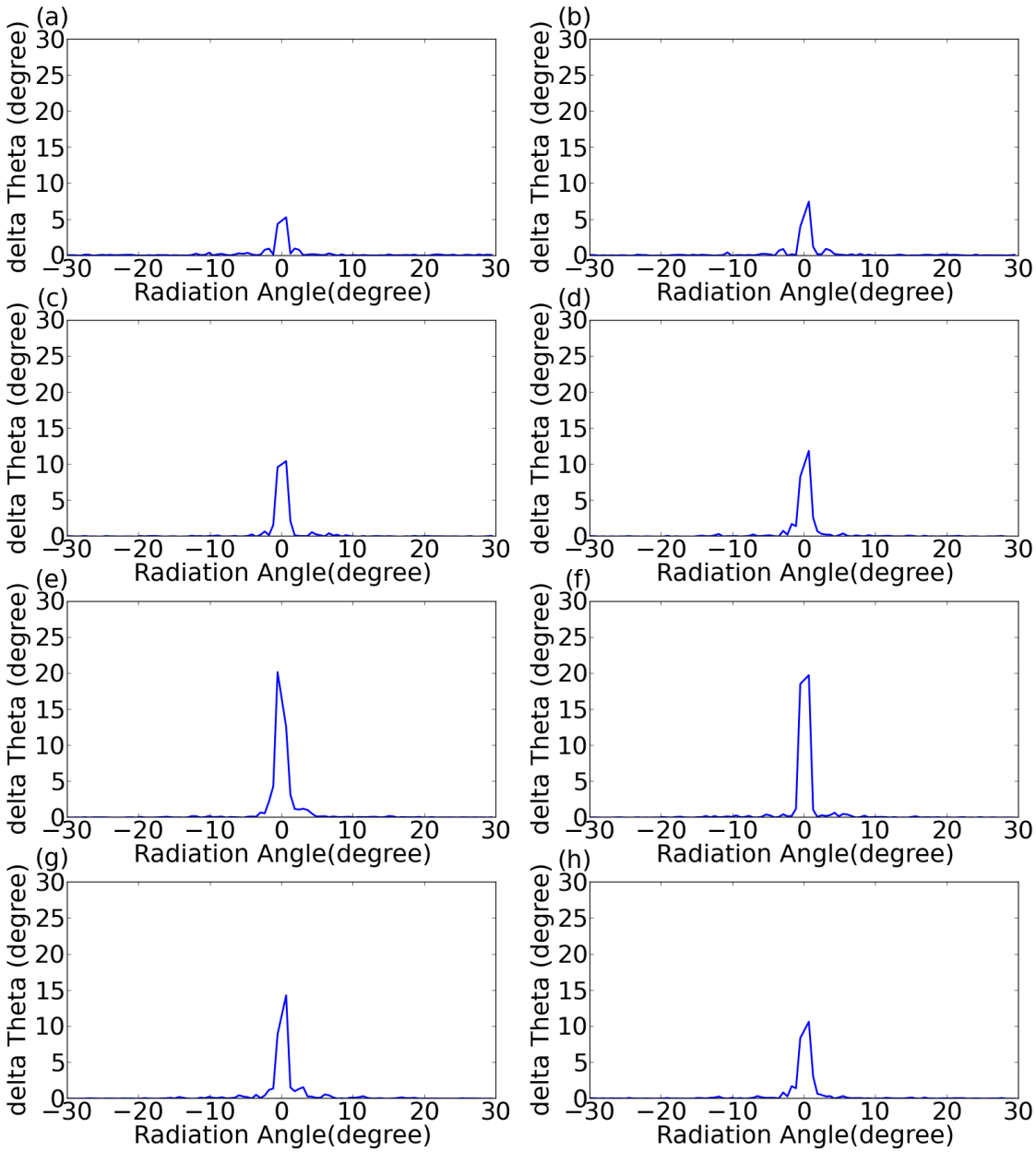

Fig. 5-13. The dependences of the cloaking performance on the radiation angle for the distributions of **ε** and **μ** obtained by the FEM-based solution of the Navier's equation with various distribution of Young modulus (Y); (a) $Y = d^{-5}$, (b) $Y = d^{-3}$, (c) $Y = d^{-1}$, (d) $Y = d^{0}$, (e) $Y = d^{1}$, (f) $Y = d^{3}$, and (g) $Y = d^{5}$. As a reference, the profile for the Laplace's equation is shown in (h). The relative full-mesh resolution is 4.17e–03.

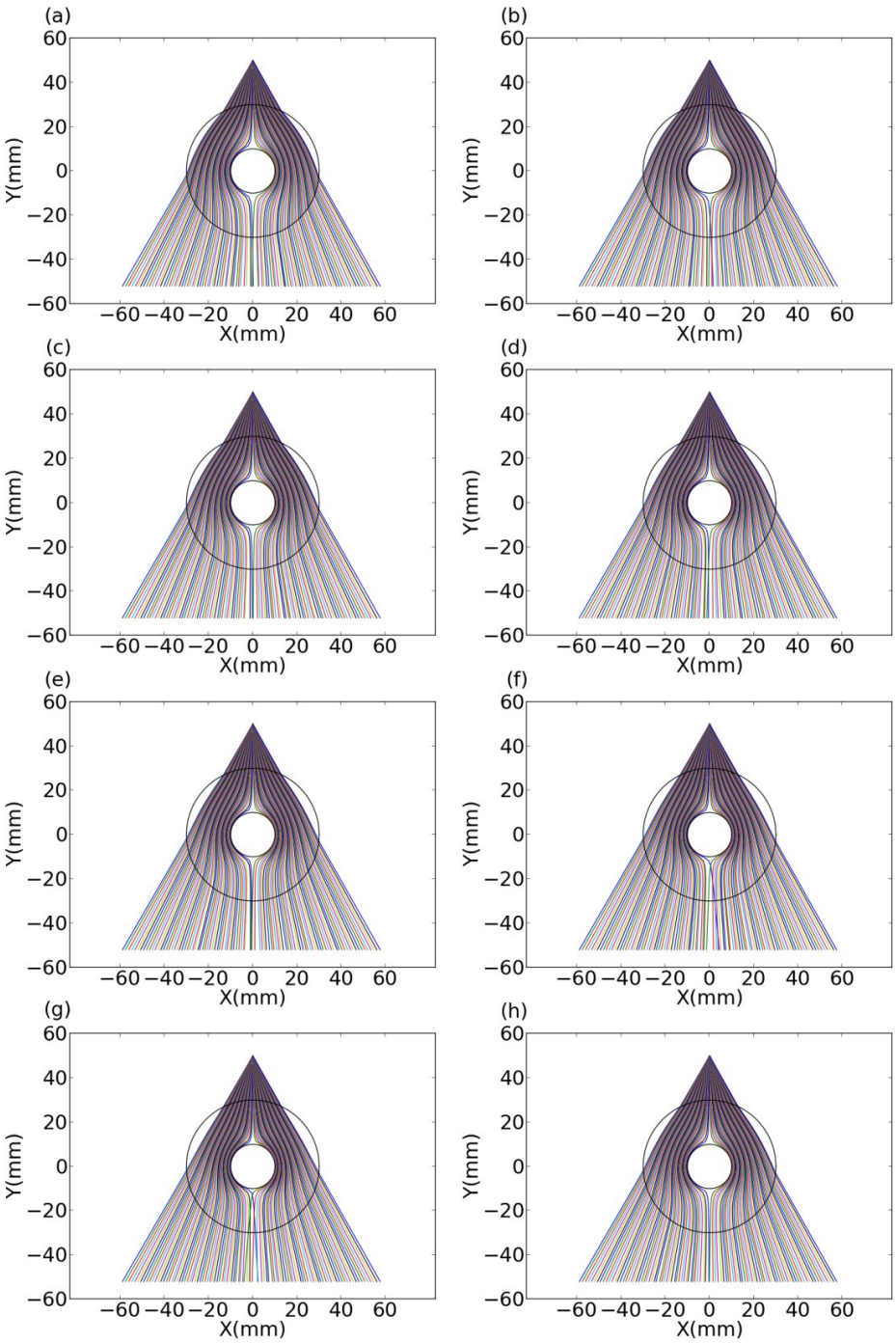

Fig. 5-14. The ray trajectoriess with the cylindrical cloaking device for the distributions of **ε** and **μ** obtained by the FEM-based solution of the Navier's equation with various distribution of Young modulus (Y); (a) $Y = d^{-5}$, (b) $Y = d^{-3}$, (c) $Y = d^{-1}$, (d) $Y = d^{0}$, (e) $Y = d^{1}$, (f) $Y = d^{3}$, and (g) $Y = d^{5}$. As a reference, the rays trajectories for the Laplace's equation is shown in (h). The relative full-mesh resolution is 1.67e–03.

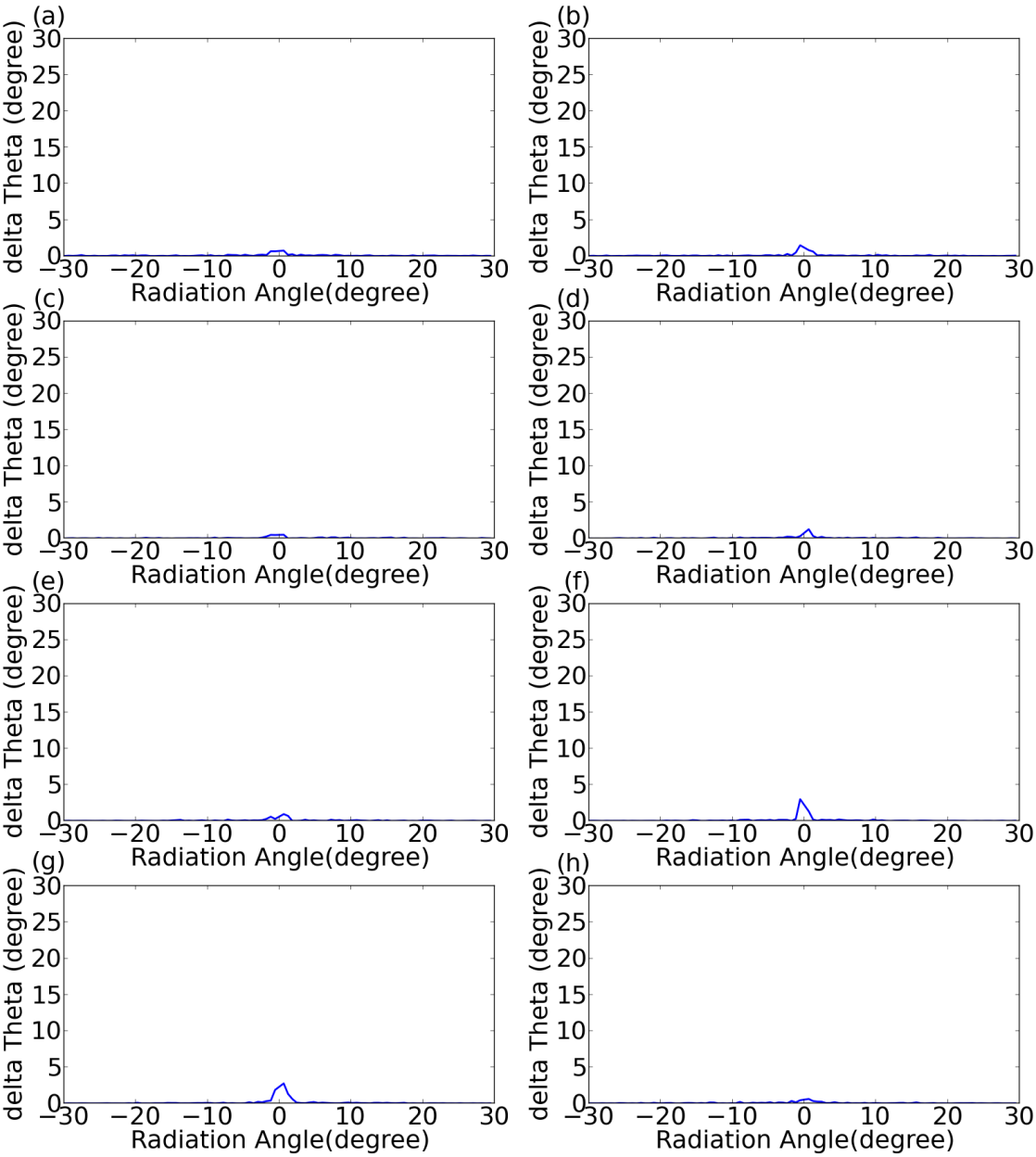

Fig. 5-15. The dependences of the cloaking performance on the radiation angle for the distributions of ε and μ obtained by the FEM-based solution of the Navier's equation with various distribution of Young modulus (Y); (a) $Y = d^{-5}$, (b) $Y = d^{-3}$, (c) $Y = d^{-1}$, (d) $Y = d^{0}$, (e) $Y = d^{1}$, (f) $Y = d^{3}$, and (g) $Y = d^{5}$. As a reference, the profile for the Laplace's equation is shown in (h). The relative full-mesh resolution is 1.67e−03.

Table 5-1: Performances of cylindrical cloaking calculated for the distributions of ε and μ obtained by the FEM-based solution of the Navier's equation with various distribution of Young modulus (*Y*) and the Laplace's equation.

Number	Relative full-mesh resolution	Equations		Δθ(°)
1	4.17e−02	Navier's Eqn.	$Y=d^{-5}$	11.1
2			$Y=d^{-3}$	11.7
3			$Y=d^{-1}$	12.2
4			$Y=d^{0}$	12.4
5			$Y=d^{1}$	12.9
6			$Y=d^{3}$	13.1
7			$Y=d^{5}$	14.2
8		Laplace's Eqn.		12.1
9	1.67e−02	Navier's Eqn.	$Y=d^{-5}$	4.12
10			$Y=d^{-3}$	5.04
11			$Y=d^{-1}$	5.31
12			$Y=d^{0}$	5.26
13			$Y=d^{1}$	5.32
14			$Y=d^{3}$	6.74
15			$Y=d^{5}$	7.20
16		Laplace's Eqn.		5.19
17	8.33e−03	Navier's Eqn.	$Y=d^{-5}$	4.26
18			$Y=d^{-3}$	4.12
19			$Y=d^{-1}$	4.50
20			$Y=d^{0}$	4.63
21			$Y=d^{1}$	4.62
22			$Y=d^{3}$	4.70
23			$Y=d^{5}$	4.61
24		Laplace's Eqn.		4.51
25	4.17e−03	Navier's Eqn.	$Y=d^{-5}$	0.729
26			$Y=d^{-3}$	0.887
27			$Y=d^{-1}$	1.46
28			$Y=d^{0}$	1.51

29			$Y=d^{1}$	2.48
30			$Y=d^{3}$	2.74
31			$Y=d^{5}$	1.74
32			Laplace's Eqn.	1.43
33	1.67e−03	Navier's Eqn.	$Y=d^{-5}$	0.144
34			$Y=d^{-3}$	0.198
35			$Y=d^{-1}$	0.108
36			$Y=d^{0}$	0.154
37			$Y=d^{1}$	0.151
38			$Y=d^{3}$	0.340
39			$Y=d^{5}$	0.374
40			Laplace's Eqn.	0.113

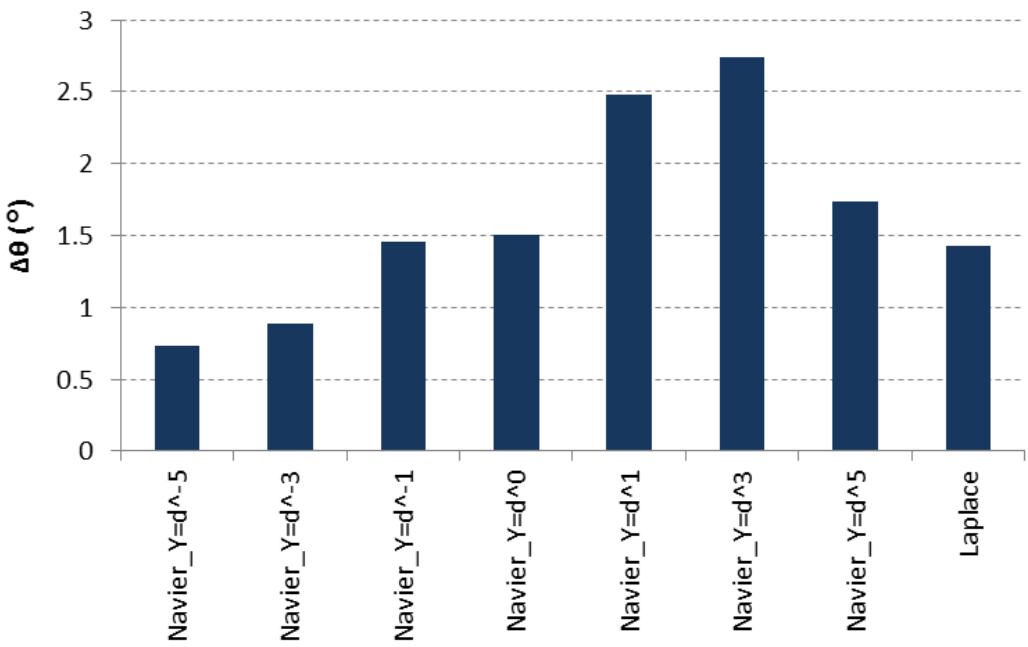

Fig. 5-16. The dependence of cloaking performance on the distribution of Y at the relative mesh resolution of 4.17e−2.

5.4. Discussion

5.4.1. Effects of Young's modulus on the distribution of ε and μ

Here, the effects of Young's modulus on the distributions of ε and μ are investigated. From Eqs. (5-4a)-(5-4c), Young's modulus is found to modify the distributions of ε and μ through the value of ψ given by Eq. (5-5). The expression of ψ can be rewritten by

$$\psi = \frac{dr'}{dr} = \frac{d(r+U_r)}{dr} = 1 + \frac{dU_r}{dr}, \tag{5-7}$$

where U_r is the displacement in the radial direction and dU_r/dr the strain in the radial direction. From Eq. (5-7), the value of ψ is found to increase with increasing the value of the strain. Because the space transformation from (r, ϕ, z) to (r', ϕ', z') compresses the region in the radial direction, the value of dU_r/dr becomes negative. In contrast, the larger value of Young's modulus is considered to yield the smaller absolute value of dU_r/dr from the viewpoint of continuum mechanics. Therefore, by increasing the value of Young's modulus, the value of dU_r/dr gets close to 0, resulting in the larger value of ψ.

From the effects of Young's modulus on the value of ψ described above, the distributions of Young's modulus which increase from the inner boundary to the outer boundary, such as $Y= d^1$, d^3, and d^5, are considered to yield smaller values of ψ at the inner boundary than those which decrease from the inner boundary to the outer boundary, such as $Y= d^{-1}$, d^{-3}, and d^{-5}. On the other hand, the distributions of Young's modulus which increase from the inner boundary to the outer boundary are considered to yield larger values of ψ at the outer boundary than those which decrease from the inner boundary to the outer boundary.

The relationship between r and r' for various distributions of Young's modulus is

shown in Fig. 5-17. The slopes of the curves correspond to the values of ψ as described in Eq. (5-7). From Fig. 5-17, the value of ψ at the inner boundary is found to increase in the order from $Y= d^5$ to $Y=d^{-5}$. On the other hand, the value of ψ at the outer boundary is found to increase in the order from $Y= d^{-5}$ to $Y=d^5$. These trends are in agreement with the effects of Young's modulus on the value of ψ.

The calculated results shown in Fig. 5-4 and Fig. 5-5 can be explained by the value of ψ as follows. Looking at ε_r, ε_ϕ, and ε_z at the outer boundary, these values can be expressed as follows:

$$r' \to b, r \to b \Rightarrow \varepsilon_r \to \psi, \varepsilon_\phi \to \frac{1}{\psi}, \varepsilon_z \to \frac{1}{\psi}. \tag{5-8}$$

Therefore, ε_r at the outer boundary increases with the increase of ψ. This suggests that ε_r at the outer boundary increases in the order from $Y= d^{-5}$ to $Y=d^5$. On the other hand, ε_ϕ and ε_z at the outer boundary decrease with the decrease of ψ. This suggests that ε_z at the outer boundary increases in the order from $Y=d^5$ to $Y=d^{-5}$.

Subsequently, the slopes of ε_r and ε_z, at the inner boundary are investigated. The slopes of them can be written as

$$r' \to a, r \to 0 \Rightarrow \frac{d\varepsilon_r}{dr} \to \frac{\psi}{a}, \frac{d\varepsilon_z}{dr} \to \frac{1}{a \cdot \psi}. \tag{5-9}$$

Equation (5-9) suggests that the slope of ε_r at the inner boundary increase with increasing ψ, whereas that of ε_z at the inner boundary increases with decreasing ψ. Therefore, the slope of ε_r at the inner boundary increases in the order from $Y=d^{-5}$ to $Y=d^5$, while that of ε_z at the inner boundary increases in the order from $Y=d^5$ to $Y=d^{-5}$.

Finally, the value of ε_ϕ near the inner boundary, that is, at $r=\delta$, is considered. Here, δ is a very small value. The value of ε_ϕ at $r=\delta$ can be calculated as follows:

$$\varepsilon_\phi = \frac{a}{\delta \cdot \psi} \tag{5-10}$$

This suggests that the value of ε_ϕ near the inner boundary increases with the decrease of ψ. That is, the value of ε_ϕ increases in the order from $Y=d^5$ to $Y= d^{-5}$.

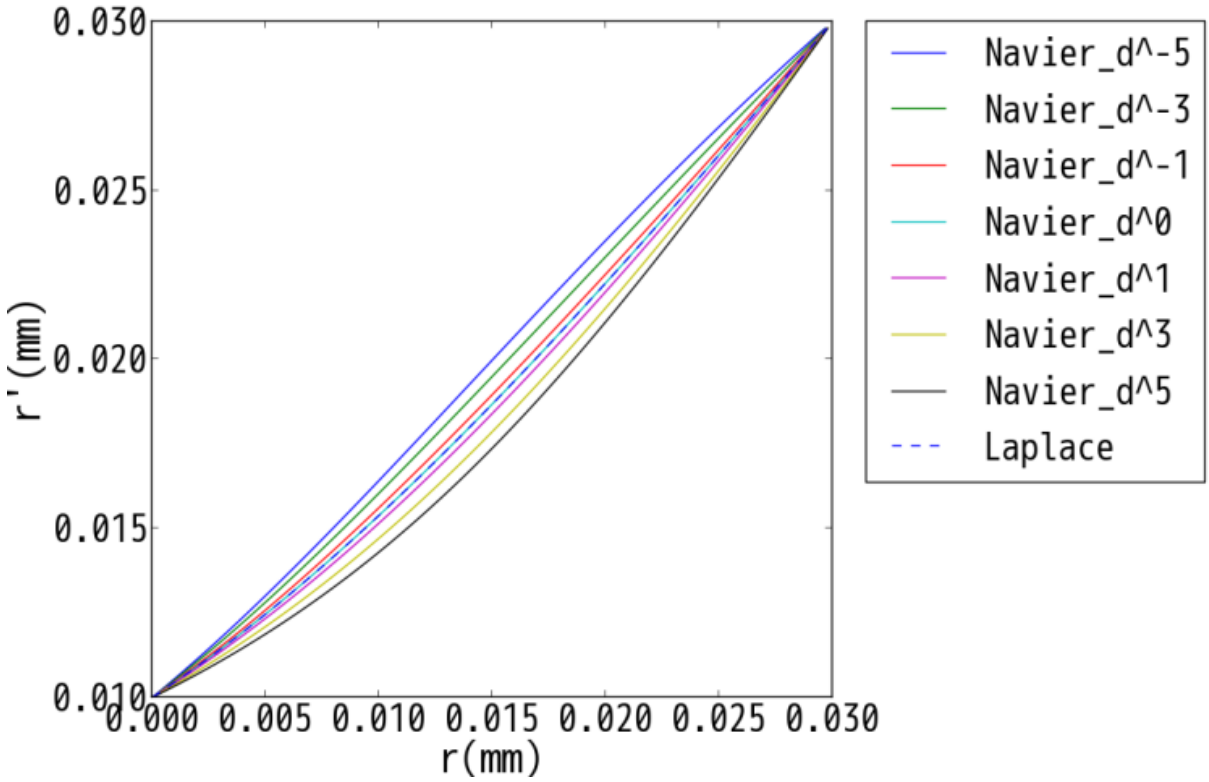

Fig. 5-17. The relationship between r and r' for various distributions of Young's modulus.

5.4.2. Effects of Young's modulus on cloaking performance

The cloaking performance calculated for the five relative full-mesh resolutions and the seven distributions of ε and μ is shown in Fig. 5-18. Figure 5-18 shows that distributions of Y decreasing from the inner boundary to the outer boundary, such as $Y=d^{-5}$ and $Y=d^{-3}$ tend to give high performance. From Figs. 5-7, 5-9, 5-11, 5-13, and 5-15, the most

dominant error contributing to the cloaking performance is found to be the deviation of ray trajectories passing near the inner boundary. This deviation is caused by the low accuracy of the interpolation of distributions of **ε** and **μ** inside the elements neighboring the inner boundary as described in 4.3.3. From Figs. 5-6~15, the deviation of the ray trajectories can be reduced by changing from $Y=d^5$ *to* $Y=d^{-5}$.

This tendency can be explained by the characteristics of the distributions of **ε** and **μ** described in 5.4.1. Figures 5-4 and 5-5 show that with changing from $Y=d^5$ to $Y=d^{-5}$, ε_r and ε_z can approach zero at larger d, and ε_ϕ can approach the unlimited value at larger d. By these characteristics, the ray passing near the inner boundary can be guided around the inner boundary at the larger d as shown in Fig. 5-19. Hence, these characteristics can prevent the ray from entering the region with the low accuracy, resulting in the successful cloaking.

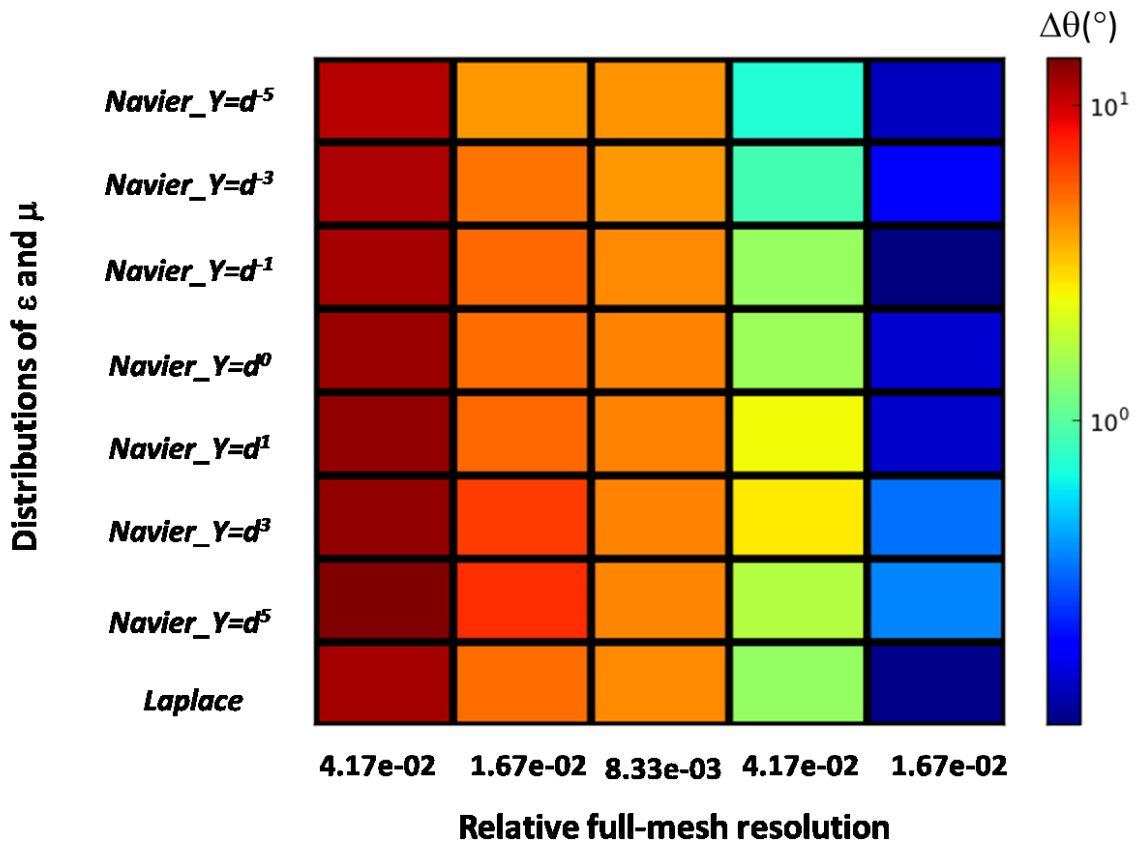

Fig. 5-18. The cloaking performance for the five relative full-mesh resolutions and the seven distributions of ε and μ.

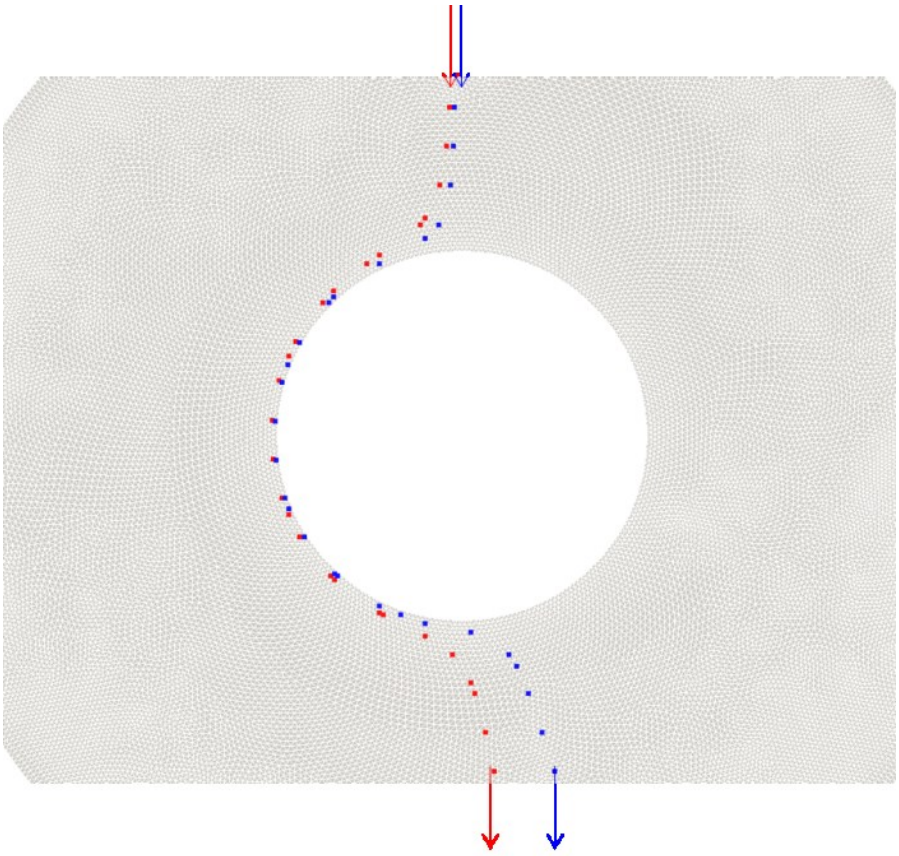

Fig. 5-19. The ray trajectories passing near the inner boundary for $Y=d^{-5}$ (the red points) and $Y=d^{5}$ (the blue points).

5.4.3. Validation of the improvement of cloaking performance for huge arbitrary cloaking

In order to confirm that the performance of cloaking devices with other shapes can be improved by modifying of the distribution of Y, the cloaking performance of a cloaking device with a more complicated shape, which has been investigated in 4.3.5, is calculated. The distributions of $\boldsymbol{\varepsilon}$ and $\boldsymbol{\mu}$ is obtained by the FEM-based numerical technique using the Laplace's equation and the Navier's equation with the following three distributions of Young's modulus: (i) $Y = d^{-5}$, (ii) $Y = d^{-3}$, and (iii) $Y = d^{-1}$. The cloaking device is modelled by the full-mesh representation with the relative full-mesh resolution of

1.67e–03.

The calculated ray trajectories are illustrated in Fig. 5-20. The numerical results of the cloaking performance are shown in Table 5-2. Table 5-2 indicates that the performance can be improved by employing the distributions of Y decreasing from the inner boundary to the outer boundary in comparison with the Laplace's equation in the same way as the cylindrical cloaking device.

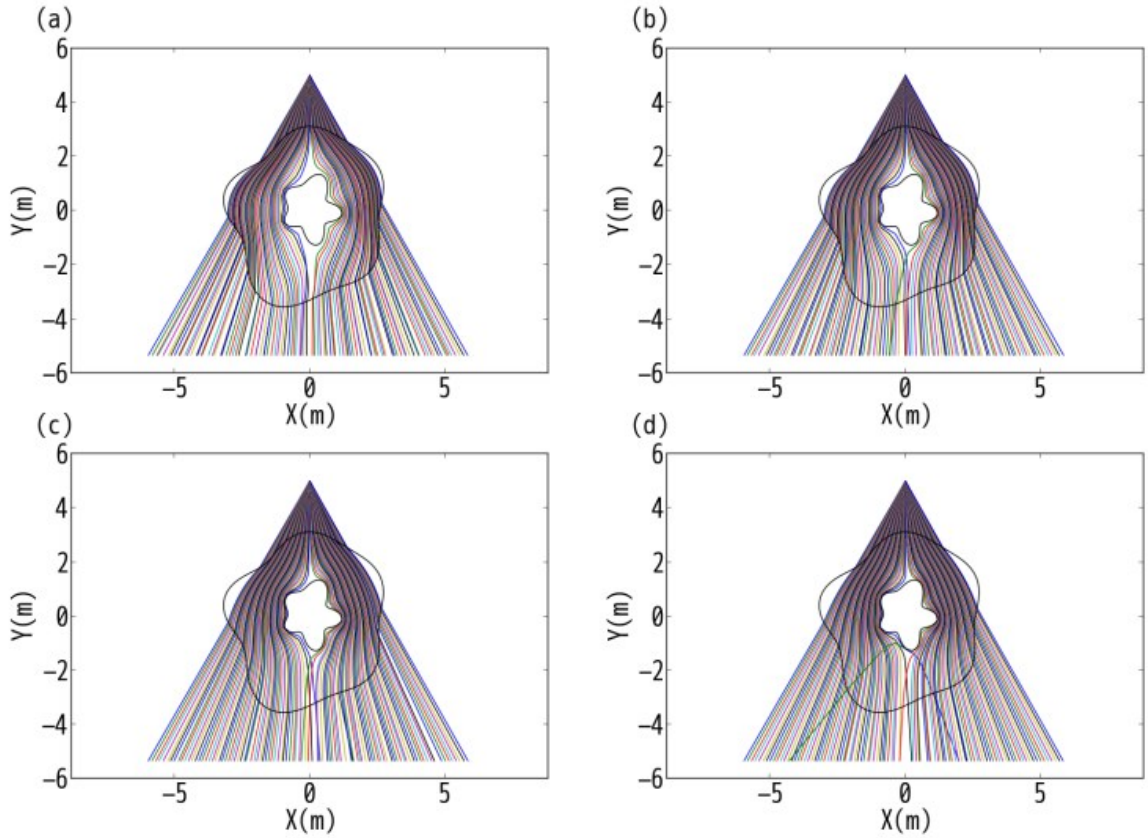

Fig. 5-20. The ray trajectories with the huge arbitrary cloaking device for the distributions of ε and μ obtained by the FEM-based solution of the Navier's equation with various distribution of Young's modulus (Y); (a) $Y = d^{-5}$, (b) $Y = d^{-3}$, and (c) $Y = d^{-1}$. As a reference, the ray paths for the Laplace's equation is shown in (d). The relative full-mesh resolution is 1.67e–03.

Table 5-2: Performances of the huge arbitrary cloaking device calculated for the distributions of ε and μ obtained by the FEM-based solution of the Navier's equation with various distribution of Young's modulus (*Y*) and the Laplace's equation.

Number	Relative full-mesh resolution	Equations		Δθ(°)
1	1.67e–03	Navier's Eq.	$Y=d^{-5}$	0.259
2			$Y=d^{-3}$	0.458
3			$Y=d^{-1}$	0.447
4		Laplace's Eq.		2.54

5.5. Conclusion

The improvement of the cloaking performance of the cylindrical cloaking device by the design of the distributions of ε and μ has been investigated. The distributions of ε and μ are changed by employing the Navier's equation with various distributions of Young's modulus as a partial differential equation for the numerical technique for the calculation of ε and μ based on the FEM. The cloaking performance has been evaluated by the Hamiltonian ray tracing with the full-mesh representation.

The numerical results have shown that the cloaking performance can be improved by employing distributions of Young's modulus where the value of Young's modulus decreases from the inner boundary to the outer boundary. These distributions of Young's modulus can generate the distributions of ε and μ which can guide the ray around the inner boundary at the larger distance from the inner boundary. Therefore, these distributions of Young's modulus can prevent the ray from entering the region with the low accuracy, resulting in the successful cloaking. From the obtained results, the

following guideline for the design of the distributions of ε and μ can be proposed: Higher values of Young's modulus near the inner boundary compared with other regions can lead to the improvement of the cloaking performance. Furthermore, it has been confirmed that the guideline can be applied to the example of huge cloaking devices with completely arbitrary shapes.

From the viewpoint of the manufacture, this design method of distributions of ε and μ can reduce the resolution required for successful cloaking since the method can improve the cloaking performance at a coarse full-mesh resolution. Therefore, the design of distributions of ε and μ will contribute to the realization of cloaking devices with large scale, taking the finite resolution of the manufacture into account.

References

1. J. Hu, X. Zhou and G. Hu, "Design method for electromagnetic cloak with arbitrary shapes based on Laplace's equation," Opt. Express **17**, 1308-1320 (2009).
2. X. Wang, S. Qu, Z. Xu, H. Ma, J. Wang, C. Gu, and X. Wu, "Three-dimensional invisible cloaks with arbitrary shapes based on partial differential equation," Appl. Math. Comput. **216**, 426–430 (2010).
3. https://www.csc.fi/web/elmer.
4. D. Schurig, J. B. Pendry, and D. R. Smith, "Calculation of material properties and ray tracing in transformation media," Opt. Express **14**, 9794–9804 (2006).
5. J.C. Halimeh, and M. Wegener, "Photorealistic rendering of unidirectional free-space invisibility cloaks," Opt. Express **21**, 9457–9472 (2013).
6. J. C. Halimeh and M. Wegener, "Time-of-flight imaging of invisibility cloaks," Opt. Express **20**, 63–74 (2012).
7. J. C. Halimeh, R. Schmied, and M. Wegener, "Newtonian photorealistic ray tracing of grating cloaks and correlation-function-based cloaking-quality assessment," Opt. Express **19**, 6078–6092 (2011).
8. J. C. Halimeh, and M. Wegener, "Photorealistic ray tracing of free-space invisibility cloaks made of uniaxial dielectrics," Opt. Express **20**, 28330–28340 (2012).
9. G. Dolling, M. Wegener, S. Linden, and C. Hormann, "Photorealistic images of objects in effective negative-index materials," Opt. Express **14**, 1842–1849 (2006).
10. J. C. Halimeh, R. T. Thompson, and M. Wegener, "Invisibility cloaks in relativistic motion," Phys. Rev. A 93, 013850 (2016).
11. J. C. Halimeh, and R. T. Thompson, "Fresnel-Fizeau drag: Invisibility conditions for all inertial observers," arXiv:1601.04218.
12. A. J. Danner, "Visualizing invisibility: Metamaterials-based optical devices in

natural environments," Opt. Express **18**, 3332–3337 (2010).

13. Y. Jiao, S. Fan, and D. A. B. Miller, "Designing for beam propagation in periodic and nonperiodic photonic nanostructures: Extended Hamiltonian method," Phys. Rev. E 70, 036612 (2004).
14. A. Alireza, and A. J. Danner, "Generalization of ray tracing in a linear inhomogeneous anisotropic medium: a coordinate-free approach," J. Opt. Soc. Am. A **27**, 2558–2562 (2010).

CHAPTER 6

Conclusions and Suggested Future Work

6.1. Summary

In this thesis, a novel Hamiltonian-based ray tracing has been proposed in order to evaluate the performance of macroscopic cloaking devices with arbitrary shapes, by solving the two technical issues for treatment of arbitrary shapes; (i) how to represent the surfaces of arbitrary shapes, (ii) how to represent the constitutive parameters inside of cloaking devices with arbitrary shapes. By using the Hamiltonian-based ray tracing, the analyses of examples of macroscopic cloaking devices with arbitrary shapes have been performed for the first time. In addition, the design of the distributions of the constitutive parameters has been proposed for improvement of cloaking performance.

In CHAPTER 3, in order to make a model of the cloaking device with the arbitrary shape, the surface of the cloaking device is represented by triangular meshes. In order to verify the proposed Hamiltonian ray tracing adapting the surface-mesh representation approach, the results of the spherical cloaking and the cylindrical cloaking from the surface-mesh representation approach have been compared with those from the approach where the surfaces of cloaking devices are represented by rigorous functions. From the comparison, the distortion due to the coarse mesh resolution has been found to occur with the surface-mesh representation approach, while by increasing the

surface-mesh resolution the distortion has been suppressed. Therefore, the cloaking performance of the surface-mesh representation with fine mesh resolution have been found to be in good agreement with that of the rigorous function representation, suggesting the verification of the surface-mesh representation.

In CHAPTER 4, a Hamiltonian ray tracing with the full-mesh representation, where the constitutive parameters of cloaking devices are calculated by the finite element method, has been proposed. The full-mesh representation was verified by comparison the result of cloaking simulations of the cylindrical cloaking device with the full-mesh representation and that with the rigorous function representation. The Hamiltonian-based ray tracing with the full-mesh representation have been applied to the double cylindrical cloaking device and the huge arbitrary cloaking device as examples of cloaking devices with arbitrary shapes. For the calculation of ε and μ of the cloaking device, the numerical method by using the solution of Laplace's equation based on the FEM was employed. This is the first time of analysis of macroscopic cloaking devices with arbitrary shapes. The numerical results of the double cylindrical cloaking device and the huge arbitrary cloaking device have shown high performance. This result suggests that the Hamiltonian ray tracing can be applied to evaluation of performance of cloaking devices with arbitrary shapes. The full-mesh representation is also found to be useful to fabricate the actual devices.

In CHAPTER 5, the improvement of performance of cylindrical cloaking by the design of distributions of constitutive parameters has been investigated. The distributions of the constituent parameters have been modified by employing the Navier's equation with various distributions of Young moduli as the partial differential equation for the numerical method calculation of the constitutive parameters based on FEM. The performances of cylindrical cloaking have been evaluated by the Hamiltonian

ray tracing with the full-mesh representation. The numerical results have revealed that cloaking performance can be improved by modifying the distributions of constitutive parameters.

The proposed novel Hamiltonian-based ray tracing can evaluate performance of macroscopic cloaking devices with arbitrary shapes. Therefore, the proposed method will significantly contribute to the realization of macroscopic cloaking devices. Especially, the full-mesh representation will be very useful since it can take account of resolution of fabrication. Moreover, the proposed design of distributions of constitutive parameters is expected to improve the cloaking performance for coarser resolution of fabrication technology.

6.2. Suggested Future Work

In order to realize cloaking devices in the future, the following two technical issues are addressed; (i) design of metamaterial which give ε and μ required, (ii) fabrication technology for layout of metamaterials which show different values of ε and μ in cloaking devices.

In order to resolve the technical issue (i), many types of metamaterial have been designed by using full-wave simulations, e.g. split ring resonator (SRR), metallic cut-wire pairs, fishnet structure, etc. Actually cloaking devices for visible light have been designed. However, since most of the metamaterials involve metals, they show large inherent losses, especially at visible frequencies. In order to decrease the loss, all-dielectric metamaterial has been investigated by utilization of Mie resonances. Although material which has large refractive index is required to induce the Mie resonances, such a material is available at microwave, terahertz and infrared frequencies,

leading to all-dielectric metamaterial. Furthermore, all-dielectric cloaking devices have been proposed at these frequencies. However, at visible frequencies, no experiment has been published since it is difficult to find material which has large refractive index.

Another approach to alleviate the issue of the loss is to introduce gain materials into the metamaterial structure. However, gain coefficients for the compensation of the loss are hard to obtain in practice.

In order to overcome the technical issue (i) fundamentally, new man-made magnetic materials with reduced loss are required at visible frequencies.

In terms of the technical issue (ii), few researches have been performed in order to layout metamaterials which show different values of ε and μ whereas fabrications of metamaterials which uniformly show certain values of ε and μ have been investigated intensively. On the other hand, it is expected that alinement technology used in semiconductor processing can be applied to the layout of metamaterials because current steppers or scanners have an alinement accuracy of several of nanometers. This study has shown that a resolution of the order of micrometer is required for high cloaking performance. I consider that this resolution can be realized by the current alinement technology. However, most of the fabrication methods for metamaterials, such as electron beam lithography (EBL), nanoimprint lithography (NIL), and direct laser writing (DLW), are not compatible with the current semiconductor processing. Therefore, the integration of these fabrication methods into the current semiconductor processing is necessary to overcome the technical issues (ii).

Acknowledgements

Firstly, I would like to express my deepest gratitude to my advisor Professor Osamu Matoba of Kobe University for his continuous support of my Ph.D study and his invaluable discussions and suggestions.

I am greatly grateful to Professor Nobuyuki Kaya of Kobe University for his kind guidance and his introduction of Professor Osamu Matoba.

I would like to thank to Prof. Hideki Sano, Prof. Chikara Ohta, and Associate Prof. Kouichi Nitta for fruitful comments for my Ph. D thesis.

I would like to thank to Mr. Hisanori Okada, Mr. Shinzi Goto, Mr. Toshiharu Yamamoto, and Mr. Masahiro Tsukamoto with AsahiKasei Corporation for providing me an opportunity of my Ph.D study,

Finally, I would like to thank my family for their financial support and continuous encouragement.

List of Publications

CHAPTER 3

1. T. Tanaka and O. Matoba, "Hamiltonian-based ray-tracing method with triangular-mesh representation for a large-scale cloaking device with an arbitrary shape," Appl. Opt. **55**, 3456-3461 (2016).

CHAPTER 4

1. T. Tanaka and O. Matoba, "Evaluation and design of a large-scale cloaking device by Hamiltonian-based ray-tracing method. Part I: full-mesh representation," J. Opt. Soc. Am. B, **34**, 1041-1051 (2017).

CHAPTER 5

1. T. Tanaka and O. Matoba, "Evaluation and design of a large-scale cloaking device by the Hamiltonian-based ray-tracing method. Part II: design of the distribution of constitutive parameters," J. Opt. Soc. Am. B, **34**, 1052-1059 (2017).

List of Presentations

[International Conference]

1. T. Tanaka and O. Matoba, “Analysis of double-cylindrical cloaking device by Hamiltonian-based ray-tracing method,” International Symposium on Optical Memory 2016 (ISOM'16), Mo-F-01, Oct. 17, 2016, Kyoto Research Park, Kyoto, Japan, Technical digest of ISOM'16, pp. 40-41 (2016). (Oral)

2. T. Tanaka and O. Matoba, “Improvement of Cloaking Performance by Designing the Constitutive Parameter,” Information Photonics 2017 (IP’17), IP-21PM-1-9, Apr. 21, 2017, PACIFICO Yokohama, Yokohama, Japan, Proceedings of IP'17, pp. 100-101 (2017). (Poster)

[Domestic Conference]

1. 田中健夫、的場修、”ハミルトニアン形式光線追跡法を用いた大規模クローキング素子の解析、” 第 41 回光学シンポジウム、講演番号 11、6/23, 東京大学生産技術研究所、講演予稿集、pp.29-30, 2016. (口頭)

Doctor Thesis, Kobe University

“Analysis of Macroscopic Cloaking Devices,” 147 pages

Submitted on June, 30th, 2017

The date of publication is printed in cover of repository version published in Kobe University Repository Kernel.